



DE GRUYTER  
OPEN

# Open Engineering

---

## Topical Issue on **Engineering Flow and Design**

### COORDINATING EDITORS

Antonio F. Miguel  
University of Évora  
Portugal

Luiz A. O. Rocha  
Federal University of Rio  
Grande do Sul, Brazil

Andreas Öchsner  
Griffith University  
Australia

**Abstracting and indexing:** Astrophysics Data System (ADS); Celdes; Chemical Abstracts Service (CAS); Chemical Abstracts Service (CAS) - SciFinder; CNKI Scholar (China National Knowledge Infrastructure); CNPIEC; EBSCO Discovery Service; SCOPUS; Google Scholar; J-Gate; JournalTOCs; Naviga (Softweco); Primo Central (ExLibris); ReadCube; ResearchGate; Summon (Serials Solutions/ProQuest); TDOne (TDNet); Ulrich's Periodicals Directory/ulrichsweb; WorldCat (OCLC)

Antonio F. Miguel, Luiz A. O. Rocha, and Andreas Öchsner

DOI 10.1515/eng-2015-0029

The importance of design in natural and engineered flow systems is undisputed. It is not only essential to life, but also plays a crucial role in our technological world. In Nature, it arises organically, spontaneously, and is the constructal path for systems to persist in time. The generation of the best design is the target of engineered flow systems. Fluid dynamics and thermodynamics have played a crucial role in the search for these flow designs. Analytical, numerical (CFD) and experimental studies played crucial roles in many technological breakthroughs. They provide the frameworks for understanding, simulating and interpreting flow phenomena.

This issue contains a selection of papers presented at the special session “Fluid Flow, Energy Transfer and Design” held at the 10th International Conference on Diffusion in Solids and Liquids in Paris, June 2014.

The first paper of this issue is focused on vascularization. In vascular design, flow bathes the containing volume almost uniformly, and is widely encountered in natural systems (river basins, lungs, etc.). Smart materials with advanced capabilities such as self-healing and self-cooling require bathing the entire volume with a healing agent or coolant fluid. Constructal theory focuses its attention on the relationship between the architecture of the flow system and its global performance, and Erdal Cetkin explores new constructal vascular designs for self-healing and self-cooling while decreasing the resistances to flow.

Over the years, many devices are developed for thermal management of systems such as heat sinks. Heat sinks are extensively used because are ease of use and provide a high heat transfer capability. Tunde Bello-Ochende study the performance of a cylindrical micro-pin fins with multiples arrays structures for maximum heat transfer. The results are obtained by combining the constructal design methodology with a numerical optimization technique.

Cement-based materials are envisaged in both surface and deep geological nuclear waste repositories. The success

of this confinement and storage lays on precise estimations of physical and chemical properties, such as the diffusivity. Hugo Mercado-Mendoza and Sylvie Lorente review the progress made by INSA in developing a technique based on “Electrochemical Impedance Spectroscopy” to determine the diffusion coefficient through non saturated porous materials.

The ocean is an inexhaustible source of energy. Wave energy is a promising but also a challenging form of renewable energy to harvest. Mateus Gomes and co-authors compare two types of physical constraints in the chimney of an oscillating water column device.

Nanofluids are solid suspensions of nanometer-size particles in a base liquid and find important applications in several areas including biomedicine, automobile, microelectronics, nuclear systems and power generation. These fluids are characterized by higher thermal conductivity and single-phase heat transfer coefficients than their base fluids. Mixed convection of Cu-water and Ag-water nanofluids in a square cavity is studied by Abdelkader Boutra and co-authors. The interest on soot formation stems mostly from environmental concerns on pollutant emission from combustion devices. Soot also contributes to thermal radiation loads on combustor liners and turbine blades. In the final paper of this issue, Nattan Caetano and co-authors investigate the soot formation in a flat flame burner using pre-mixed compressed natural gas and air.

The collection of the articles in this issue, along with a complementary and expansive volume devoted to the same subject<sup>1</sup>, reflect and reaffirm the importance and relevance of the study of flow design in natural and man-made flow systems in the twenty-first century.

We would like to thank the authors for their efforts in preparing the special issue articles. We are indebted to the anonymous reviewers who participated in the editorial process. Thanks are also due to Dr. M. Domanski and Dr. I. Grzegorek, Managing Editors of Open Engineering for the invaluable help and guidance throughout.

**Antonio F. Miguel** : University of Évora, Portugal

**Luiz A. O. Rocha**: Federal University of Rio Grande do Sul, Brazil

**Andreas Öchsner**: Griffith University, Australia

<sup>1</sup>A. F. Miguel, L. A. O Rocha, A. Öchsner (editors) Fluid Flow, Energy Transfer and Design II, Defect and Diffusion Forum 362, Trans. Tech. Publications, Switzerland, 2015

## Research Article

## Open Access

Erdal Cetkin\*

# Constructal vascularized structures

DOI 10.1515/eng-2015-0017

Received September 02, 2014; accepted January 01, 2015

**Abstract:** Smart features such as self-healing and self-cooling require bathing the entire volume with a coolant or/and healing agent. Bathing the entire volume is an example of point to area (or volume) flows. Point to area flows cover all the distributing and collecting kinds of flows, i.e. inhaling and exhaling, mining, river deltas, energy distribution, distribution of products on the landscape and so on. The flow resistances of a point to area flow can be decreased by changing the design with the guidance of the constructal law, which is the law of the design evolution in time. In this paper, how the flow resistances (heat, fluid and stress) can be decreased by using the constructal law is shown with examples. First, the validity of two assumptions is surveyed: using temperature independent Hess-Murray rule and using constant diameter ducts where the duct discharges fluid along its edge. Then, point to area types of flows are explained by illustrating the results of two examples: fluid networks and heating an area. Last, how the structures should be vascularized for cooling and mechanical strength is documented. This paper shows that flow resistances can be decreased by morphing the shape freely without any restrictions or generic algorithms.

**Keywords:** constructal law; vascularization; point to area flows; distributing flows; smart materials

## 1 Emergence of vascularization

Advanced capabilities such as self-healing and self-cooling require bathing the entire volume with coolant fluid or healing agent [1–5], which can be achieved by vascularization. In addition of being necessary for the advanced capabilities, vascularization is also essential to decrease the resistances of the distribution of energy, goods and water [1, 6, 7]. In smart materials, the structure is bathed with coolant or healing agent which is supplied

from a reservoir to obtain the smart features. Similarly, a factory distributes all its products to the cities located around the world. All these flows are examples of flow from a point to an area (or volume).

In addition, the peak temperature and the maximum stress of a heated and mechanically loaded structure can be kept under an allowable limit as its weight decreases with vascularization [8, 9]. Therefore, the penalty of moving the structure decreases which is crucial for avionics. Decreasing this penalty decreases the fuel consumption which is also essential due to finite source of fuel supplies. Vascularization is a necessity for the advanced aircrafts and space shuttles because it promises to protect the vehicles under great heat fluxes and great mechanical loads with being capable of repairing itself and being light and robust at the same time.

There are two kinds of cooling requirements for a structure: deterministic and random. The deterministic are due to heat sources that are known which are steady. However, random cooling requirements are unsteady and diverse. Vascularization also protects the structure from random heat sources [10]. Because random cooling requirements are unpredictable, they are responsible of damaging the structure which is designed to work under an allowable temperature level.

Constructal law is the law of the design evolution in time, and it was stated in 1996 by Adrian Bejan as “For a finite size system to persist in time (to live), it must evolve such a way that it provides easier access to the imposed currents that flow through it” [11]. Constructal law is a law because it is applicable for both animate and inanimate, i.e. it is valid for everything. Because it is a law, constructal law can be found in diverse fields such as biology, geophysics, engineering, social dynamics and evolution of sports [1, 12–43]. Constructal law is also significant because it fills the gap of design parameter in thermal sciences which is overlooked in the field.

In this paper constructal vascularized structures are used to enable advanced capabilities such as self-healing and self-cooling while decreasing the resistances of flow (heat, fluid and stresses). Constructal designs can be defined as the designs that perform the best in their environment (boundary conditions, initial conditions) with the existence of constraints (size, shape, volume of material). The power of constructal designs comes from pursu-

\*Corresponding Author: Erdal Cetkin: Izmir Institute of Technology, Department of Mechanical Engineering, Urla, Izmir 35430, Turkey, E-mail: erdalcetkin@iyte.edu.tr

ing the designs best fits to their environment without any assumptions, design constraints and generic algorithms. Constructal designs are free to vary and there is no optimal design.

## 2 Validity of flow assumptions

The accuracy of the assumptions is crucial for the validity of the results. Therefore, this section discusses the validity of two assumptions in fluid flow problems. First, it is questioned how a duct should be shaped to discharge fluid along its length while the flow resistance is the smallest, Figure 1. Second, the effect of temperature on Hess-Murray rule is uncovered by assuming the properties of the fluid is temperature dependent.

### 2.1 Tapered ducts

Imagine a duct which discharge fluid along its length which can be a model of a duct connected to a number of users receiving the fluid along its length, Figure 1 [44]. The flow rate in the duct varies linearly  $\dot{m}(x) = \dot{m}x/L$ . The pressure drops for laminar and turbulent flows are

$$\Delta P_1 = C_1 \frac{\dot{m}}{L} \int_0^L \frac{x}{D^4} dx \quad (1)$$

$$\Delta P_t = C_t \frac{\dot{m}^2}{L^2} \int_0^L \frac{x^2}{D^5} dx,$$

where  $C_1 = 128/\nu\pi$  and  $C_t = 32f/\pi^2\rho$ , and  $\nu$ ,  $\rho$  and  $f$  are the kinematic viscosity, the density and the constant fric-

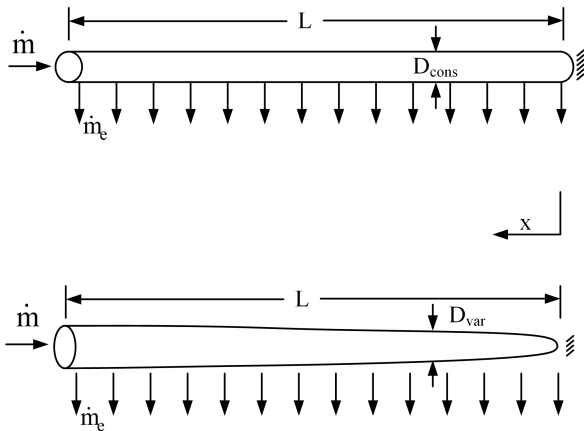


**Figure 1:** Supply duct with longitudinally distributed discharge: duct with constant diameter (top) and tapered duct (bottom).

tion factor for turbulent flow in the fully developed and fully rough regime, respectively [1].  $m$ ,  $L$ ,  $x$  and  $D$  are the mass flow rate that enters the duct, the length, the distance from the closed end of the duct, and the diameter, respectively. The volume constraint is

$$Vol = \int_0^L \frac{\pi}{4} D^2 dx. \quad (2)$$

The pressure drops for laminar and turbulent flow regimes along the duct with constant diameter are

$$\Delta P_{0,1} = C_1 \frac{\dot{m}L}{2D_0^4} \quad (3)$$

$$\Delta P_{0,t} = C_t \frac{\dot{m}^2 L}{3D_0^5}.$$

Now consider the duct shape is free to vary. By using variational calculus, pressure drops of Equation (1) can be minimized subject to the volume constraint of Equation (2). The tapered channel diameters and their pressure drops for laminar and turbulent regimes are

$$\Delta P_{min,1} = \frac{3^3 \pi^2 C_1 \dot{m} L^3}{4^5 Vol^2} \quad (4)$$

$$D_{min,1} = \left( \frac{16 Vol}{3\pi L} \right)^{1/2} \left( \frac{x}{L} \right)^{1/6}$$

$$\Delta P_{min,t} = C_t \dot{m}^2 \pi^{5/2} \left( \frac{7L}{44Vol} \right)^{7/2} \quad (5)$$

$$D_{min,t} = \left( \frac{44 Vol}{7\pi L} \right)^{1/2} \left( \frac{x}{L} \right)^{2/7}.$$

Dividing the minimized pressure drops of Equations (4) and (5) by the pressure drops of Equation (1), for turbulent and laminar flows respectively, shows the reduction in the flow resistance by tapering the ducts in laminar and turbulent flow regimes

$$\frac{\Delta P_{min,1}}{\Delta P_{0,1}} = \frac{3^3 2}{4^3} = 0.84$$

$$\frac{\Delta P_{min,t}}{\Delta P_{0,t}} = 3 \left( \frac{7}{11} \right)^{7/2} = 0.62. \quad (6)$$

The results of Equation (6) show that the flow resistance of the tapered ducts is smaller when the duct discharges fluid along its length. In laminar flow regime, modeling the channel as a constant diameter duct would not affect the results as much as in turbulent flow regime.

## 2.2 Temperature dependence

Dendritic flow structures offer less resistance when bifurcations are accompanied with the Hess-Murray rule for the diameter ratio of the mother and daughter channels. The concept is reviewed by assuming the general case of temperature dependent properties [8]. In addition, the mother tube is connected to  $n$  identical daughter tubes, and the flow regime can be laminar or turbulent. The fluid volume is fixed. The pressure drop formula for laminar flow is

$$\Delta P = C_1 v_i \dot{m}_i \frac{L_i}{D_i^4}, \quad (7)$$

where  $v_i$  is the kinematic viscosity corresponding to the mean temperature  $T_{me} = \int T dVol / \int dVol$ .

The total flow volume and pressure drop area

$$\begin{aligned} Vol &= \pi \frac{D_1^2}{4} L_1 + n \pi \frac{D_2^2}{4} L_2 \\ \Delta P &= C v_1 \dot{m}_1 \frac{L_1}{D_1^4} + C v_2 \dot{m}_2 \frac{L_2}{D_2^4}, \end{aligned} \quad (8)$$

where  $\dot{m}_2 = \dot{m}_1/n$ . The diameter ratio for minimum  $\Delta P$  in laminar flow regime is

$$\frac{D_1}{D_2} = n^{1/3} \left( \frac{v_1}{v_2} \right)^{1/6}. \quad (9)$$

The pressure drop formula for fully developed and fully rough turbulent flow is

$$\Delta P = \frac{C_i \dot{m}_i^2 L_i}{\rho_i D_i^5}, \quad (10)$$

where  $\rho_i$  is the density of the fluid corresponding to  $T_{me}$ . The diameter ratio corresponding to the smallest flow resistance in turbulent flow is

$$\frac{D_1}{D_2} = n^{3/7} \left( \frac{\rho_2}{\rho_1} \right)^{1/7}. \quad (11)$$

The effect of variable properties is felt through the ratios  $(v_1/v_2)^{1/6}$  and  $(\rho_2/\rho_1)^{1/7}$  for laminar flow and turbulent flow, respectively. Assumption of the fluid with temperature independent properties is valid when the temperature variations are small enough.

## 3 Point to area flows: distribution on the landscape

The distribution of fluids, energy and products from a source to the individuals is essential for life. Its importance has increased with globalization because the production

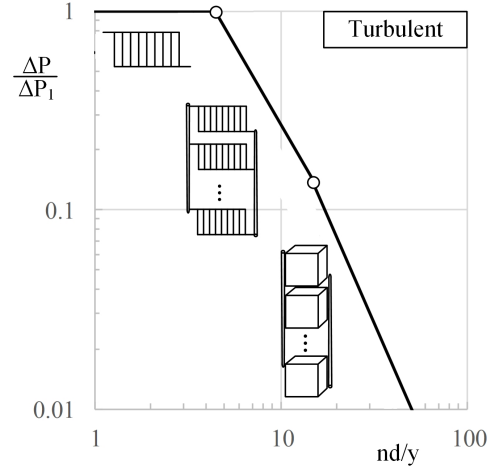


**Figure 2:** The pressure drop of three competing designs divided by the pressure drop of the design of stack of  $n$  elemental flow volumes for turbulent flow regime.

efficiency has increased with the mass production. Similarly, the efficiency of heaters increases as their size increases [7, 45, 46]. Therefore, the distribution of hot water to a number of users from a central heater, i.e. urban heating, became more efficient than individual heating. The materials gathered around the world (area to point flow) become end products in a factory, and these products are distributed to millions of people every day (point to area flow). These distributing and collecting types of flows can perform with greater efficiency if their flow resistances are reduced [1]. The flow resistances cannot be eliminated but they can be reduced to a limit. In heat engines this limit is known as Carnot limit (Carnot efficiency).

### 3.1 Fluid networks

In the case of distributing fluid to a number of elemental volumes or users there are infinite design possibilities. However, the objective is to find the design that corresponds to the smallest resistance for a known size (number of elemental volumes or users) [44, 47]. Depending on the flow regime and other conditions there is a design which achieves the smallest flow resistance, Figure 2 [44]. Figure 2 shows that as the number of elemental volumes increase the flow resistance can be decreased by changing the design. If the size of the elemental volume is fixed, this result means that as the size of the structure increases, the design should be changed, i.e. the design of the miniature structure should be different than the normal scale structure to achieve the smallest flow resistance possible.

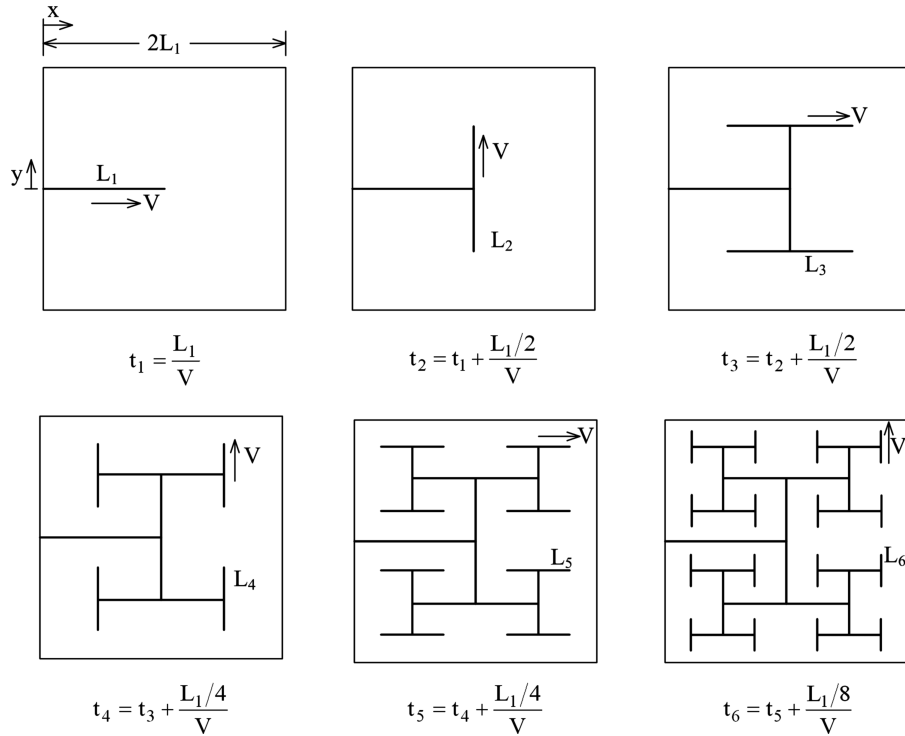


Figure 3: Tree-shaped line invasion of a conducting domain with assumed T-shaped bifurcations.

### 3.2 Heating of an area

Similar to distributing fluid to an area and bathing the area with fluid, imagine that a conducting area is invaded by heating, for instance, is bathed with a hot stream. The conducting domain is two dimensional with the uniform initial temperature ( $T_0$ ), conductivity ( $k$ ) and thermal diffusivity ( $\alpha$ ). The boundaries of the square are insulated. Beginning with the time  $t = 0$ , lines of uniform temperature ( $T_1$ ) invade the conducting domain with the constant speed  $V$ , Figure 3 [48]. Heat is transferred by thermal diffusion from the invading lines to the conducting material. The details of the solution method can be seen in Ref. [48]. The temperature averaged over the square area is

$$T_{avg} = \frac{1}{A} \iint_A T dx dy \tag{12}$$

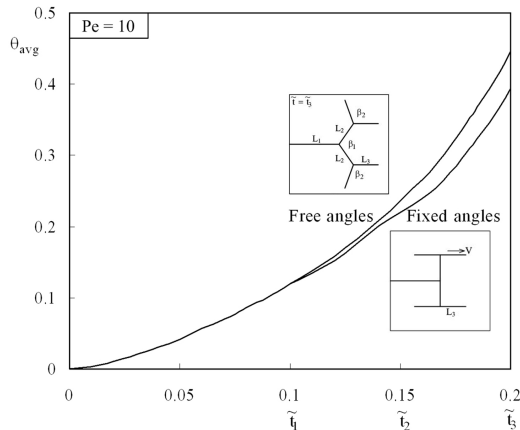
and it rises from  $T_0$  to  $T_1$ .

Figure 4 shows that S curve of the history of invading becomes steeper as the invading tree morphed freely. The overall resistance to the heat flow is decreased just by changing the shape of the invading tree as all the other parameters (total length of the tree, invading speed, boundary conditions and initial conditions) are the same. Fig-

ure 4 emphasizes the importance of design parameter in thermal sciences.

## 4 Vascularization for cooling and mechanical strength

Vascularization increases the cooling performance of a structure, and it decreases the mechanical strength of the structure if the material is removed for the cooling channels. However, vascularization increases the mechanical strength of the structure if the material of the structure is fixed, i.e. the material removed for the channels are placed around the cooling channels. Constructal law states that the material should be placed where it is needed the most to decrease the resistance to its flow. This flow can be flow of stresses [1, 49–51] as well as the flow of fluid and heat. Greater mechanical strength is promised by placing the material away from the center where the material is stressed the least in the case of a plate loaded with a uniform force from its below and the edge of this plate is a no displacement boundary condition. A beam is an example to how mechanical strength can be increased by vary-



**Figure 4:** The S curve of tree invasion with free angles is steeper (faster) than the S curve of tree invasion with fixed branching angles.

ing the shape of the beam when the amount of material is fixed.

#### 4.1 Radial and tree-shaped channel configurations

Here the thermal and mechanical performances of a heated and mechanically loaded circular plate have increased by embedding vascular structures in it. The diameter and thickness of the plate are  $D$  and  $H$ , and their ratio is fixed  $D/H = 10$ , Figure 5a [8]. The total volume and the volume of the channels are fixed. The plate with radial cooling channels is subjected to uniformly distributed force and uniform heat flux, both acting from below, Figure 5a. The dimensionless governing equations (the mass conservation, the conservation of the momentum for the fluid domain, the energy equation, the generalized Hooke's law and the conservation of momentum equations for solid domain) were solved in a finite element software<sup>1</sup>. Mesh test was also performed to confirm mesh independency of the results [8].

The heat flux and mechanical load which are subjected from the bottom of the plate as shown in Figure 5a, are fixed. The pressure difference between inlet and outlet is nondimensionalized as [52, 53].

$$\tilde{P}_{max} = \frac{(P_{in} - P_{ref}) D^2}{\mu \alpha}, \quad (13)$$

where  $\mu$  and  $\alpha$  are dynamic viscosity and thermal diffusivity. The value of  $\tilde{P}_{max}$  represents their dimensionless over-

all pressure difference. The flow is laminar in all the channels.

The purpose of morphing the shape is to decrease the peak temperature and stress. Figure 5b shows the relation between the temperature, stress and number of ducts when  $\tilde{P}_{max}$  is  $10^7$  and  $10^8$ . The maximum stress decreases when the number of the cooling channels increases from 6 to 8 and then increases when the number of the cooling ducts increases. The reason of this behavior is that the maximum stress increases in the vicinity of the junctions of the cooling ducts. Even though  $\sigma_{max}$  is the minimum when the number of the channels is 8, neighboring designs (design of 6 cooling channels when  $\tilde{P}_{max} = 10^7$  and design of 12 cooling channels when  $\tilde{P}_{max} = 10^8$ ) offer minimum peak temperatures. In summary, when  $\tilde{P}_{max}$  is specified, it is possible to identify one design (or a group of similar designs) that provides low peak stress and peak temperature. However, there is no optimal design for all the conditions.

#### 4.2 Hybrid channel configurations

Consider a square plate with length  $L$ , thickness  $H = 0.1L$ , and embedded cooling channels, Figure 6a [9]. The plate is subjected to a uniformly distributed force acting from below, and it is heated uniformly. The volume of the structure and the flow volume are fixed.  $L_g$  is the side of the square area in which the grid cooling channels are embedded. The grid channels are connected to the periphery with radial channels. Coolant enters or exits from the center of the grid, and it is driven by the pressure difference maintained between the inlet and outlet. The results were obtained by solving the governing equations numerically as discussed in the previous subsection.

Figure 6b shows the minimum peak temperatures plotted against the peak stresses as  $L_g/L$  varies. The effect of the flow direction is weak. The smaller  $T_{peak}$  and  $\sigma_{peak}$  values occur when  $L_g/L < 0.25$ . Peak stress is the minimum when the design is a hybrid of grid and trees. However, the peak temperature is the minimum when the channels are configured as radial channels.

#### 4.3 Concentrated heating

An important aspect to consider is the concentrated heating in the vascularized solid. Until now the heat generation effect was uniform. Here the effect of concentrating the heat generation in a small area is documented. The area of the heated spot is 1/16 of the square area of length

<sup>1</sup> See [www.comsol.com](http://www.comsol.com) for information about comsol multiphysics.

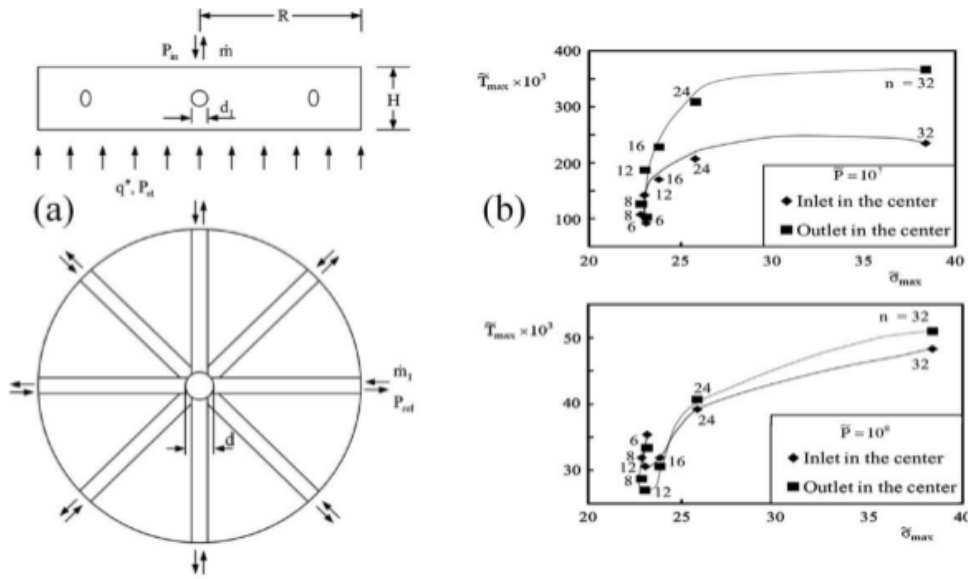


Figure 5: (a) Radial cooling channel configuration embedded in the circular plate. (b) The effect of the number of cooling ducts on the maximum temperature and stress.

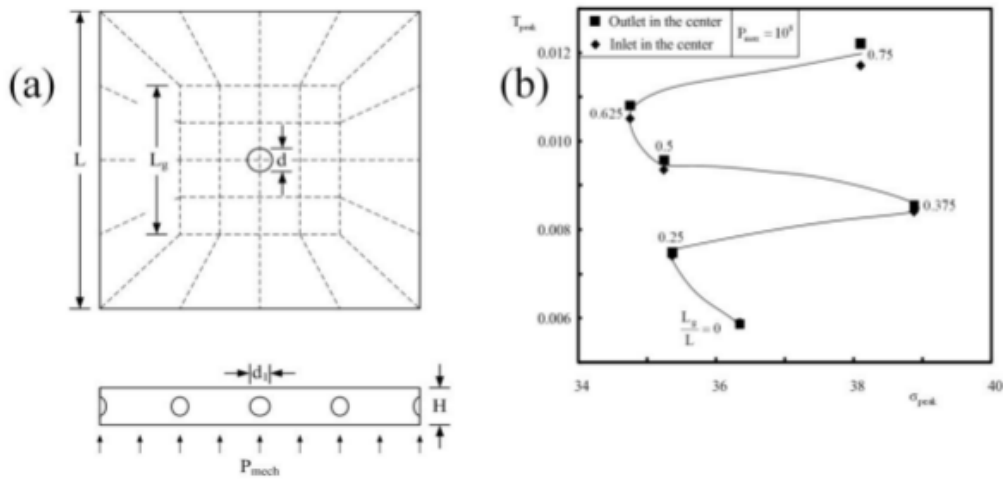


Figure 6: (a) Grid structure connected to the perimeter with radial channels, hybrid structure of a square slab. (b) Minimum peak temperatures relative to their peak stresses as  $L_g/L$  varies.

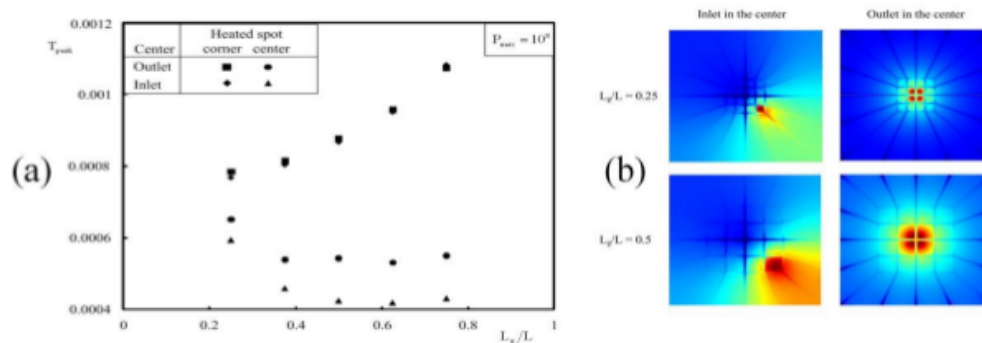
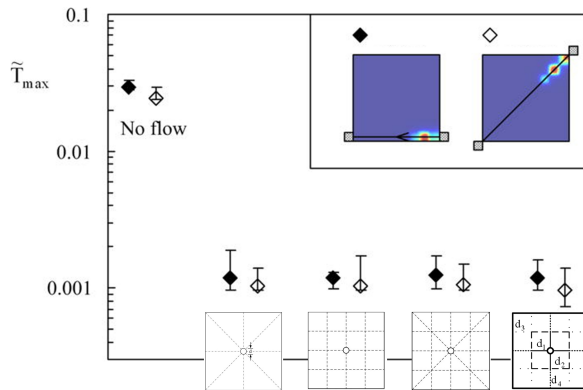


Figure 7: (a) Peak temperature relative to  $L_g/L$  when the flow direction and the concentrated heat generation location change. (b) The temperature distribution in the mid-plane of the slab.



**Figure 8:** The average peak temperature in four competing designs.

$L_g$ , Figure 7 [9]. The heating rate of the concentrated heat generation is fixed.

Figure 7 shows the temperature distribution when the heat generation is concentrated in the center of the slab and in the corner of the grid. Two designs are illustrated,  $L_g/L = 0.25$  and  $0.5$ . The flow direction changes from inlet in the center to outlet in the center. Figure 7 also shows the evolution of the peak temperature as  $L_g/L$  increases. When the concentrated heating is located in the center of the slab,  $T_{peak}$  decreases as  $L_g/L$ . When the concentrated heating is located in the corner of the grid,  $T_{peak}$  increases as  $L_g/L$  increases. The  $T_{peak}$  value is the lowest with  $L_g/L = 0.25$  when the concentrated heating is in the corner, and with  $L_g/L = 0.625$  when the concentrated heating is in the center. In addition, when  $L_g/L = 0.375$  the peak temperature becomes almost as low as the lowest peak temperature obtained when the concentrated heating is located in the center or in the corner.

#### 4.4 Moving hot spot

Consider a square plate of width and length  $L$ , and with thickness of  $H = 0.1L$ , Figure 8 [10]. A structure of cooling channels is embedded in this plate to keep it under its maximum allowable temperature while the plate is heated with a concentrated and moving heat flux spot. The length scale of the square footprint of the heating spot is  $0.1L$  and it moves with the constant speed of  $W$  from one edge of the plate to its other edge. Reference 8 documents the change in the temperature for four possible beam paths. The volume of the solid structure and the volume of the coolant fluid are fixed. Coolant enters or exits from the center of the slab while the pressure difference between the entrance

and exit is fixed. The flow is incompressible with constant properties and it is time dependent. The governing equations were solved as in the previous subsections.

Figure 8 shows the average peak temperature in four competing designs. The error bars indicate the maximum and minimum peak temperatures when the dimensionless time is greater than  $0.1$ , i.e. after the entire beam enters the plate surface. The peak temperatures for four different possible beam paths are documented. Figure 8 also shows that a plate heated by a moving beam with an unpredictable path can be cooled to under an allowable temperature level by embedding vascular cooling channels in the plate. The effect of changing from no cooling to vascular cooling is dramatic.

## 5 Conclusions

The main conclusion of this paper is that the flow resistances (heat, fluid and stress) can be decreased with vascularization by using the constructal law. However, there is no design that is optimal. The design should be changed to the new phase of the constructal design for the greatest performance as the conditions (i.e., boundary conditions, objectives and assumptions) change. This paper shows that the design is live and should vary freely for the greatest performance.

First, the assumptions of using temperature independent Hess-Murray rule and using constant diameter ducts where the duct discharges fluid along its edge are valid in which limits are documented. Then, point to area types of flows are explained by illustrating the results of two examples: fluid networks and heating of an area. These examples showed that the design should be varied freely for the smallest flow resistances as the conditions change.

This paper shows that the cooling performance and mechanical strength of a system which is heated and loaded with a distributed force can be increased by embedding vascular structures into it. The embedded vascular structure can be designed such that its cooling performance and mechanical strength is the greatest for the given conditions. The cooling of the system is also documented when the system is heated locally.

**Acknowledgement:** This work was supported by the Republic of Turkey. The author thanks to Prof. Adrian Bejan and Prof. Sylvie Lorente for their valuable comments and suggestions.

## References

- [1] Bejan A., Lorente S., *Design with constructal theory*, Wiley, 2008.
- [2] Aragon A.M., Wayer J.K., Geubelle P.H., Goldberg D.E., White S.R., *Design of microvascular flow networks using multi-objective genetic algorithms*, *Comput. Methods Appl. Mech. Eng.*, 2008, 197, 4399–4410.
- [3] Cho K.-H., Kim M.-H., *Fluid flow characteristics of vascularized channel networks*, *Chem. Eng. Sci.*, 2010, 65, 6270–6281.
- [4] Hamilton A.R., Sottos N.R., White S.R., *Mitigation of fatigue damage in self-healing vascular materials*, *Polymer*, 2012, 53, 5575–5581.
- [5] Williams H.R., Trask R.S., Waever P.M., Bond I.P., *Minimum mass vascular networks in multifunctional materials*, *J. R. Soc. Interface*, 2008, 5, 55–65.
- [6] Lee J., Lorente S., Bejan A., Kim M., *Vascular structures with flow uniformity and small resistance*, *Int. J. Heat Mass Transfer*, 2009, 52, 1761–1768.
- [7] Bejan A., Lorente S., *The constructal law and the evolution of the design in nature*, *Phys. Life Rev.*, 2011, 8, 209–240.
- [8] Cetkin E., Lorente S., Bejan A., *Vascularization for cooling and mechanical strength*, *Int. J. Heat Mass Transfer*, 2011, 54, 2774–2781.
- [9] Cetkin E., Lorente S., Bejan A., *Hybrid grid and tree structures for cooling and mechanical strength*, *J. Appl. Phys.*, 2011, 110, 064910.
- [10] Cetkin E., Lorente S., Bejan A., *Vascularization for cooling a plate heated by a randomly moving source*, *J. Appl. Phys.*, 2012, 112, 084906.
- [11] Bejan A., *Advanced engineering thermodynamics*, 2nd ed, Wiley, 1997.
- [12] Rocha L.A.O., Lorente S., Bejan A., *Constructal law and the unifying principle of design*, Springer, 2012.
- [13] Bejan A., Zane J.P., *Design in nature: How the constructal law governs evolution in biology, physics, technology and social organizations*, Doubleday, 2012.
- [14] Bejan A., Merx G.W., *Constructal theory of social dynamics*, Springer, 2007.
- [15] Bejan A., *Shape and structure from engineering to nature*, Cambridge University Press, 2000.
- [16] Reis A.H., *Constructal theory: from engineering to physics, and how flow systems develop shape and structure*, *Appl. Mec. Rev.*, 2006, 59, 269–282.
- [17] Raja A.H., Basak T., Das S.K., *Thermal performance of a multi-block heat exchanger designed on the basis of Bejan's constructal theory*, *Int. J. Heat Mass Transfer*, 2008, 51, 3582–3594.
- [18] Lorente S., *Constructal view of electrokinetic transfer through porous media*, *J. Phys. D Appl. Phys.*, 2007, 40, 2941–2947.
- [19] Chen Y., Cheng P., *An experimental investigation on the thermal efficiency of fractal tree-like microchannel nets*, *Int. Comm. Heat Mass Transfer*, 2005, 32, 931–938.
- [20] Reis A.H., *Constructal view of scaling laws of river basins*, *Geomorphology*, 2006, 78, 201–206.
- [21] Muzychka Y.S., *Constructal multi-scale design of compact micro-tube heat sinks and heat exchangers*, *Int. J. Thermal Sci.*, 2007, 46, 245–252.
- [22] Reis A.H., Miguel A.F., Aydin M., *Constructal theory of flow architecture of lungs*, *Med. Phys.*, 2004, 31, 1135–1140.
- [23] Azoumah Y., Mazet N., Neveu P., *Constructal network for heat and mass transfer in a solid-gas reactive porous medium*, *Int. J. Heat Mass Transfer*, 2004, 47, 2961–2970.
- [24] Tondeur D., Luo L., *Design and scaling laws of ramified fluid distributors by the constructal approach*, *Chem. Eng. Sci.*, 2004, 59, 1799–1813.
- [25] Miguel A.F., *Constructal pattern formation in stony corals, bacterial colonies and plant roots under different hydrodynamics conditions*, *J. Theoretical Biol.* 2006, 242, 954–961.
- [26] Zhou S., Chen L., Sun F., *Optimization of constructal volume-point conduction with variable cross section conducting path*, *Energy Convers. Manage.*, 2007, 48, 106–111.
- [27] Wechsato W., Ordóñez J.C., Kosaraju S., *Constructal dendritic geometry and the existence of asymmetric bifurcations*, *J. Appl. Phys.*, 2006, 100, 113514.
- [28] Wu W., Chen L., Sun F., *On the area to point flow problem based on constructal theory*, *Energy Convers. Manage.*, 2007, 48, 101–105.
- [29] Rocha L.A.O., Lorenzini E., Biserni C., *Geometric optimization of shapes on the basis of Bejan's Constructal theory*, *Int. Comm. Heat Mass Transfer*, 2005, 32, 1281–1288.
- [30] Wu W., Chen L., Sun F., *Heat-conduction optimization based on constructal theory*, *Appl. Energy*, 2007, 84, 39–47.
- [31] Beyene A., Peffley J., *Constructal theory, adaptive motion, and their theoretical application to low-speed turbine design*, *J. Energy Eng.*, 2009, 135, 112–118.
- [32] Lorenzini G., Rocha L.A.O., *Constructal design of T-Y assembly of fins for an optimized heat removal*, *Int. J. Heat Mass Transfer*, 2009, 52, 1458–1463.
- [33] Biserni C., Rocha L.A.O., Stanescu G., Lorenzini E., *Constructal H-shaped cavities according to Bejan's theory*, *Int. J. Heat Mass Transfer*, 2007, 50, 2132–2138.
- [34] Azoumah Y., Neveu P., Mazet N., *Optimal design of thermochemical reactors based on constructal approach*, *Aiche J.*, 2007, 53, 1257–1266.
- [35] Zhou S., Chen L., Sun F., *Constructal entropy generation minimization for heat and mass transfer in a solid-gas reactor based on triangular element*, *J. Phys. D Appl. Phys.*, 2007, 40, 3545–3550.
- [36] Reis A.H., Miguel A.F., *Constructal theory and flow architectures in living systems*, *Thermal Sci.*, 2006, 10, 57–64.
- [37] Carone M.J., Williams C.B., Allen J.K., Mistree F., *An application of constructal theory in the multi-objective design of product platforms*, *ASME 2003 Design Engineering Technical Conferences and Computer and Information in Engineering Conference Chicago, Illinois USA, September 2-6, 2003*.
- [38] Lorente S., Cetkin E., Bello-Ochende T., Meyer J.P., Bejan A., *The constructal-law physics of why swimmers must spread their fingers and toes*, *J. Theor. Biol.*, 2012, 308, 141–146.
- [39] Bejan A., Lorente S., *The physics of spreading ideas*, *Int. J. Heat Mass Transfer*, 2012, 55, 802–807.
- [40] Bejan A., Jones E.C., Charles J.D., *The evolution of speed in athletics: why the fastest runners are black and swimmers are white*, *Int. J. Design Nature*, 2010, 5, 1–13.
- [41] Bejan A., *Why so many shapes resemble the golden ratio: vision, cognition, and locomotion as a single design in nature*, *Int. J. Design Nature Ecodyn.*, 2009, 4, 97–104.
- [42] Rocha L.A.O., Isoldi L.A., Real M.V., dos Santos E.D., Correia A.L.G., Lorenzini G., Biserni C., *Constructal design applied to the elastic buckling of thin plates with holes*, *Centr. Eur. J. Eng.*,

- 2013, 3, 475–483.
- [43] Miguel A.F., An analytical approach for optimal design of heat sinks under forced convection, *Centr. Eur. J. Eng.*, 2013, 3, 276–284.
- [44] Cetkin E., Lorente S., Bejan A., Natural constructal emergence of vascular design with turbulent flow, *J. Appl. Phys.*, 2010, 107, 114901.
- [45] Bejan A., Lorente S., Yilbas B.S., Sahin A.Z., The effect of size on efficiency: power plants and vascular designs, *Int. J. Heat Mass Transfer*, 2011, 54, 1475–1481.
- [46] Lorente S., Bejan A., Few large and many small: hierarchy in movement on earth, *Int. J. Nature Ecodyn.*, 2010, 5, 254–267.
- [47] Kim S., Lorente S., Bejan A., Miller W., Morse J., The emergence of vascular design in three dimensions, *J. Appl. Phys.*, 2008, 103, 123511.
- [48] Cetkin E., Lorente S., Bejan A., The steepest S curve of spreading and collecting flows: Discovering the invading tree, not assuming it, *J. Appl. Phys.*, 2012, 111, 114903.
- [49] Bejan A., Lorente S., Lee J., Unifying constructal theory of roots, canopies and forests, *J. Theor. Biol.*, 2008, 254, 529–540.
- [50] Bejan A., The constructal-law origin of the wheel, size and skeleton in animal design, *Am. J. Phys.*, 2010, 78, 692–699.
- [51] Lorente S., Lee J., Bejan A., The flow of stresses concept: The analogy between mechanical strength and heat convection, *Int. J. Heat Mass Transfer*, 2010, 53, 2963–2968.
- [52] Bhattacharje S., Grosshandler W.L., The formation of a wall jet near a high temperature wall under microgravity environment, *ASME HTD*, 1988, 96, 711–716.
- [53] Petrescu S., Comments on the optimal spacing of parallel plates cooled by forced convection, *Int. J. Heat Mass Transfer*, 1994, 37, 1283.

## Research Article

## Open Access

Tunde Bello-Ochende\*

**Multi-scale pin fins: Scale analysis and mathematical optimization of micro-pin fins arranged in rows**

DOI 10.1515/eng-2015-0023

Received October 09, 2014; accepted February 26, 2015

**Abstract:** This paper shows the performance of a cylindrical micro-pin fins with multiples-arrays structures for maximum heat transfer. The structures has a varying geometric sizes (diameter, height and spacing). The effects of Reynolds number and thermal conductivity ratio on the optimized geometric configurations and the maximum heat transfer rate is documented. Two design configuration were considered. Scales and computational fluid dynamics analysis shows that the benefits of varying fin height is minimal. Results show that performace is increased when three rows of micro pin fin heat sinks with a reduced degree of freedom (fixed height) when compared to two rows of micro pin fins heat sink for the same amount of material. The optimized diameters of the fins seems to have greatest effect on performace of the heat sink.

**Keywords:** thermal conductivity; heat transfer rate; gradient-based; geometry; micro-pin fin; constructal design

**Nomenclature**

$C_p$	Specific heat transfer, [J/kg]
$D$	Pin diameter, [m]
$h$	heat transfer coefficient, [W/m <sup>2</sup> K]
$H$	Pin height, [m]
$k$	Thermal conductivity, [W/m.K]
$L$	Length, [m]
$L_1$	Width, [m]
$n$	numbers of rows [-]
$P$	Pressure, [Pa]
$q$	Rate of heat transfer, [W/m <sup>2</sup> ]
$Q$	Dimensionless heat transfer rate, [-]
$Re$	Reynolds number base on axial length, L[-]

$R_{th}$	Thermal Resistance, [K/W]
$s$	Interfin spacing, [m]
$T$	Temperature, [K]
$U$	Velocity, [m/s]
$u, v, w$	Velocities in the $x, y, z$ directions, [m/s]
$V$	Volume, [m <sup>3</sup> ]
$x, y, z$	Cartesian coordinates, [m]
Special characters	
$\Delta$	Difference, [-]
$\mu$	Dynamic viscosity, [kg/m.s]
$\rho$	Density, [kg/m <sup>3</sup> ]
$\gamma$	Thermal conductivity ratio, [-]
$\lambda$	Lagrange multiplier, [-]
Subscripts	
1	First fin row
2	Second fin row
3	Third fin row
$f$	Fluid
$inlet$	Inlet
$max$	Maximum
$opt$	Optimum
$r$	Ratio
$s$	Solid
$w$	Wall
0	Free stream

**1 Introduction**

In the last decade there has been a considerable increase in power and ability of various devices and machinery. New concepts and ideas pushed for more versatile, efficient and powerful devices to be used to address rising requirements in industry. More power and ability also introduces the problem of an increase of heat of the various components of these devices. Primarily, these components would be the transistors and various other electronic components in electronic devices; heat exchangers found in industrial applications and other plant and equipment such turbines. Each of these components generates a considerable amount of heat due to the nature of their use, the fluids which they handle and their designs.

\*Corresponding Author: Tunde Bello-Ochende: Department of Mechanical Engineering, University of Cape Town, Private Bag X3, Rondebosch, 7701, South Africa, E-mail: tunde.bello-ochende@uct.ac.za

Micro pin-fin heat sinks are the more dominant in the micro heat sink category as they prove to yield increased heat dissipation characteristics under severe space and acoustic restraints [1]. Nevertheless, design considerations which include material selection, size and compactness greatly influences the heat dissipation rates that can be achieved by these heat sinks. A new evolutionary design methodology known as constructal design handles all this design consideration in a simple manner [2–4].

[5] investigated the convective heat transfer and pressure drop phenomenon across a pin-fin micro heat sink by comparing its thermal resistance to that of a micro channel heat sink. They discovered that the thermo-hydraulic performance of a cylindrical micro pin-fin heat sink is superior to that of a micro channel heat sink as very high heat fluxes can be dissipated with low wall temperature rises across the heat sink. Their results showed that for fin diameters larger than  $50 \mu\text{m}$ , the thermal resistance is less sensitive to changes in the fin diameter and for increased efficiency short pins should be used.

[1] optimized a fin heat sink by finding optimal geometric design parameters that minimize the entropy generation rate for both an in-line and staggered configuration. In-line arrangements gave lower entropy generation rates for both low and high thermal conductivity heat sink cases.

In a further study by [6], the effects of geometric factors on the optimal design performance of pin-fin heat sinks were examined by using the entropy generation minimization scheme. They found that the thermal resistance of these heat sinks increases with an increase in the side and top clearance ratios resulting in a decrease in the entropy generation rate. They also documented that the pin height has an effect on the optimal entropy generation rate of heat sinks. [7], conducted a comparative study into the heat transfer performance of various fin geometries. The study consisted of fins having round, elliptical and plate cross sections both for in-line and staggered configurations. They found that round geometries out-performed sharp-edged fin shapes with the circular fin shape yielding the highest Nusselt number and that of the parallel plate having the lowest Nusselt number for the  $110 \leq Re \leq 1320$  range considered. It was also found that at lower pressure drops, elliptical fins provide the best heat transfer performance with the circular fins taking over at higher pressure drops. Parallel plates however offered the best performance in terms of pressure drop and pumping power requirement.

[8] developed steady-state correlations predicting heat transfer performances of in-line and staggered pin-fins from which they found optimal designs. They revealed a

dimensionless optimal pin-fin pitch in the span-wise and stream-wise direction of 0.135 and 0.173 respectively for the in-line arrangement. For the staggered arrangement, this dimensionless parameter was found to be 0.19 and 0.1 respectively. [9] developed a response surface methodology to find the optimal design parameters of a pin-fin heat sink. They documented that the fin height and fin diameter are the main factors that affect the thermal resistance of the heat sink while the pitch influences its pressure drop requirements. The conclusion that the most important design parameters affecting the thermal performance of pin-fin heat sink are the fin-diameter and height was also supported by [10]. Their work entailed an optimal design of pin-fin heat sink using a grey-fuzzy logic based on orthogonal arrays.

This work seeks to determine the optimal geometric configuration of a multi-scale micro-pin fin heat sink which will result in the maximal heat transfer rate. The resulting heat transfer across the cylindrical micro-pin fins is by laminar forced convection of uniform, isothermal free stream. The process is carried out using a gradient based mathematical optimization under total fixed volume and manufacturing constraints. It's important to note that the work covered in this paper follows that of [11]. The difference lies in the fact that the constructal design methodology has been combined with mathematical optimisation and applied to a known micro-pin fins heat sink with two and three rows.

## 2 Model

Consider a cylindrical micro pin fins heat sink consisting of multiple rows of fins as shown in Figure 1a. The flow assembly consist of rows of micro pin fins with diameter  $D_1, D_2, D_3, D_4, D_5 \dots D_n$ , and heights  $H_1, H_2, H_3, H_4, H_5, \dots H_n$ , spaced at distance  $s_1, s_2, s_3, s_4, \dots s_n$ , from each other with the aims to enhance the extractions of heat at the base of the thermal conductive materials. The swept length is  $L$ , and it is fixed. The flow assembly is bathed by a free stream that is uniform and isothermal with temperature  $T_0$  and velocity  $U_0$ , because of symmetry we select an elemental volume comprising of two, three cylindrical micro pin fins on the swept length  $L$  and width  $L_1$  as shown in Figure 1b. A heat sink with dimensions of  $1 \text{ mm} \times 0.6 \text{ mm} \times 1 \text{ mm}$  is used for the numerical computation. The base of the heat sink is supplied with heat at a uniform temperature  $T_w$ . The respective continuity, momentum and energy equations governing the fluid flow and heat transfer for the cooling

fluid within the heat sink are:

$$\nabla(\rho U) = 0 \quad (1)$$

$$\rho(U \cdot \nabla U) + \Delta P - \mu \nabla^2 U = 0 \quad (2)$$

$$\rho C_p(U \cdot \nabla T) - k_f \nabla^2 T = 0. \quad (3)$$

For the solid material, the momentum and energy governing equations are:

$$U = 0, \quad k_s \nabla^2 T = 0, \quad (4)$$

where  $U$  is the velocity vector,  $C_p$ , the specific heat of the fluids,  $\mu$  the dynamic viscosity and  $k_f$  and  $k_s$  the thermal conductivities of the fluid and solid. These conservation equations are solved over the fully discretized domain. A one-dimensional uniform velocity with constant temperature is assumed at the inlet:

$$u(x, y, 0) = v(x, y, 0) = 0;$$

$$w(x, y, z, 0) = U_0;$$

$$T(x, y, 0) = T_0. \quad (5)$$

Zero normal stress at the outlet. No-slip, no-penetration boundary condition is enforced on the fin and wall surfaces. Symmetry boundary condition is applied to the domain to reasonably represent the physical and geometric characteristics of flow through pin-fin arrays. A constant wall temperature  $T_w$  is imposed at the bottom of the micro pin-fin. Uniform isothermal free stream (air) is used as the working fluid. Other flow-related assumptions implemented include steady flow, laminar flow, incompressibility and constant fluid and material properties.

The objective function or the measure of goodness of the design is the total heat transfer rate. The dimensionless rate of heat transfer from the hot solid to the cold fluid is expressed as

$$Q = \frac{q/L}{k_f(T_w - T_0)}, \quad (6)$$

where  $q$  is the overall rate of heat transfer,  $T_w$  and  $T_0$  are the wall and free-stream temperatures respectively.

### 3 Numerical formulation and optimization

In this section the mass, momentum and energy conservation Equations (1)-(5) are solved over the discretized domain shown using the finite volume software<sup>1</sup> coupled with the above-mentioned boundary conditions. A

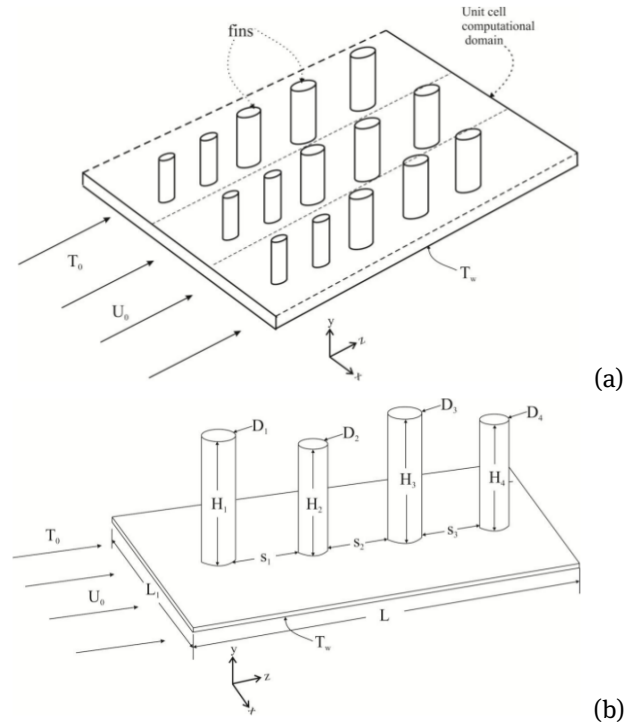


**Figure 1:** (a) Physical model of micro finned heat sink. (b) Computational model of micro finned heat sink.

second-order upwind scheme was used in discretizing the momentum equation while a SIMPLE algorithm was used for the pressure velocity coupling. Convergence criteria were set to less than  $1 \times 10^{-4}$  for continuity and momentum residuals while the residual of energy was set to less than  $1 \times 10^{-7}$ .

In order to verify the numerical model developed, grid independence tests were carried out on the pin-fin heat sink. For the two row configuration, the test was carried out on the pin-fin heat sink, whose dimensions are given in Table 1. The analysis was conducted for various control volume mesh sizes until the deviation in dimensionless heat transfer rate  $Q$  was negligible with the finest mesh consisting of 615 000 cells. The maximum average difference of  $Q$  encountered when using a mesh having greater than 159 768 cells was 2.2%, giving the confidence that the simulations carried out based on a 178 488-celled mesh provide satisfactory numerical accuracy.

The validation of the CFD<sup>1</sup> code used was carried out by comparing the numerical results obtained using this code with the analytical results obtained from the investigation carried out by [12] who analysed the performance of a cylindrical pin fin heat sink in laminar forced convection using thermal resistance network. The solution trends were in agreement with previous work [12] with a relative

<sup>1</sup> Fluent Inc., Fluent Version 6 Manuals, Centerra Resource Park, 10 Cavendish Court, Lebanon, New Hampshire, USA, 2001.

difference of between 5% to 21% as shown in Table 2a and 15% to 18% in Table 2b.

For the three row configuration, three mesh sizes of 147 546 cells, 182 358 cells and 605 300 cells respectively were used for the verification procedure, it was found that the maximum difference in the dimensionless rate of heat transfer  $Q$  between the three mesh sizes is <1%. This gives confidence that a mesh with 182 358 cells will give satisfactory accuracy in the prediction of the heat transfer across the fin array.

### 3.1 Optimization problem

The objective of the optimization problem is to find the best geometric configuration of pin diameter, fin height (for case one) and inter fin spacing that will maximize the rate of heat transfer from the solid to the fluid. The automated optimization problem was carried out in MATLAB<sup>2</sup> coupled with the DYNAMIC-Q algorithm [13, 14], the mesh generation code GAMBIT<sup>1</sup> and a finite volume code<sup>1</sup>. Detailed discussion of the optimization procedure is outlined in reference [10, 15, 16].

### 3.2 Constraints

**Total Fin Volume Constraint:** In heat sink design, weight and material cost of fins are limiting factors. Therefore, the total volume of the cylindrical fins is fixed to a constant value.

$$\begin{aligned} V &= V_1 + V_2 + \dots + V_n = \text{constant} \\ \therefore \sum V_i &= \text{Constant} \\ \sum \frac{\pi D_i^2}{4} H_i &= C \\ \sum D_i^2 H_i &= \frac{4C}{\pi} \\ \text{for } i &= 1, 2 \text{ and } 3 \dots n, \end{aligned} \quad (7)$$

where  $V$  is the volume of the fins and  $n$  the numbers of rows of fins, and  $C$  a constant associated with the volume. **Manufacturing Restraint:** Pin-fin manufacturing and size constraint allows for typical aspect ratios in the range of 0.5 and 4 [17, 18]. Considering fabrication techniques, inter fin spacing is limited to 50 microns [19, 20].

## 4 Scale analysis

Consider Figure 1a, let  $z$  be the fin positions along the plate and  $h$  be the heat transfer coefficient, the question how should rows of sequential fins be sized? We need to make the shape of each fin so that each fin is of minimum weight that is maximum heat transfer rate density. Using scale analysis, at the point of optimal configuration the scale of convective heat transfer scales as that of conduction heat transfer from the fin, using the procedure outline for two pin fins [2] for multi-scale fins with five row, we have mathematically,

$$k_s D^2 \frac{\Delta T}{H} \sim h D H \Delta T. \quad (8)$$

Next, if  $h$  depends on the fin position  $z$  along the plate such that  $h_1(z_1) \neq h_2(z_2) \neq h_3(z_3) \neq h_4(z_4) \neq h_5(z_5)$ . The total heat transfer from the fins scale as

$$\begin{aligned} & \left( h_1 D_1 H_1 \Delta T_1 + h_2 D_2 H_2 \Delta T_2 + h_3 D_3 H_3 \Delta T_3 \right. \\ & \quad \left. + h_4 D_4 H_4 \Delta T_4 + h_5 D_5 H_5 \Delta T_5 \right) \quad (9) \\ & \sim k_s \left( \frac{D_1^2}{H_1} \Delta T_1 + \frac{D_2^2}{H_2} \Delta T_2 + \frac{D_3^2}{H_3} \Delta T_3 \right. \\ & \quad \left. + \frac{D_4^2}{H_4} \Delta T_4 + \frac{D_5^2}{H_5} \Delta T_5 \right). \end{aligned}$$

Assuming that,

$$\Delta T_1 \sim \Delta T_2 \sim \Delta T_3 \sim \Delta T_4 \sim \Delta T_5 = \Delta T. \quad (10)$$

Where  $\Delta T$  is the temperature between successive fins, Equation (9) is to be maximized subject to the total volume, scales as  $D_1^2 H_1 + D_2^2 H_2 + D_3^2 H_3 + D_4^2 H_4 + D_5^2 H_5$ . We seek the extremum of

$$\begin{aligned} \phi &= \frac{D_1^2}{H_1} + \frac{D_2^2}{H_2} + \frac{D_3^2}{H_3} + \frac{D_4^2}{H_4} + \frac{D_5^2}{H_5} \\ &+ \lambda \left( D_1^2 H_1 + D_2^2 H_2 + D_3^2 H_3 + D_4^2 H_4 + D_5^2 H_5 \right), \end{aligned} \quad (11)$$

where  $\lambda$  is the Lagrange multiplier. From Equation (8) we find that the diameter of each fin must scale as

$$\frac{D}{H^2} \sim \frac{h}{k_s}. \quad (12)$$

From Equations (9) and (10) we have

$$\begin{aligned} \phi &= \\ & \left( D_1^{3/2} h_1^{1/2} + D_2^{3/2} h_2^{1/2} + D_3^{3/2} h_3^{1/2} + D_4^{3/2} h_4^{1/2} + D_5^{3/2} h_5^{1/2} \right) \\ & + \lambda \left( D_1^2 h_1^{-5/2} + D_2^2 h_2^{-5/2} + D_3^2 h_3^{-5/2} + D_4^2 h_4^{-5/2} + D_5^2 h_5^{-5/2} \right). \end{aligned} \quad (13)$$

<sup>2</sup> The MathWorks, Inc., MATLAB & Simulink Release Notes for R2008a, 3 Apple Hill Drive, Natick, MA, 2008.

**Table 1:** Heat sink dimensions used for the code validation process

$D_1$ (mm)	$D_2$ (mm)	$H_1$ (mm)	$H_2$ (mm)	$s$ (mm)	$L_1$ (mm)	$L$ (mm)	$H_T$ (mm)
0.15	0.25	0.3	0.6	0.2	0.6	1	1

**Table 2:** Validation of code for thermal resistance versus (a) pin diameter (b) pin height

(a)				
$D$ (mm)	Present Study $R_{th}$ (K/W)	[12] $R_{th}$ (K/W)	Relative Difference	
1.0	122	148	0.21	
1.5	92	92	0.00	
2.0	66	66	0.00	
2.5	51	48	0.05	
(b)				
$H$ (mm)	Present Study $R_{th}$ (K/W)	[12] $R_{th}$ (K/W)	Relative Difference	
6	127	104	0.18	
8	96	80	0.17	
10	78	66	0.15	
12	66	56	0.15	
14	59	50	0.15	

Minimizing  $\phi$  with respect to  $D_1, D_2, D_3, D_4, D_5$  we have and, that

$$\begin{aligned}
 D_1 &= -\frac{3h_1}{5\lambda}, D_2 = -\frac{3h_2}{5\lambda}, D_3 = -\frac{3h_3}{5\lambda} \\
 D_4 &= -\frac{3h_4}{5\lambda}, D_5 = -\frac{3h_5}{5\lambda} \\
 \text{and } \frac{D_2}{D_1} &= \frac{h_2}{h_1}, \frac{D_3}{D_2} = \frac{h_3}{h_2}, \frac{D_4}{D_3} = \frac{h_4}{h_3}, \frac{D_5}{D_4} = \frac{h_5}{h_4}.
 \end{aligned}
 \tag{14}$$

$$\left( \frac{D_2}{D_1} \sim \left( \frac{\Delta T_2}{\Delta T_1} \right) \leq 1, \frac{D_3}{D_2} \sim \left( \frac{\Delta T_3}{\Delta T_2} \right) \leq 1, \right.$$

$$\left. \frac{D_4}{D_3} \sim \left( \frac{\Delta T_4}{\Delta T_3} \right) \leq 1, \frac{D_5}{D_4} \sim \left( \frac{\Delta T_5}{\Delta T_4} \right) \leq 1, \right) \tag{18}$$

for  $\Delta T_1 \geq \Delta T_2 \geq \Delta T_3 \geq \Delta T_4 \geq \Delta T_5$ .

From Equation (10) we have that

$$\begin{aligned}
 \frac{D_1}{H_1^2} &\sim \frac{h_1}{k_s}, \frac{D_2}{H_2^2} \sim \frac{h_2}{k_s}, \frac{D_3}{H_3^2} \sim \frac{h_3}{k_s} \\
 \frac{D_4}{H_4^2} &\sim \frac{h_4}{k_s}, \frac{D_5}{H_5^2} \sim \frac{h_5}{k_s}.
 \end{aligned}
 \tag{15}$$

Combining Equations (12) and (13) we have that the scale of the height ratio is

$$\frac{H_2}{H_1} \sim \frac{H_3}{H_2} \sim \frac{H_4}{H_3} \sim \frac{H_5}{H_4} \sim 1.
 \tag{16}$$

Similarly [2], if we make the assumption that the convective coefficients is nearly the same (implying that the diameters are nearly the same) for all the fins locations and we maximizes Equation(9) subject to the volume constraints we have that,

$$\begin{aligned}
 \left( \frac{H_2}{H_1} = \left( \frac{\Delta T_2}{\Delta T_1} \right)^{1/2} \leq 1, \frac{H_3}{H_2} = \left( \frac{\Delta T_3}{\Delta T_2} \right)^{1/2} \leq 1, \right. \\
 \left. \frac{H_4}{H_3} = \left( \frac{\Delta T_4}{\Delta T_3} \right)^{1/2} \leq 1, \frac{H_5}{H_4} = \left( \frac{\Delta T_5}{\Delta T_4} \right)^{1/2} \leq 1, \right) \tag{17}
 \end{aligned}$$

The scale analysis result is a useful guide in mathematical optimization that would be discuss in the next section. For the numerical optimization the number of rows would be limited to three.

## 5 Numerical results

### 5.1 Double row configuration

For the case when n is equal to two (double row), the optimization procedure was conducted using the DYNAMIC-Q algorithm for Reynolds numbers ranging from 30 to 411 with the effect of Reynolds number Re on the pin-fin geometry. Geometric configuration and heat transfer capabilities are investigated for the heat sink shown in Figure 1b. Figure 2a shows that the optimal fin-height ratio is in general independent of Reynolds number. This is evident in the insignificant change of the optimal fin-height ratio over the Re. This implies that for maximum heat transfer, the pin-fins in the first row should be slightly higher than

the fins in the next row, these results also agrees with the scale analysis prediction that  $\frac{D_2}{D_1} \sim \left(\frac{H_2}{H_1}\right)^2 = \frac{\Delta T_2}{\Delta T_1} \leq 1$ , we can see that the aspect ratio of all the geometric parameters are less than 1 as shown in Figures 2a and 3a respectively.

Results obtained from the optimization problem show that the optimal spacing  $s_{opt}$  between the pin-fins remains unchanged regardless of the Reynolds number value applied across the length of the control volume. This constant value coincides with the allowable spacing due to manufacturing restraints.

Figure 2a also shows a small increase in the optimal fin-diameter ratio with Reynolds number. With an error of less than 1%, the results can be correlated as:

$$\left(\frac{D_2}{D_1}\right)_{opt} = 0.464Re^{0.0314}. \quad (19)$$

The results further imply that the non-uniformity of the diameters of fins in the various rows plays a vital role in the heat transfer rate of pin-fins heat sinks. Furthermore, the results show that at lower  $Re$ , the diameter of the pin-fins in the first row should be about twice the diameter of those in the second row in order to achieve the maximum heat transfer rate, while at higher Reynolds numbers it should be about 1.8 times the diameter of those in the second row.

Figure 2b establishes the fact that the optimal rate of heat transfer increases with an increase in Reynolds number. This relationship between the maximum (optimal) dimensionless rate of total heat transfer  $Q$  and Reynolds number can be given by the expression:

$$Q_{max} = \sigma Re^{0.323}, \quad (20)$$

where  $\sigma$  is a constant dependent on the thermal conductivity ratio  $\gamma$  and the micro pin geometry. The thermal conductivity ratio is simply the ratio of the solid's thermal conductivity to that of the fluid's ( $\gamma = k_s/k_f$ ). The correlation given in Equation (20) correlates with an error of less than 1% to the CFD results produced and it is in agreement with the work published by [11]. For a fixed thermal conductivity ratio of 100 and for microscale applications, the constant  $\sigma$  was found to be 9.78.

The effect of the thermal conductivity ratio  $\gamma$  on the maximized rate of heat transfer and the geometrical ratio of the micro-pin fins was investigated. Figure 3a show that the thermal conductivity ratio has no effect on the pin-fin-diameter ratio and height ratio. Their aspect ratio is less than or equal to one as predicted in Equations (16), (17) and (18).

Figure 3b shows that the maximized rate of heat transfer increases as the thermal conductivity ratio increases. However, at higher thermal conductivities ( $\gamma > 1000$ ), the

rate of heat transfer approximately reaches a maximum and as the thermal conductivity ratio increases, the heat transfer rate is invariant with  $\gamma$ . This is due to the fact that convection rather than conduction is the more dominant medium thus rendering the thermal conductivity property of little importance.

## 5.2 Triple row configuration

In case two that is when  $n$  equal to three, the vertically arranged micro pin-fins form part of a three-row-finned array with row-specific diameters  $D_1$ ,  $D_2$  and  $D_3$  respectively. The various rows are spaced by a distance  $s_1$  and  $s_2$  as depicted in Figure 1b. Uniform row height assumption was made (from results obtained from  $n = 2$  and scale analysis). Therefore,  $H_1 = H_2 = H_3$ .

The optimized geometric parameters (Figure 4a) predict that pin-fins in the first row  $D_1$  should be larger than the pin-fins in the next row with this decreasing diameter trend continuing to the third row. It further shows that the optimal trend of the respective pin diameters  $D_1$ ,  $D_2$  and  $D_3$  changes slightly as the Reynolds number across the finned array increases. It indicates that as the fluid velocity is increased, the pin diameter of the fins in the first row decreases slightly while the diameter of the fins in the third row increases slowly. The pin diameters in the penultimate row show independence with regard to an increasing  $Re$ .

An optimal search of the geometric parameters of the heat sinks that maximizes the heat transfer rate showed that as the Reynolds number increases, the dimensionless heat transfer rate also increases. The results are shown in Figure 4b; it explains the fact that the convective heat transfer coefficient is a strong function of the fluid velocity. For a thermal conductivity ratio of 100, the relationship between Reynolds number and the maximal rate of heat transfer can be correlated within an error of 1% as:

$$Q_{max} = 8.45Re^{0.375}. \quad (21)$$

The effect of various materials on the maximised rate of heat transfer of the heat sink was also investigated.

From Figure 5a, results show that for a Reynolds number of 123, the pin diameters for each row stay constant with an increase in the conductivity ratio  $\gamma$ . This result implies that solid-fluid medium combination is insignificant with regard to the geometric design of such heat sinks. It shows that the design is robust with respect to the conductivity ratio. In addition, it is intuitive that the minimum allowable spacing due to manufacturing constraints of  $50 \mu\text{m}$  is the optimal spacing separating the pin-fins in the various rows.

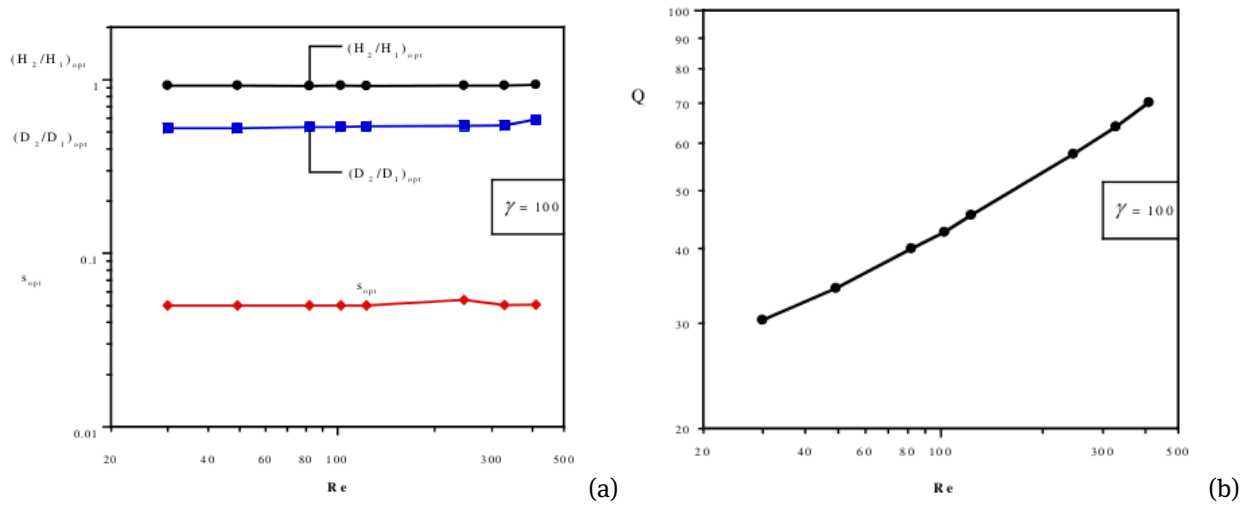


**Figure 2:** (a) The influence of Reynolds number on the optimized geometric configuration, for thermal conductivity ratio of 100 for double row finned heat sink. (b) The maximized rate of heat transfer as a function of Reynolds number with the conductivity ratio  $\gamma$  equal to 100 for double row finned heat sink.

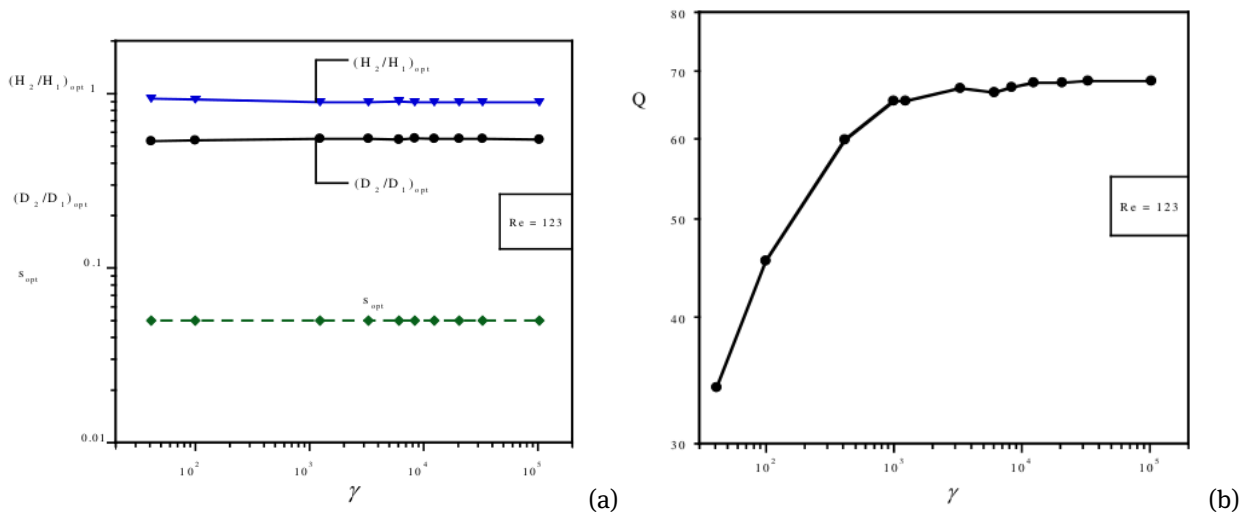
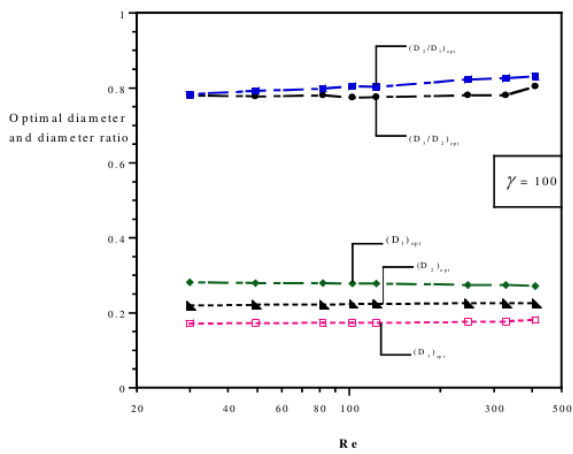
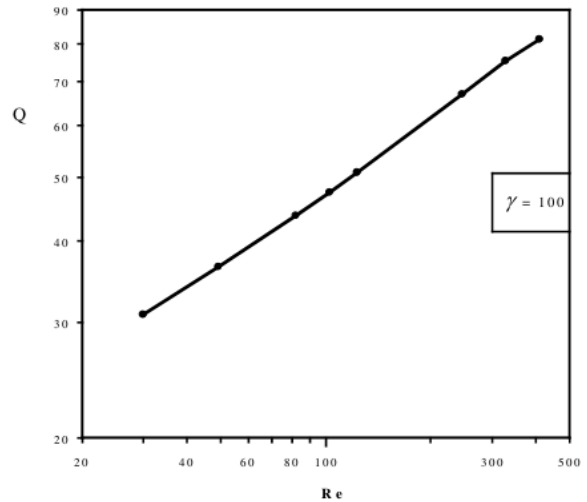


**Figure 3:** (a) The effect of the thermal conductivity ratio on the optimized geometric configuration of a double row finned heat sink at a Reynolds number of 123. (b) The effect of the thermal conductivity ratio on the maximized rate of heat transfer at a Reynolds number of 123.

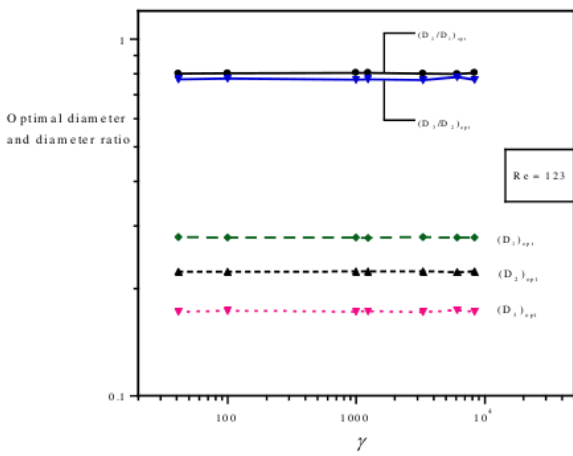


(a)

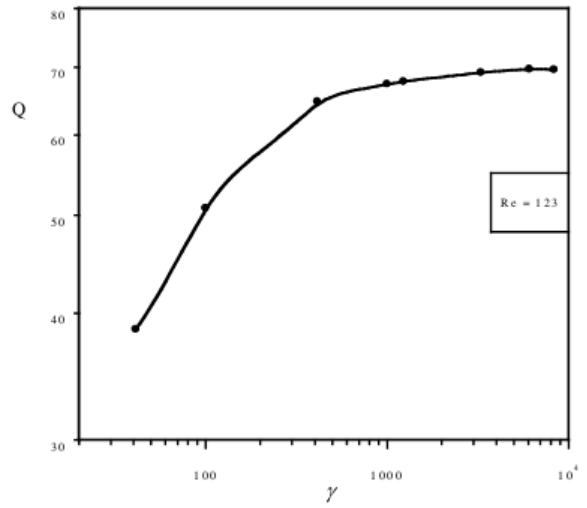


(b)

**Figure 4:** (a) The relationship between the optimal configurations for each fin row as a function of Reynolds number for triple rows for a thermal conductivity ratio of 100. (b) The relationship between the optimal dimensionless rate of heat transfer and Reynolds number for a triple row heat sink for a thermal conductivity ratio of 100.



(a)



(b)

**Figure 5:** (a) The effect of the thermal conductivity ratio on the optimized geometric Configurations for a triple row finned heat sink at a Reynolds number of 123. (b) The effect of the conductivity ratio on the maximized heat transfer rate for a triple row micro heat sink for a Reynolds number of 123.

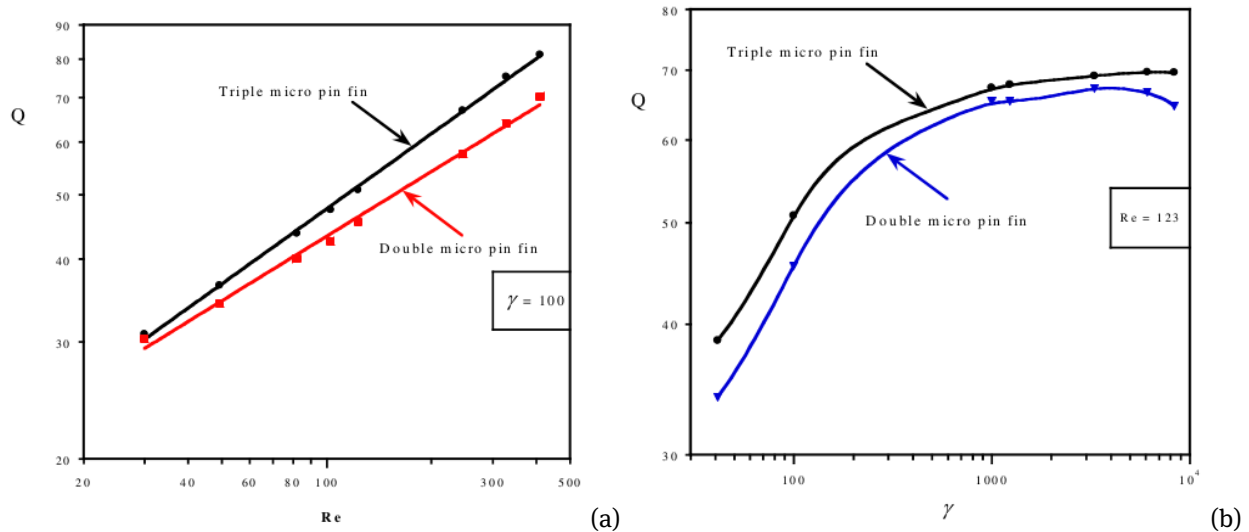


**Figure 6:** (a) The effect of Reynolds number on the maximum heat transfer for both the optimized double row micro-pin fins and triple row micro-pin fins heat sink. (b) The effect of conductivity ratio on the heat transfer for both the optimized double row micro-pin fins and triple row micro-pin finned heat sink.

**Table 3:** Optimal results for various computational widths.

$L_1$ (mm)	$D_2/D_1$	$D_3/D_2$	$Q$
0.4	0.799	0.792	52.3
0.5	0.779	0.782	50.9
0.6	0.802	0.775	50.8
0.8	0.786	0.797	52.7

Figure 5b further shows that an increase in the thermal conductivity ratio  $\gamma$  causes an increase in the maximal heat transfer rate. However, varying gradients of the dimensionless heat transfer rate as a function of  $\gamma$  are experienced with higher positive gradients experienced at lower  $\gamma$  (less than 500) and almost zero gradients for conductivity ratios greater than 1000. The results suggest that a heat sink designed to operate within a medium where the conductivity ratio is about 400 will perform very well and increasing the conductivity ratio will not significantly increase the dimensionless heat transfer rate.

Table 3 shows the optimal parameters for various computational widths. The results show that optimal geometric design parameters are insensitive to the computational width.

### 5.3 Comparison between triple rows micro-pin fins to double row pin fins

Figures 6a and 6b show the effect of Reynolds number and conductivity ratio on the heat transfer for both the

optimized double row fins and triple row micro pins, it is observed that as the Reynolds number increases the heat transfer rate also increases. The triple rows pin fins have a larger heat transfer rate when compared to the double rows micro pin fins for the same amount of material. The same behaviour is observed for Figure 6b, that the triple rows micro pin fins give a higher heat transfer as the thermal conductivity ratio increases. It was found that by adding a third row of pin-fins, the rate of heat transfer is enhanced with enhancement greater than 10% achievable for  $Re > 100$ . However, the enhancement rate decreases at higher thermal conductivity ratio  $\gamma$ .

## 6 Conclusion

This work has demonstrated the effective use of mathematics optimization coupled with geometric constraints for the design of optimum micro-pin fins heat sinks for maximum heat removal capabilities. The numerical optimization technique implemented shows that variable geometry in the various rows of a finned array will bring about maximized rate of heat transfer. However, it was discovered that the influence of non-uniform fin height to the optimal solution is quite negligible. The maximized heat transfer rate is a result of a balanced conduction-convection ratio. Results also proved that thermal conductivity ratio does not influence the optimal geometrical configuration of such heat sinks. It was found that by adding a third row of pin-fins with a reduced degree of freedom, the rate of heat transfer

is enhanced with enhancement greater than 10% achievable for  $Re > 100$ . Future work will include inserting the micro-pin fins of different cross-sectional shape inside a micro-channel heat sink and relaxing the axial length. The optimal design of micro-pin fins heat sink is expected to facilitate the heat flow for maximum heat transfer in the design of heat exchangers for the cooling of electronic devices.

**Acknowledgement:** The author acknowledges Mr F.U. Ighalo, Profs J.P. Meyer and Adrian Bejan for their contribution to this work, and the South African National Research Foundation (NRF) for its financial support.

## References

- [1] Khan W.A., Culham J.R., Yovanovich M.M., Optimization of pin-fin heat sinks using entropy generation minimization, *IEEE Trans. Compon. Packag. Technol.*, 2005, 28, 1–13.
- [2] Bello-Ochende T., Meyer J.P., Bejan A., Constructal ducts with wrinkled entrances *Int. J. Heat Mass Transfer*, 2009, 53, 3628–3633.
- [3] Bello-Ochende T., Meyer J.P., Ighalo F.U., Combined numerical optimization and constructal theory for the design of heat sinks, *Numer. Heat Tran. A*, 2010, 58, 1–18.
- [4] Lorenzini G., Biserni C., Garcia F.L., Rocha L.A.O., Geometric optimization of a convective T-shaped cavity on the basis of constructal theory, *Int. J. Heat Mass Transfer*, 2012, 5(23-24), 6951–6958.
- [5] Peles Y., Koşar A., Mishra C., Kuo C., Schneider B., Forced convective heat transfer across a pin fin micro heat sink, *Int. J. Heat Mass Tran.*, 2005, 48, 3615–3627.
- [6] Khan W.A., Yovanovich M.M., Optimization of pin-fin heat sinks in bypass flow using entropy generation minimization method, (Proceedings of IPACK 2007), Vancouver, Canada, 2007.
- [7] Soodphakdee D., Behnia M., Copeland D.W., A comparison of fin geometries for heatsinks in laminar forced convection: Part I - round, elliptical, and plate fins in staggered and in-line configurations, *Int. J. Microcir. Elect. Packag.*, 2001, 24, 68–76.
- [8] Tahat M., Kodah Z.H., Jarrah B.A., Probert S.D., Heat transfers from pin-fin arrays experiencing forced convection, *Appl. Energ.*, 2000, 67, 419–442.
- [9] Chiang K., Chang F., Application of response surface methodology in the parametric optimization of a pin-fin type heat sink, *Int. Comm. Heat Mass Tran.*, 2006, 33, 836–845.
- [10] Chiang K., Chang F., Tsai T., Optimum design parameters of pin-fin heat sink using the grey-fuzzy logic based on the orthogonal arrays, *Int. Comm. Heat Mass Tran.*, 2006, 33, 744–752.
- [11] Bello-Ochende T., Meyer J.P., Bejan A., Constructal multi-scale pin-fins, *Int. J. Heat Mass Transfer* 2010, 53, 2773–2779.
- [12] Khan W.A., Culham J.R., Yovanovich M.M., Performance of shrouded pin-fin heat sinks for electronic cooling, *J. Thermophys. Heat Transfer*, 2006, 20, 408–414.
- [13] Snyman J.A., *Practical Mathematical Optimization: An Introduction to Basic Optimization Theory and Classical and New Gradient-Based Algorithms*, Springer, New York, 2005.
- [14] Snyman J.A., Hay A.M., The DYNAMIC-Q Optimization Method: An Alternative to SQP? *Comput. Math. Appl.*, 2002, 44, 1589–1598.
- [15] Ighalo F.U., Optimization of Micro-channels and Micro-pin-fin Heat Sinks with Computational Fluid Dynamics in Combination with a Mathematical Optimization Algorithm, M.Eng. Thesis, University of Pretoria, South Africa, 2011.
- [16] Ighalo, F.U., Bello-Ochende, T., Meyer, J.P., Geometric optimization of multiple-arrays of micropin-fins, (Proceeding of the 8th ASME/JSME Thermal Engineering Joint Conference, AJTEC 2011), Honolulu, Hawaii, United States of America, 2011.
- [17] Achanta V. S., An experimental study of endwall heat transfer enhancement for flow past staggered non-conducting pin fin arrays, PhD Thesis, Department of Mechanical Engineering, Texas A & M University, U.S.A., 2003.
- [18] Lyall M.E., Heat transfer from low aspect ratio pin fins, PhD Thesis, Department of Mechanical Engineering, Virginia Polytechnic Institute and State University, 2006.
- [19] Husain A., Kim K., Shape optimisation of micro-channel heat sink for micro-electronic cooling, *IEEE Trans. Compon. Packag. Technol.*, 2008, 31, 322–330.
- [20] Li J., Peterson G.P., Geometric optimisation of a micro heat sink with liquid flow, *IEEE Trans. Compon. Packag. Technol.*, 2006, 29, 145–154.

## Research Article

## Open Access

Hugo Mercado-Mendoza and Sylvie Lorente\*

# Impact of the pore solution on the aqueous diffusion through porous materials

**Abstract:** This paper reviews the main advances of our group on the measurements of the diffusion coefficient through partially saturated porous materials. The technique that we developed is based on the definition of an equivalent electrical model reproducing the behavior of the porous microstructure. The electrical characteristics are measured by means of Electrochemical Impedance Spectroscopy. After validating the approach on saturated samples, the method was applied to partially saturated materials. We showed that the pore solution ionic composition has not impact on the results, and documented the effect of the pore size distribution on the macroscopic diffusion coefficient.

**Keywords:** porous media, pore network, saturation level, diffusion

DOI 10.1515/eng-2015-0013

Received October 31, 2014; accepted January 05, 2015

## 1 Introduction

The diffusion coefficient is a macroscopic parameter that depends on the characteristics of both the diffusing species and the porous material involved in the diffusion process [1–3]. This parameter is of extreme importance in several domains. In nuclear engineering, the confinement of nuclear waste is done by means of cement-based materials, and its success depends on knowing the diffusion coefficient. In civil engineering applications, species such as chloride may invade the pore network of the material,

reach the reinforcement bars of concrete structures and trigger the initiation of corrosion.

Most techniques rely still today on saturated samples [1, 4–11]. Yet, in-situ structures are hardly encountered in saturated state. There is a strong need, not only in the domain of civil engineering but also in nuclear engineering and nuclear waste disposal, to determine the relationship between aqueous diffusion coefficients and the saturation level of the materials. The objective of this paper is to review the progress made by our group in developing a technique based on Electrochemical Impedance Spectroscopy to determine the diffusion coefficient through non saturated porous materials.

## 2 Materials and methods

Two different kinds of materials were tested: TiO<sub>2</sub> samples as non-reactive porous material and cement pastes samples as reactive porous systems. The TiO<sub>2</sub> ceramics was chosen for being inert vis-à-vis chloride and alkali ions, unlike concrete. Their geometry was cylindrical (110 mm in diameter, 15 mm in thickness). The cement paste samples were based on type-I and type-V cement (i.e. blended cement) with water-to-cement ratio of 0.4 and 0.43 respectively. The samples were kept in humid chamber at controlled temperature of 20°C before being demolded after 24 hours. Then they were kept in the same chamber for several months. At the end of the curing period, the cylinders were sawed into thin samples. The materials microstructure was characterized through apparent density and water porosity measurements following the protocol [12]. Table 1 gives the results obtained as an average of three measurements.

**Hugo Mercado-Mendoza:** Laboratoire ICube (INSA / Université de Strasbourg), Département Mécanique, Equipe Génie Civil et Energétique, 2 rue Boussingault, F-67000 Strasbourg, France

**\*Corresponding Author: Sylvie Lorente:** Université de Toulouse, UPS, INSA, LMDC (Laboratoire Matériaux et Durabilité des Constructions), 135 Avenue de Ranguieu, F-31077 Toulouse Cedex 04, France, E-mail: lorente@insa-toulouse.fr

This paper was presented during 10th International Conference on Diffusion in Solids and Liquids, June 23-27, 2014, Paris, France.

**Table 1:** Microstructure characteristics.

Material	Apparent density, kg/m <sup>3</sup>	Water porosity
type-I paste	1580	0.39
type-V paste	1594	0.37
TiO <sub>2</sub>	3571	0.4

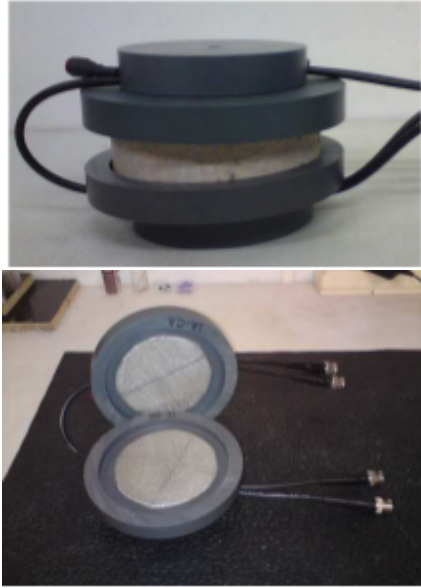


Figure 1: EIS cell.

Cement pastes samples were placed in chambers at controlled relative humidity until equilibrium before being tested with Electrochemical Impedance Spectroscopy. Impedance measurements were performed with an impedance analyzer (HP 4294A), with an amplitude of the sinusoidal voltage of 200 mV, and a frequency range of 40 – 110 10<sup>6</sup> Hz. The values of the measured impedance were plotted on Nyquist plots, before analysis. Each electrode was made of copper with a thin mattress of stainless steel, and protected by a PVC envelope (see Figure 1). The mattress of stainless steel was thick and flexible enough to ensure a very good contact with the sample when a light compression was applied between the two PVC containers. The test lasted less than five minutes per sample. Every result presented in this paper corresponds to an average of 3 to 4 tests, one test per day, in a room at constant temperature.

The Nernst-Einstein relation reads

$$\mu = \frac{zFD_{bulk}}{RT}, \quad (1)$$

where  $D_{bulk}$  is the diffusion coefficient in an infinitely diluted solution, and  $\mu$  is the ionic mobility, which is linked to the electrical conductivity  $\sigma$  through [13]

$$\mu = Fz\sigma. \quad (2)$$

The formation factor  $F_f$  is the ratio of the pore solution conductivity  $\sigma_{bulk}$  to the conductivity of the material saturated with the same pore solution  $\sigma_{mat}$ . This ratio is the same as the ratio of an ion diffusion coefficient in the pore solution

$D_{bulk}$  to the diffusion coefficient of the same ion through the material.

$$F_f = \frac{\sigma_{bulk}}{\sigma_{mat}} = \frac{D_{bulk}}{D}. \quad (3)$$

[14, 15] gave a very good overview on the applicability of the notion of formation factor to cementitious materials. Indeed the formation factor corresponds to a global factor characterizing the pore structure of the material.  $D_{bulk}$  is available in books of chemistry (e.g. [13]), while the material conductivity is obtained from

$$\sigma_{mat} = \frac{L}{AR_{mat}}, \quad (4)$$

where  $A$  is the sample cross-section, and  $R_{mat}$  is the saturated material electrical resistance. As shown in the next section the value of  $R_{mat}$  depends on the type of equivalent electrical circuit that is associated with the Nyquist diagram. Whatever the electrical model chosen, the impedance of the equivalent circuit is given by:

$$Z(\omega) = Z_{real}(\omega) + iZ_{imag}(\omega). \quad (5)$$

One of the biggest challenges in electrochemical impedance spectroscopy is to propose an electrical model that not only fits at best the experimental results, but also corresponds to an actual description of the material tested. The difficulty lies in the fact that the solution of the problem is not unique, meaning that several electrical circuits may correspond to the same diagram on the Nyquist plot [16, 17]. The circuit is made of the assembly in series of two blocks: one block describes the material, while the second one represents the electrodes and their interface. The latter is built as the assembly in parallel of a resistance  $R_E$  and a constant phase element  $Q_E$ . The material itself can be viewed as an assembly of simple electrical elements (Figure 2). It is represented by a combination in parallel of three ways to transfer electrical charges:

- The continuous conductive paths represent the fraction of opened and connected pores. They are represented by a resistance in the equivalent electrical model,  $R_{CCP}$  which is the material resistance we are interested in:  $R_{mat}$ .
- The solid matrix plays the role of non-ideal capacitor, modeled by a constant phase element  $Q_{mat}$ .
- The discontinuous pore paths are pore paths separated by solid layers. The association in series of a resistance  $R_{CP}$  and a constant phase element  $Q_{DP}$  represents this path, where CP means continuous portion and DP discontinuous point. The microstructure model is then associated in series with the block representing the contribution of the electrodes, as shown in Figure 2.

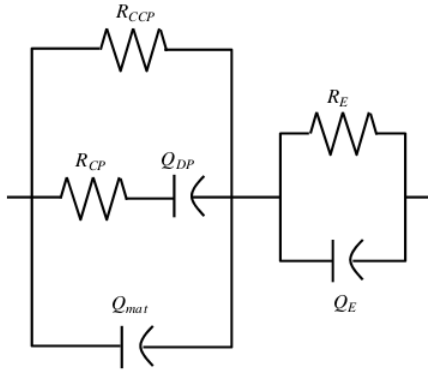


Figure 2: Electrical equivalent microstructural model.

Generally, the impedance of each simple element constituting the equivalent circuit is

$$Z(\omega) = R \quad (6)$$

for the resistance, and

$$Z(\omega) = \frac{1}{Q(i\omega)^\alpha} \quad (7)$$

for the constant phase element, where the constant  $Q$  is the equivalent capacitance ( $1/|Z|$ ) at  $\omega = 1$  rad/s. As a result, the equivalent impedance of the entire circuit is

$$Z(\omega) = \left( \frac{1}{R_{mat}} + \frac{1}{R_{CP} + \frac{1}{Q_{DP}(i\omega)^{\alpha_{DP}}}} + Q_{mat}(i\omega)^{\alpha_{mat}} \right)^{-1} + \left( \frac{1}{R_E} + Q_E(i\omega)^{\alpha_E} \right)^{-1}. \quad (8)$$

Equation (8) represents both the sample of material and the two electrodes constituting the experiment. This equation contains nine unknowns: the three resistances ( $R_{mat}$ ,  $R_{CP}$ ,  $R_E$ ), the three equivalent capacitances ( $Q$  terms), and the three  $\alpha$  factors appearing in the constant phase element expressions. The fitting procedure consists of solving the equation

$$Z(\omega) - Z_{exp}(\omega) = 0, \quad (9)$$

where the nine electrical characteristics ( $R$ ,  $Q$ ,  $\alpha$ ) are unknown. The optimization is based on the Simplex algorithm [18, 19]. The code was developed in the Matlab environment. Finally, once  $R_{mat}$  is obtained, the diffusion coefficient can be calculated from Equations (3) and (4).

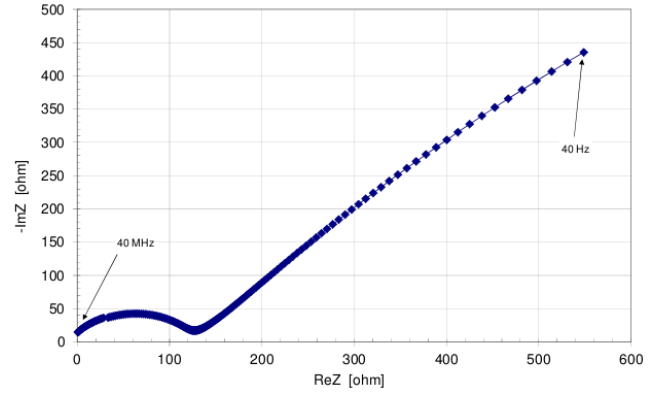


Figure 3: Example of EIS results on  $\text{TiO}_2$  sample.

### 3 Impact of the pore solution composition

Three samples of  $\text{TiO}_2$  disks were vacuum saturated (following the protocol [12]) with artificial solutions presented in Table 2.

Figure 3 presents an example of result corresponding to the EIS test of  $\text{TiO}_2$  sample. Note that the minimum of the imaginary part is obtained for a frequency of 61593 Hz, leading to an overall material resistance of  $126 \Omega$ . The capacitive branch measured in the lower frequencies highlight the effect of the interface between the electrodes and the material. The capacitive loop obtained above  $\omega_{mat}$  is typical of the material itself [20].

The samples saturated with the first two solutions were dried after the tests and vacuum saturated again with the same solution to which 20 g/L of NaCl was added. This led respectively to ionic strengths of 0.496 mol/L for solution 1 + NaCl, and 0.586 mol/L for solution 2 + NaCl.

The formation factor  $F_f$  was determined in each case from the EIS measurements. Its variation is small and in the range of discrepancy of the experiments. The results obtained are gathered in Figure 4. They show that the formation factor of this non-reactive material is not affected by a change in ionic strength, at least in the range of ionic strengths tested. Extending this result to the value of the diffusion coefficient of an ionic species thanks to Equation (3), means that the ionic diffusion coefficient will not vary when the ionic strength of the pore solution changes, thus will not vary when the pore solution concentration of the various ions in presence change. Such results are in agreement with previous works of our group (see for example [21] and [3]).

Table 2: Pore solutions

Solution	Na <sup>+</sup> (mol/m <sup>3</sup> )	K <sup>+</sup> (mol/m <sup>3</sup> )	OH <sup>-</sup> (mol/m <sup>3</sup> )	Ionic strength (mol/L)
Solution 1, from type-I cement paste	31.5	122.8	154.3	0.154
Solution 2, from type-V cement paste	70.6	173.9	244.6	0.245
Solution 3	127.6	510.6	638.3	0.638

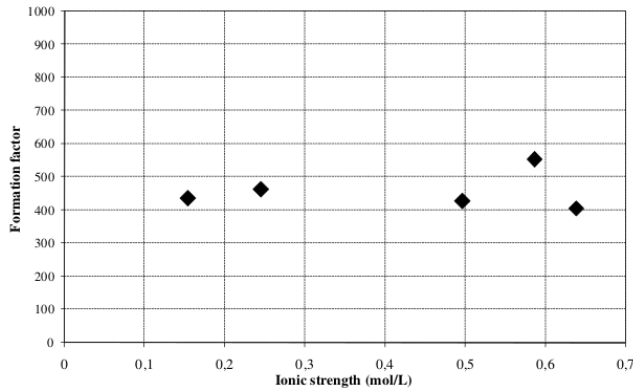


Figure 4: Formation factors as a function of the ionic strength.

## 4 Impact of the saturation level

We present in Figure 5 the EIS results obtained for the different water saturation levels,  $S_l$  in the case of a type I cement paste. Because a test lasts less than 5 minutes, we considered that the saturation state of the material remained constant during the experiment.

When the water saturation level  $S_l$  is 97.3%, the results plotted in the Nyquist diagram resemble the ones obtained in the fully saturated state. The two capacitive loops begin to appear clearly in the diagram when  $S_l = 0.67$ , while the inflexion of the experimental curve between the second capacitive arc and the part due to electrodes interface becomes smoother.

The diagram for  $S_l = 0.50$  exhibits a drastic change. One capacitive loop is still visible in the highest frequency while the other loop seems to be mixed with what was a tail due to the electrodes for higher water saturation levels. When  $S_l$  continues to decrease, the two capacitive arcs are not detectable anymore.

Figure 5 also shows the numerical Nyquist plots corresponding to the Simplex algorithm optimization. The model fits with very good accuracy the experimental results. The microstructure model chosen in this work is robust and describes the material behavior for all the water saturation levels studied.

From the strict viewpoint of determining an ionic diffusion coefficient, the parameter of interest is the one char-

acterizing the continuous conductive paths,  $R_{mat}$ . When the porous system is fully saturated or almost fully saturated, the  $R_{mat}$  resistance corresponds to the value of the equivalent circuit impedance for which the imaginary part is null, for a frequency located between the two extreme frequency values. This means that there is no need for a sophisticated model to obtain from the Nyquist diagram the information with which the sample diffusion coefficient can be calculated. Note that in practice the equivalent circuit impedance does not have a null imaginary part but rather reaches a minimum value.

As shown in Figure 5, the Nyquist diagram shape changes drastically when the water saturation level decreases. In this case, the electrical model is absolutely necessary because the resistance cannot be extracted directly from the plot, whereas  $R_{mat}$  remains a result from the microstructure-based model for any value of the water saturation level.

The values of the formation factor are presented in Figure 6 as a function of the water saturation level together with the chloride diffusion coefficient. The formation factor is a macroscopic parameter that accounts for the geometry of the porous system through the tortuosity of the network, its constrictivity and connectivity [22, 23]. We see from Figure 6 that it does not remain a constant because its value depends on the electrical conductivity of the pore network; this is why the formation factor gives not only a global image of the pore network geometry but also of the saturation state of the material.

The chloride diffusion coefficient decreases regularly with the saturation level as it can be seen on the log diagram, which means that there is continuity in the liquid fraction all over the sample. From a fully saturated state to  $S_l = 0.18$ , the chloride diffusion coefficient decreases by three orders of magnitude, moving from about  $1.8 \times 10^{-11} \text{ m}^2/\text{s}$  to  $5.5 \times 10^{-15} \text{ m}^2/\text{s}$  in the case of the type I cement pastes. The decrease in the diffusion coefficient is sharper in the case of the cement pastes with mineral additions (type V). The diffusion coefficient is of the same order of magnitude when the samples are saturated, but one order of magnitude lower than the type I pastes when the saturation level is of 20%, even though the water porosity of the samples is identical. The difference in results is

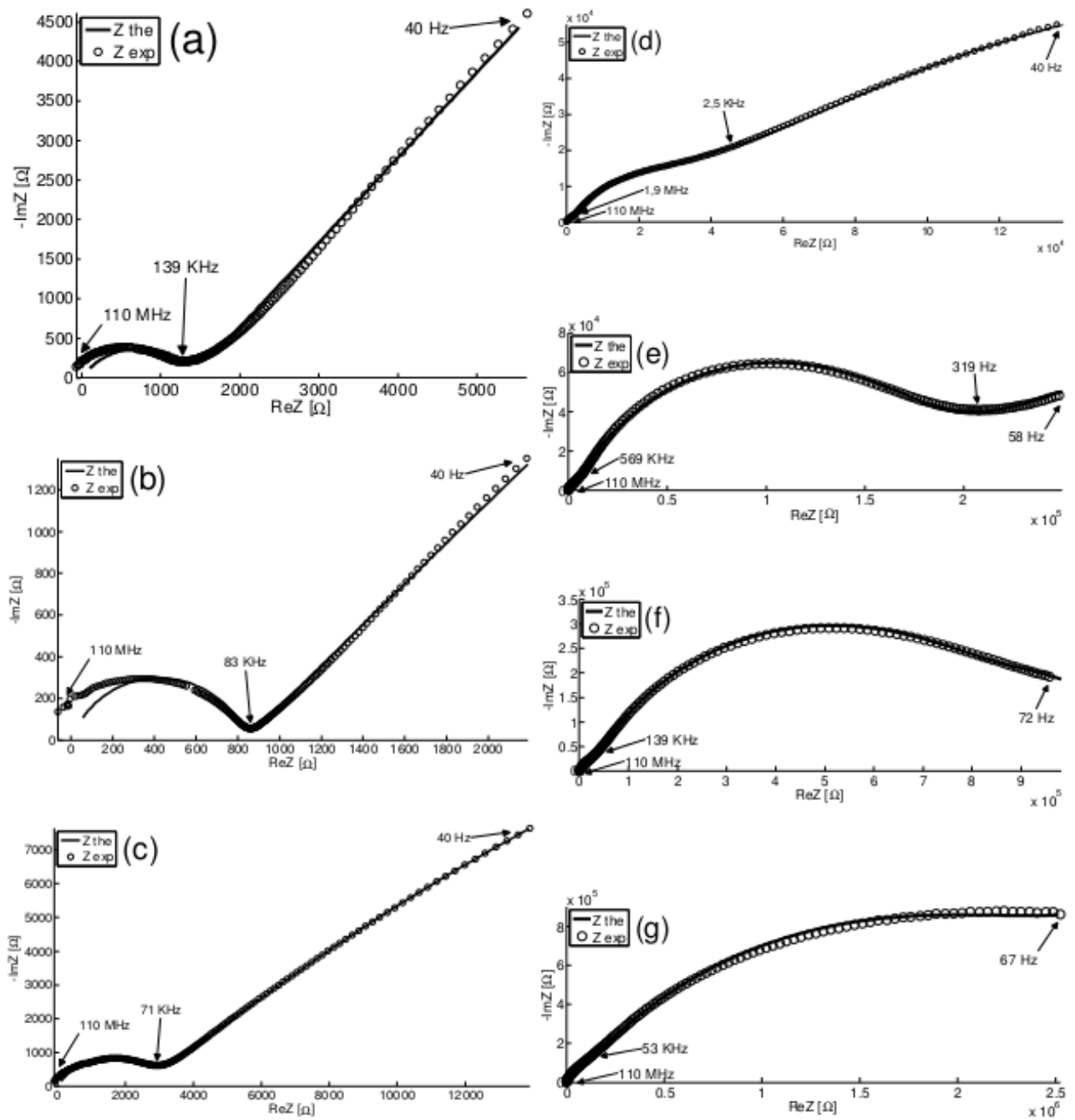


**Figure 5:** Experimental and modeled Nyquist plots for the different water saturation levels of type I cement paste; (a)  $S_l = 0.973$ , (b)  $S_l = 0.966$ , (c)  $S_l = 0.88$ , (d)  $S_l = 0.67$ , (e)  $S_l = 0.50$ , (f)  $S_l = 0.30$ , (g)  $S_l = 0.18$ .

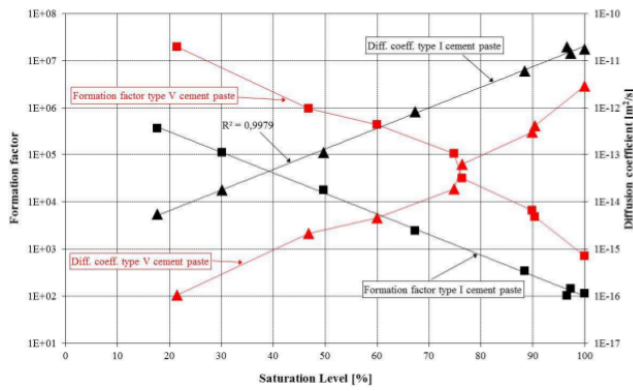


**Figure 6:** Formation factor and chloride diffusion coefficient as a function of the water saturation level.

to be found in the pore size distribution of such materials. Type V cement pastes possess typically the same total pore volume as type I (see Table 1). Yet, their pore size is much smaller as mercury intrusion porosimetry tests can demonstrate [24] and this make them more sensitive to dryness.

## 5 Concluding remarks

The objective of this work was to review the progress of our group on the impact of the pore solution on diffusion through saturated and non-saturated materials. The method chosen to characterize diffusion is based on the electrical analogy between current transport and diffusive transport, and uses Electrochemical Impedance Spectroscopy.

The electrical equivalent model based on the material microstructure proved to be robust over the entire range of water saturation levels, capturing the main features of the material microstructure.

**Acknowledgement:** This work was supported by a contract from ANDRA (Agence Nationale pour la Gestion des Déchets Radioactifs).

## Nomenclature

$A$	Sample cross section [ $\text{m}^2$ ]
$D_{bulk}$	Diffusion coefficient in an infinitely diluted solution, [ $\text{m}^2 \cdot \text{s}^{-1}$ ]
$F$	Faraday constant, [ $\text{C} \cdot \text{mol}^{-1}$ ]
$F_f$	Formation factor, [-]

$L$	Sample thickness, [m]
$Q$	Equivalent capacitance of a constant phase element, [F]
$R$	Ideal gas constant, [ $\text{J} \cdot \text{mol}^{-1} \cdot \text{K}^{-1}$ ]
$R$	Electrical resistance, [ $\Omega$ ]
$S_l$	Saturation level, [-]
$T$	Temperature, [K]
$Z(\omega)$	Impedance [ $\Omega$ ]
$z$	Valency of an ionic species, [-]

## Greek letters

$\alpha$	Phase constant of a $Q$ element, [-]
$\mu$	Electrochemical mobility of an ionic species, [ $\text{m}^2 \cdot \text{s}^{-1} \cdot \text{V}^{-1}$ ]
$\sigma$	Electrical conductivity, [ $\text{S} \cdot \text{m}^{-1}$ ]
$\omega$	Angular frequency, [ $\text{rad} \cdot \text{s}^{-1}$ ]

## References

- [1] Marchand J., Modelling the behaviour of unsaturated cement based systems exposed to aggressive chemical environments, *Mater. Struct.*, 2001, 34, 195–200.
- [2] Bégué P., Lorente S., Migration versus diffusion through porous media: time-dependent scale analysis, *J. Porous Media*, 2006, 9, 637–650.
- [3] Voinitchi D., Julien S., Lorente S., The relation between electrokinetics and chloride transport through cement-based materials, *Cem. Concr. Compos.*, 2008, 30, 157–166.
- [4] Tang L.P., Nilsson L.O., Rapid determination of the chloride diffusivity in concrete by applying an electrical field, *ACI Mater. J.*, 1992, 89, 49–53.
- [5] Khitab A., Lorente S., Ollivier J.P., Predictive model for chloride penetration through concrete, *Mag. Concr. Res.*, 2005, 57(9), 511–520.
- [6] Shi M., Chen Z., Sun J., Determination of chloride diffusivity in concrete by AC impedance spectroscopy, *Cem. Concr. Res.*, 1999, 29, 1111–1115.
- [7] Sanchez I., Lopez M.P., Ortega J.M., Climent M.A., Impedance spectroscopy: an efficient tool to determine the non-steady-state chloride diffusion coefficient in building materials, *Mater. Corros.*, 2011, 62, 139–145.
- [8] Cabeza M., Keddad M., Novoa X.R., Sanchez I., Takenouti H., Impedance spectroscopy to characterize the pore structure during the hardening process of Portland cement paste, *Electrochim. Acta*, 2006, 51, 1831–1841.
- [9] Diaz B., N6voa X.R., P6rez M.C., Study of the chloride diffusion in mortar: a new method of determining diffusion coefficients based on impedance measurements, *Cem. Concr. Compos.*, 2006, 28, 237–245.
- [10] Vedalakshmi R., Renugha Devi R., Bosco E., Palaniswamy N., Determination of diffusion coefficient of chloride in concrete: an electrochemical impedance spectroscopic approach, *Mater.*

- Struct., 2008, 41, 1315–1326.
- [11] Loche J.M., Ammar A., Dumargue P., Influence of the migration of chloride ions on the electrochemical impedance spectroscopy of mortar paste, *Cem. Concr. Res.*, 2005, 35, 1797–1803.
- [12] Arliguie G., Hornain H., *GranDuBé: Grandeurs associées à la Durabilité des Bétons*, Presses de l'école nationale des Ponts et Chaussées, Paris, 2007.
- [13] Atkins P. W., *Physical chemistry*, 6th edition, Oxford university press, Oxford, Melbourne, Tokyo, 1998.
- [14] Snyder K.A., Ferraris C., Martyrs N.S., Garboczi E.J., Using impedance spectroscopy to assess the viability of the rapid chloride test for determining concrete conductivity, *J. Res. NIST*, 2000, 105, 497–509.
- [15] Snyder K.A., The relationship between the formation factor and the diffusion coefficient of porous materials saturated with concentrated electrolytes: theoretical and experimental considerations, *Concr. Sci. Eng.*, 2001, 3, 216–224.
- [16] Barsoukov E., Macdonald J.R., *Impedance spectroscopy*, 2nd edition, John Wiley & Sons, Inc., Hoboken, 2005.
- [17] Orazem M.E., Tribollet B., *Electrochemical impedance spectroscopy*, John Wiley & Sons, Inc., Hoboken, 2008.
- [18] Nelder J., Mead R., A simplex method for function minimization, *Comput. J.*, 1965, 7, 308–313.
- [19] Olsson D., Nelson L., The Nelder-Mead simplex procedure for function minimization, *Technometrics*, 1975, 17, 45–51.
- [20] Cabeza M., Merino P., Miranda A., Nóvoa X.R., Sánchez I., Impedance spectroscopy study of hardened Portland cement paste, *Cem. Concr. Res.*, 2002, 32, 881–91.
- [21] Lorente S., Constructal view of electrokinetic transfer through porous media, *J. Phys. D.: Appl. Phys.*, 2007, 40(9), 2941–2947.
- [22] Nield D.A., Bejan A., *Convection in Porous Media*, 3rd edition, Springer, New York, 2006.
- [23] Bejan A., Dincer I., Lorente S., Miguel A.F., Reis A.H., *Porous and Complex Flow Structures in Modern Technologies*, Springer, New York, 2004.
- [24] Mercado H., Lorente S., Bourbon X., Chloride diffusion coefficients: a comparison between impedance spectroscopy and electrokinetic tests, *Cem. Concr. Compos.*, 2012, 34, 68–75.

## Research Article

## Open Access

Mateus das Neves Gomes, Elizaldo Domingues dos Santos, Liércio André Isoldi, and Luiz Alberto Oliveira Rocha\*

# Numerical Analysis including Pressure Drop in Oscillating Water Column Device

**Abstract:** The wave energy conversion into electricity has been increasingly studied in the last years. There are several proposed converters. Among them, the oscillating water column (OWC) device has been widespread evaluated in literature. In this context, the main goal of this work was to perform a comparison between two kinds of physical constraints in the chimney of the OWC device, aiming to represent numerically the pressure drop imposed by the turbine on the air flow inside the OWC. To do so, the conservation equations of mass, momentum and one equation for the transport of volumetric fraction were solved with the finite volume method (FVM). To tackle the water-air interaction, the multiphase model volume of fluid (VOF) was used. Initially, an asymmetric constraint inserted in chimney duct was reproduced and investigated. Subsequently, a second strategy was proposed, where a symmetric physical constraint with an elliptical shape was analyzed. It was thus possible to establish a strategy to reproduce the pressure drop in OWC devices caused by the presence of the turbine, as well as to generate its characteristic curve.

**Keywords:** Oscillating Water Column (OWC), Numerical Modeling, Volume of Fluid (VOF), Pressure Drop, Turbine

DOI 10.1515/eng-2015-0019

Received January 16, 2015; accepted February 02, 2015

**Mateus das Neves Gomes:** Paraná Federal Institute of Education, Science and Technology, Paranaguá Campus, Rua Antônio Carlos Rodrigues 453, Porto Seguro, Paranaguá, PR, Brazil

**Elizaldo Domingues dos Santos, Liércio André Isoldi:** School of Engineering, Universidade Federal do Rio Grande, Cx.P. 474, Rio Grande, RS 96201-900, Brazil

**\*Corresponding Author: Luiz Alberto Oliveira Rocha:** Department of Mechanical Engineering, Federal University of Rio Grande do Sul, Rua Sarmento Leite, 425, Porto Alegre, RS 90050-170, Brazil, E-mail: luizrocha@mecanica.ufrgs.br

 © 2015 Mateus das Neves Gomes et al., licensee De Gruyter Open. This work is licensed under the Creative Commons Attribution-NonCommercial-NoDerivs 3.0 License.

## 1 Introduction

Nowadays, the investments in exploration of new energy sources are growing, especially in those called renewable energy sources. Renewables are mainly focused on the utilization of solar, wind, biomass and geothermal sources. The diversification of sources should be a target to reach in order to expand and vary the choice [1]. This kind of energy can help to comply with the energetic demand of the world, which had a global energy consumption in 2011 of nearly  $1.6 \times 10^7$  MW, 60% higher than that consumed in 1980 [2]. So far, the main source of energy to reach this demand has been based on the consumption of fossil fuels. Among several ways to obtain energy from renewable sources, the conversion of the ocean wave energy into electrical power can be an attractive alternative for countries with large coastal regions, such as Brazil.

Ocean energy sources can have different classifications. Undoubtedly, the most relevant are the ocean tidal energy (caused by interaction between the gravitational fields of Sun and Moon), the ocean thermal energy (direct consequence of solar radiation incidence), the ocean currents energy (originated from the gradients of temperature and salinity and tidal action) and, finally, the ocean wave energy (which results from the wind effect over the ocean surface) [3].

The criterion used to classify Wave Energy Converters (WEC), in most references, is associated with the installation depth of the device. In this context, the WECs are classified as: Onshore devices (with access by foot), Nearshore devices (with water depths between 8 and 20 m), and Offshore devices (with water depths higher than 20 m). Other possible classification is related to the main operational principle of the wave energy converters. The main operational physical principles mainly described in literature are: Oscillating Water Column (OWC) devices, Floating Bodies (or surging) devices and Overtopping devices [4]. In the present work, the main operational physical principle of OWC converter is numerically studied. The purpose here is to consider, in the computational model, a physical constraint in the chimney outlet mimicking the effect of

the turbine over the fluid flow inside the OWC device, and its interactions with wave flow. This work will allow future investigations about the turbine influence on the design of an OWC chamber. An analogous approach was already employed by Liu et al. [5]. Moreover, this study has the aim to investigate the employment of two different physical restrictions in the outlet chimney of the OWC chamber. More precisely, the influence of blunt body and elliptical shape restrictions on the available power take off (PTO) is evaluated, in addition to determination of the mass flow rate and pressure drop in the OWC device.

Different dimensions for each kind of physical constraint are tested with the purpose to evaluate the effect of restriction geometry on the ratio between the air mass flow rate crossing the chimney and the internal pressure of the OWC hydropneumatic chamber. For this analysis, the geometrical characteristics of the OWC converter were kept fixed, while the diameter of the physical constraint ( $d_1$ ) was varied. Hence, it was possible to choose an optimal  $d_1$  value for each kind of constraint. Subsequently, these optimal values were used to study the incidence of a wave spectrum in real scale in the OWC converter, allowing the numerical reproduction of a turbine characteristic curve. In this sense, a strategy to reproduce the pressure drop in OWC devices caused by the presence of the turbine and the generation of the turbine characteristic curve was established.

The computational domains, composed by an OWC inserted into a wave tank, are generated in GAMBIT software. The numerical simulations are performed in FLUENT software, which is a Computational Fluid Dynamic (CFD) package based on the Finite Volume Method (FVM). More details about the FVM can be found in Versteeg and Malalasekera [6]. The Volume of Fluid (VOF) multi-phase model was adopted to treat adequately the water-air interaction. The VOF model was developed by Hirt and Nichols [7] and it is already used in other numerical studies related with wave energy (e.g. [8–12]). Furthermore, regular waves are generated in the wave tank, reaching to the OWC converter and generating an alternate air flow through its chimney.

## 2 Oscillating Water Column (OWC)

The Oscillating Water Column devices are, basically, hollow structures partially submerged, with an opening to the sea below the water free surface, as can be seen in Figure 1. In accordance with Falcão [4], the electricity generation process has two stages: when the wave reaches

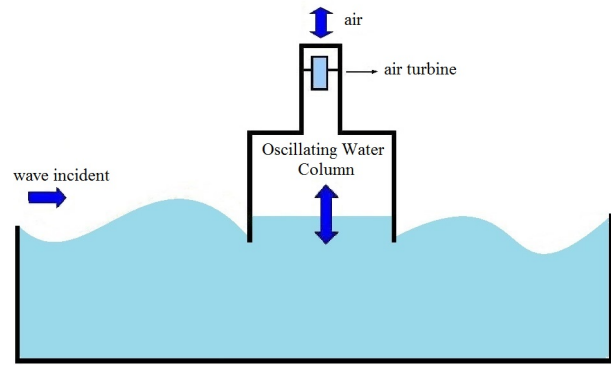


Figure 1: Oscillating Water Column (OWC) converter.

the structure, the column's internal air is forced to pass through a turbine, as a direct consequence of the augmentation of pressure inside the chamber. When the wave returns to the ocean, the air again passes by the turbine, but now being aspirated from the external atmosphere towards the device chamber, due to the chamber internal pressure decreasing. As a consequence, to enable use of these opposite air movements, the Wells turbine is usually employed, which has the property of maintaining the rotation direction irrespective of the flow direction. The turbine/generator set is responsible for the electrical energy production.

## 3 Computational domain

As aforementioned, the computational domain consists of the OWC converter inserted into a wave tank. In addition, to represent the pressure drop imposed to the airflow at the OWC, two physical constraints were considered at the chimney device.

Based on the period ( $T$ ), height ( $H$ ) and propagation depth ( $h$ ) of the wave, it is possible to define the length ( $L_T$ ) and height ( $H_T$ ) of the wave tank (Figure 2). There is no general rule to establish these dimensions, however some aspects must be taken into account. The wave propagation depth is adopted as the wave tank mean water level, i.e., the wave tank water depth ( $h$ ). For the wave tank length it is necessary to consider the wave length, as it is recommended that the wave tank length is at least five times the wave length. In this way, a numerical simulation without effects of wave reflection can be performed, during a satisfactory time interval and without an unnecessarily large increase of the computational domain length (which would cause an increase in the computational effort and in the process-

ing time). Regarding the wave tank height, the propagation depth and the height of the wave must be considered. It is suggested to define the wave tank height as equal to the propagation depth plus three times the wave height.

In the first strategy to represent the pressure drop, called constraint A, a blunt body is placed at the OWC chimney, as shown in Figure 3(a). For this case it is expected that a greater influence of the restriction occurs during the air compression, given its geometry is not symmetrical. The geometry employed here is similar to restriction imposed in the previous work of Conde and Gato [13].

The other physical restriction, called constraint B, proposed in this work, has an elliptical geometry, as can be seen in Figure 3(b). Due to its symmetry, the same airflow resistance is caused during compression and decompression stages; this behavior is more realistic when compared with the influence of the Wells turbine.

Some dimensions for the physical constraints were tested, aiming to evaluate the ratio between the air mass flow rate and the pressure inside the OWC hydropneumatic chamber. In this analysis, the geometric characteristics of the OWC device were kept constant, being variable only the diameter ( $d_1$ ) of the physical constraint. To do so, the optimal geometry obtained by Gomes et al. [14] was adopted, having the follow dimensions:  $H_3 = 9.50$  m;  $H_1/L = 0.1346$ ;  $L = 16.7097$  m;  $H_1 = 2.2501$  m,  $l = 2.3176$  m e  $H_2 = 6.9529$  m; in addition, a real scale wave (period  $T = 5.0$  s, height  $H = 1.00$  m, length  $\lambda = 37.50$  m, and depth  $h = 10.00$  m) was generated.

For the constraint A the dimension  $d_1$  represents its diameter, while the dimension  $d$  represents its length (see Figure 3(a)). Analogously, for the constraint B, the dimension  $d_1$  is the ellipse axis length in the horizontal direction, while the dimension  $d$  defines the ellipse axis length in the vertical direction (see Figure 3(b)).

### 3.1 Boundary Conditions and Mesh

As can be observed in Figure 2, the wave maker is placed in the left side of the wave tank. For the regular wave generation the so-called Function Methodology [15] was employed. This methodology consists of applying the horizontal ( $u$ ) and vertical ( $w$ ) components of wave velocity as boundary conditions (velocity inlet) of the computational model, by means of an User Defined Function (UDF) in the FLUENT® software. These velocity components vary as functions of space and time and are based on the Linear Theory of waves. So these wave velocity components

are given by:

$$u = \frac{H}{2} g k \frac{\cosh(kz + kh)}{\omega \cosh(kh)} \cos(kx - \omega t) \quad (1)$$

$$w = \frac{H}{2} g k \frac{\sinh(kx + kh)}{\omega \cosh(kh)} \sin(kx - \omega t) \quad (2)$$

where:  $H$  is the wave height (m);  $g$  is the gravitational acceleration ( $\text{m/s}^2$ );  $\lambda$  is the wave length (m);  $k$  is the wave number, given by  $k = 2\pi/\lambda(m - 1)$ ;  $h$  is the depth (m);  $T$  is the wave period (s);  $\omega$  is the frequency, given by  $\omega = 2\pi/T$  (rad/s);  $x$  is the streamwise coordinate (m);  $t$  is the time (s); and  $z$  is the normal coordinate (m).

Concerning the other boundary conditions, in the upper surfaces of wave tank and chimney and above the wave maker (dashed line in Figure 2) the atmospheric pressure was considered (pressure outlet). In the bottom and right side of computational domain the no slip and impermeability conditions (wall) were adopted.

## 4 Mathematical model

The analysis consists in finding the solution of a water-air mixture flow. For this, the conservation equations of mass, momentum and one equation for the transport of volumetric fraction are solved via the finite volume method (FVM). The conservation equation of mass for an isothermal, laminar and incompressible flow with two phases (air and water) is the following:

$$\frac{\partial \rho}{\partial t} + \nabla \cdot (\rho \vec{v}) = 0 \quad (3)$$

where  $\rho$  is the mixture density [ $\text{kg/m}^3$ ] and  $\vec{v}$  is the velocity vector of the flow [ $\text{m/s}$ ].

The conservation equation of momentum is:

$$\frac{\partial}{\partial t} (\rho \vec{v}) + \nabla \cdot (\rho \vec{v} \vec{v}) = -\nabla p + \nabla \cdot (\bar{\tau}) + \rho \vec{g} + \vec{F} \quad (4)$$

where:  $p$  is the pressure ( $\text{N/m}^2$ ),  $\rho \vec{g}$  and  $\vec{F}$  are buoyancy and external body forces ( $\text{N/m}^3$ ), respectively, and  $\bar{\tau}$  is the deformation rate tensor ( $\text{N/m}^2$ ), which, for a Newtonian fluid, is given by:

$$\bar{\tau} = \mu \left[ \left( \nabla \vec{v} + \nabla \vec{v}^T \right) - \frac{2}{3} \nabla \cdot \vec{v} I \right] \quad (5)$$

where  $\mu$  is the dynamic viscosity ( $\text{kg/(ms)}$ ), and  $I$  is a unitary tensor; the second right-hand-side term is concerned with the deviatoric tension ( $\text{N/m}^2$ ).

In order to deal with the air and water mixture flow and to evaluate its interaction with the device, the Volume of

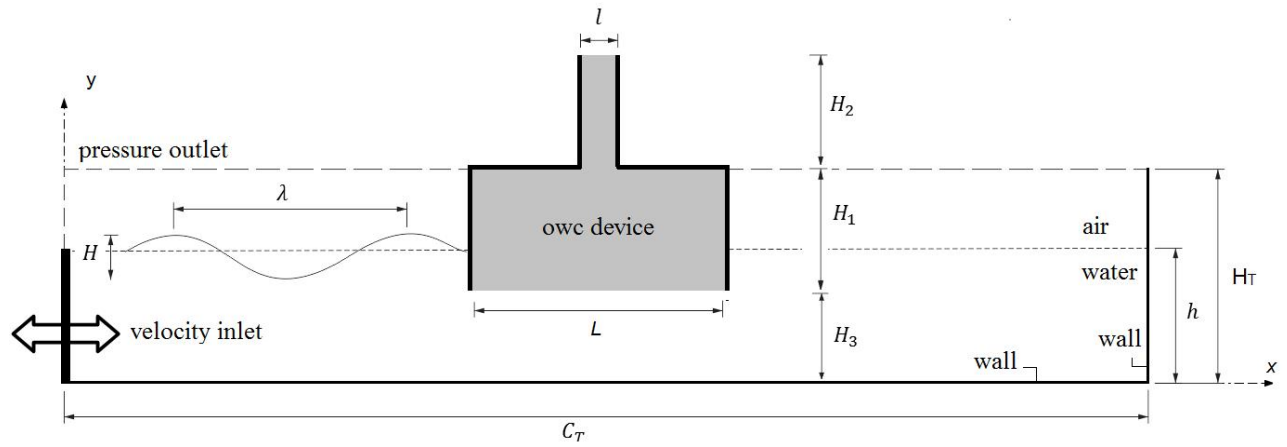


Figure 2: Schematic representation of the computational domain.

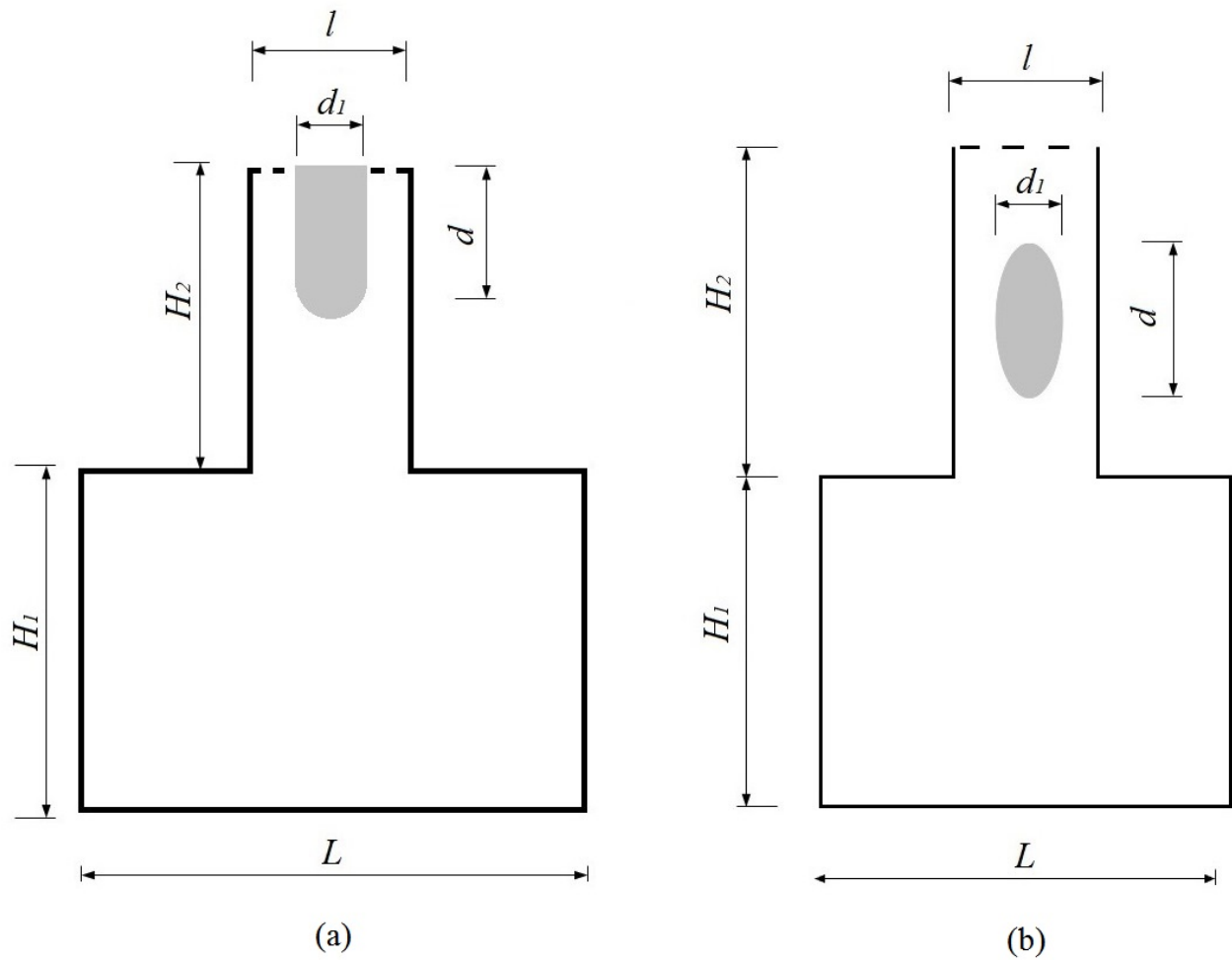


Figure 3: Physical constraints at the OWC chimney: (a) blunt body (constraint A); (b) elliptical body (constraint B).

Fluid (VOF) method is employed. The VOF is a multiphase model used for fluid flows with two or more phases. In this model, the phases are immiscible, i.e., the volume of one phase cannot be occupied by another phase [16, 17].

In the simulations of this study, two different phases are considered: air and water. Therefore, the volume fraction concept ( $\alpha_q$ ) is used to represent both phases inside one control volume. In this model, the volume fractions are assumed to be continuous in space and time and the sum of volume fractions, inside a control volume, is always unitary ( $0 \leq \alpha_q \leq 1$ ). Consequently, if  $\alpha_{water} = 0$ , the cell is empty of water and full of air ( $\alpha_{air} = 1$ ), and if the fluid has a mixture of air and water, one phase is the complement of the other, i.e.,  $\alpha_{air} = 1 - \alpha_{water}$ . Thus, an additional transport equation for one of the volume fractions is required:

$$\frac{\partial(\rho\alpha_q)}{\partial t} + \nabla \cdot (\rho\alpha_q\vec{v}) = 0 \quad (6)$$

It is worth mentioning that the conservation equations of mass and momentum are solved for the mixture. Therefore, it is necessary to obtain values of density and viscosity for the mixture, which can be written by:

$$\rho = \alpha_{water}\rho_{water} + \alpha_{air}\rho_{air} \quad (7)$$

$$\mu = \alpha_{water}\mu_{water} + \alpha_{air}\mu_{air} \quad (8)$$

## 5 Numerical model

For the numerical simulation of the conservation equations of mass and momentum, a commercial code based on the FVM is employed [18]. The solver is pressure-based and all simulations were performed using ‘upwind’ and PRESTO for spatial discretizations of momentum and pressure, respectively. The velocity-pressure coupling is performed by the PISO method, while the GEO-RECONSTRUCTION method is employed to tackle with the volumetric fraction. Moreover, under-relaxation factors of 0.3 and 0.7 are imposed for the conservation equations of continuity and momentum, respectively. More details concerning the numerical methodology can be obtained in the works of Versteeg and Malalasekera [6] and Patankar [19]. The numerical simulations were performed using a computer with two dual-core Intel processors with 2.67 GHz clock and 8 GB ram memory. It used Message Passing Interface (MPI) for parallelization. The processing time of each simulation was approximately two hours.

It is important to emphasize that this numerical methodology was already validated in previous studies of this re-

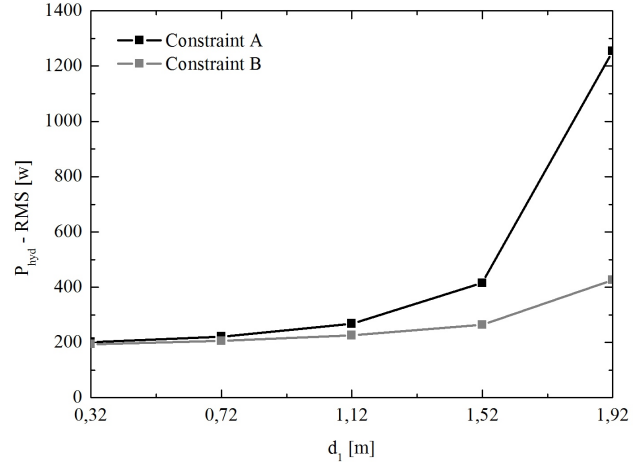


**Figure 4:** The effect of diameter ( $d_1$ ) over the RMS available hydropneumatic power for the two different studied constraints.

search group [14, 15]. Therefore, for the sake of brevity, this validation will not be repeated in this study.

## 6 Results and Discussions

Five values for the dimension  $d_1$  were tested (Table 1), for both constraints (A and B). For the constraint A, the value of  $d$  was also changed, being considered  $d = 1$  m plus the constraint radius ( $d_1/2$ ) for each case. For the constraint B the value of  $d$  is constant, as noted in Table 1.

Figure 4 shows the effect of physical constraint diameter ( $d_1$ ) over the root mean square (RMS) hydropneumatic power ( $P_{hyd}$ ) for constraints A and B. For constraint A it can be noticed that the increase of  $d_1$  leads to an increase of  $P_{hyd-RMS}$  in the device, especially for  $d_1 \geq 1.1176$  where the magnitude of  $P_{hyd}$  had a step increase. For constraint B, results showed an increase of  $P_{hyd}$  with the increase of the diameter of the restriction ( $d_1$ ). However, the increase of  $P_{hyd}$  for constraint B is smoothed in comparison with those reached for constraint A, especially in the range  $1.1176 \leq d_1 \leq 1.9176$ , where the highest magnitudes of  $P_{hyd}$  are achieved for both constraints. In other words, results showed that the employment of different geometries for each constraint also led to differences in available power in the OWC device.

With the purpose to improve the comprehension about the effect of  $d_1$  over the available power of the device, the transient mass flow rate for constraints A and B (Figure 5(a) and Figure 5(b)), as well as transient pressure inside the chamber for the same constraints (Figure 6(a) and Figure 6(b)) are shown.

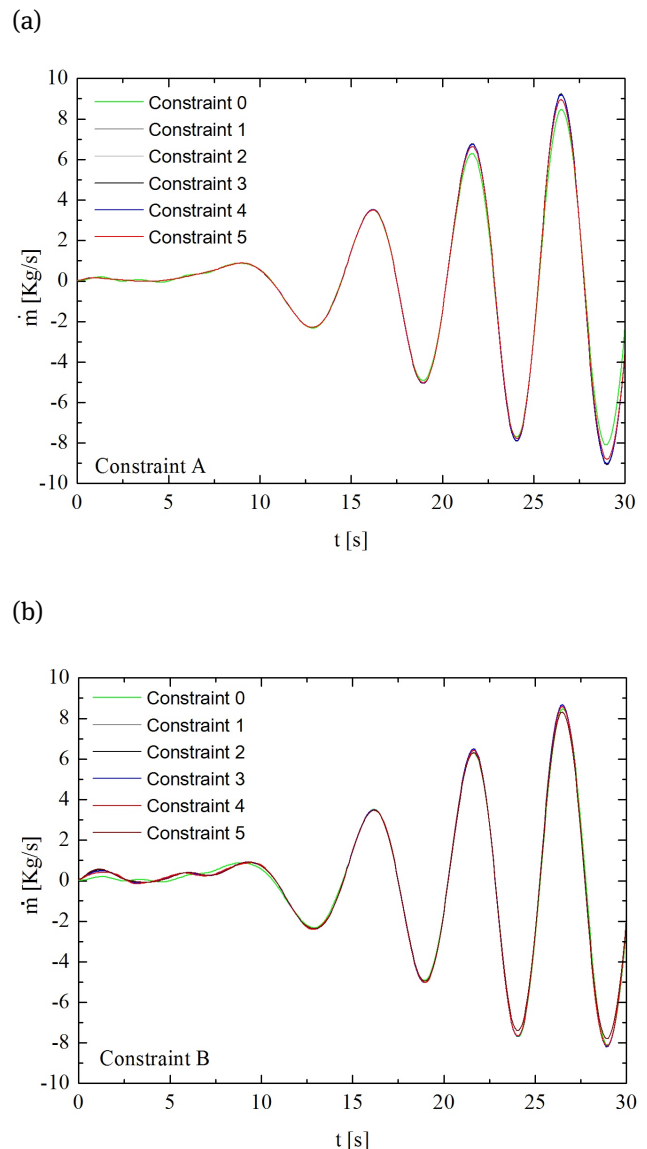
**Table 1:** Physical constraint dimensions.

Case	Constraint A			Constraint B		
	$d_1$ [m]	$d$ [m]	Area [m <sup>2</sup> ]	$d_1$ [m]	$d$ [m]	Area [m <sup>2</sup> ]
0	0.0000	0.0000	0.0000	0.0000	0.0000	0.0000
1	0.3176	1.1588	0.3968	0.3176	2.0000	0.4988
2	0.7176	1.3588	1.1220	0.7176	2.0000	1.1272
3	1.1176	1.5588	2.0985	1.1176	2.0000	1.7555
4	1.5176	1.7588	3.3264	1.5176	2.0000	2.3838
5	1.9176	1.9588	4.8056	1.9176	2.0000	3.0121

For constraint A, a decrease of mass flow rate for every instants of time with the augmentation of geometrical constraint can be seen (Figure 5(a)). This effect is more evident for constraint case 5, where a reduction of nearly 30% is noticed for the mass flow rate. Concerning the pressure inside the chamber, Figure 6(a) shows a strong increase of pressure inside the chamber with the augmentation of the restriction. For instance, for  $t = 27.0$  s, the pressure increases four times from restriction case 4 to restriction case 5. In this sense, the increase of pressure gradient from the chamber to the chimney outlet for the case with the largest restriction compensates the decrease of mass flow rate. It is worthy to mention that a minimal momentum for the air flow is required to drive the turbine. As a consequence, the imposition of a turbine with large turbine hub diameter ( $d_1$ ) can be inviable in practical applications.

For constraint B, results of mass flow rate (Figure 5(b)) show that the elliptical restriction leads to similar magnitudes for all values of  $d_1$  investigated, with slight differences in peaks and values of mass flow rate. Concerning the pressure inside the chamber, for constraint B (Figure 6(b)) the magnitude of pressures are similar in the inlet and outlet of the air flow in the device, which is not noticed for constraint A. This difference can be assigned to differences in the geometrical shape of constraints A and B. In constraint A the geometry is asymmetric and inserted in the chimney outlet, while constraint B is symmetric and inserted in the center of chimney leading to a more symmetrical behavior of pressure inside the chamber.

In general, the results of power as a function of diameter  $d_1$  show the importance of geometrical evaluation of turbine inserted in the OWC chimney. For constraint A, the highest diameter  $d_1$  evaluated leads to an available power six times higher than that achieved with the lowest diameter  $d_1$  studied. For both cases (constraints A and B) the highest value of  $d_1$  leads to the highest available power in the device. However, for constraint A and  $d_1 > 1.5176$  m the mass flow rate suffers a strong decrease. Moreover, the

**Figure 5:** Transient behavior of mass flow rate for all studied diameters (cases 0 to 5, see Table 1) for: (a) constraint A; (b) constraint B.

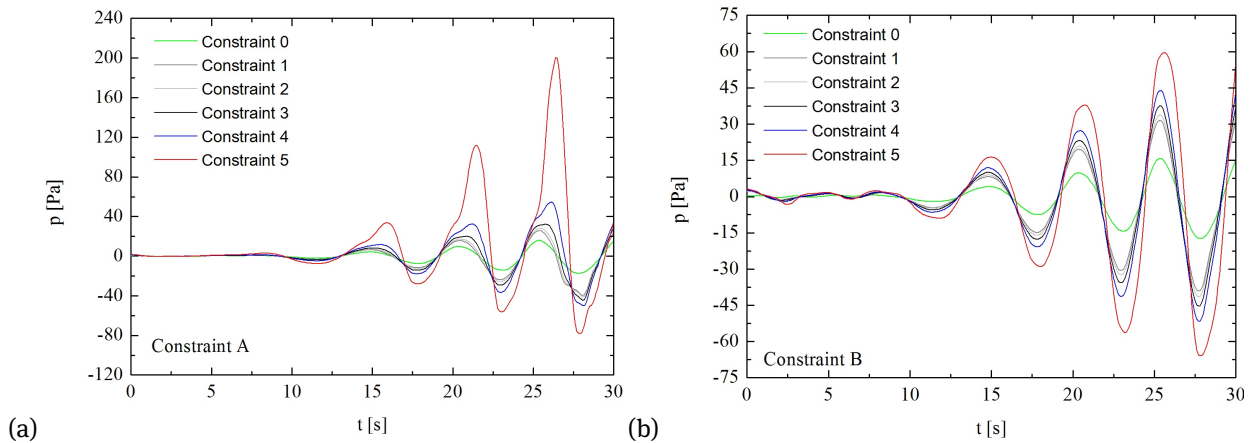


**Figure 6:** Transient behavior of pressure inside the chamber for all studied diameters (cases 0 to 5, see Table 1) for: (a) Constraint A; (b) Constraint B.

pressure inside the chamber increases dramatically, being necessary to decrease the pressure inside the chamber by means of a by-pass valve in the OWC chamber.

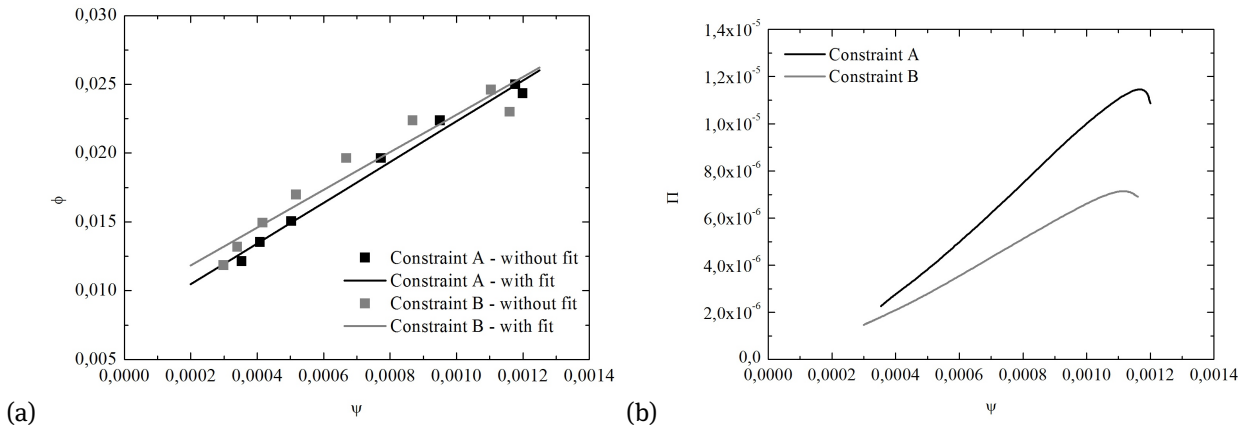
Weber and Thomas [20] presented three dimensionless coefficients for the mass flow rate (flow coefficient), for the pressure drop (pressure coefficient) and for the available power (power coefficient). The effect of pressure coefficient ( $\psi$ ) over the flow coefficient ( $\phi$ ) and power coefficient ( $\Pi$ ) has been described in literature, mainly into the experimental framework [20].

Figure 7(a) shows the effect of pressure coefficient over the flow coefficient, and Figure 7(b) depicts the effect of pressure coefficient over the power coefficient. As aforementioned, these curves are constructed by means of simulation of a wave spectrum for a pre-determined restriction ( $d_1 = 1.5176$  m, which represents a condition where the fluid flow inside the chamber does not suffer a strong reduction of mass flow rate nor a strong increase of pressure inside the chamber). The results showed an almost linear relation between the pressure coefficient and flow coefficient, which represents adequately the characteristic curve of a Wells turbine. For power coefficient, the behavior is also almost linear, except in regions of highest pressure where the power begins to decrease. In general, the behavior predicted numerically is similar to those obtained experimentally in existing literature [20]. In this sense, the employment of a restriction mimicking the effect of a turbine over the fluid flow seems an adequate methodology to construct the characteristic turbine curve for an OWC device.

## 7 Concluding remarks

In the present work, a numerical study was performed with the purpose of comparing the imposition of two different physical restrictions at the chimney outlet, mimicking the effect of a turbine over the fluid flow inside an OWC chamber device. The first strategy considered a bluff body in the chimney outlet (constraint A) and the second approach imposed an elliptical obstacle (constraint B) in the half of chimney duct. The effect of geometry on the available power take off in the device is evaluated. Subsequently, the best geometries were submitted to wave flows under different conditions in order to generate a turbine characteristic curve. The conservation equations of mass, momentum and the volumetric fraction were solved with the employment of a CFD package based on the Finite Volume Method. To treat the interaction between the water-air mixture, the Volume of Fluid (VOF) method was used.

Results showed that the type of restriction affected the available power as well as the transient behavior of the air flow inside the chamber. On the one hand, constraint B (elliptic form) led to similar magnitudes of mass flow rate and pressure drop in the exhaustion and suction of the air into the chamber. On the other hand, for constraint A (bluff body), the pressure inside the chamber behaved in an asymmetric way, with higher pressure drop magnitudes in the exhaustion than in the suction of the air through the chimney. It was also noticed that two main factors must be taken into account to represent adequately the turbine by means of an imposed restriction: the pressure inside the chamber and the mass flow rate. The combination of these two parameters generated the available power in the device.



**Figure 7:** Wells characteristic curves represented by constraints A and B: (a) flow coefficient ( $\phi$ ) as a function of pressure coefficient ( $\psi$ ); b) power coefficient ( $\Pi$ ) as a function of pressure coefficient.

The effect of restriction geometry, more precisely the parameter  $d_1$ , on the available power in the OWC device was also evaluated. The parameter  $d_1$  had a strong influence on the available power in the OWC chimney. For constraint A, for example, the largest diameter  $d_1$  evaluated led to an available power six times greater than that achieved with the lowest diameter  $d_1$  studied. Results allowed the determination of a theoretical recommendation for the parameter  $d_1$ , which must be increased until a superior limit is reached, where the momentum is enough to drive the turbine, and where the pressure inside the chamber is not large enough to suppress the water movement inside the chamber.

Lastly, the optimal value of  $d_1$  that maximizes the available power and at the same time does not cause a strong reduction in the mass flow rate and excessive pressure inside the chamber was used to study the incidence of a wave spectrum in real scale in the OWC converter, allowing the construction of a turbine characteristic curve. In this sense, it was possible to establish a strategy to reproduce the pressure drop in OWC devices caused by the presence of the turbine and to generate its characteristic curve, as well as estimate the available power in the device. The behavior found numerically here was similar to those obtained experimentally in literature [20]. Future studies will use this methodology for geometric optimization of device chamber.

**Acknowledgement:** The authors thank the Universidade Federal de Rio Grande (FURG), Universidade Federal do Rio Grande do Sul (UFRGS), Instituto Federal do Paraná (IFPR), FAPERGS and CNPq (Process: 555695/2010-7) for financial support. E. D. dos Santos, L. A. Isoldi and L.A.O. Rocha also thank CNPq for a research grant and E. D. dos

Santos thanks FAPERGS for financial support (Process: 12/1418-4).

### Conflict of Interest

The authors do not have a direct financial relation with the commercial identity mentioned in this paper, avoiding any conflict of interest.

## Nomenclature

$d$	Length of constraint [m]
$d_1$	Diameter of the constraint [m]
$\vec{F}$	External body forces [ $\text{N}/\text{m}^3$ ]
$g$	Gravitational acceleration [ $\text{m}/\text{s}^2$ ]
$h$	Propagation depth [m]
$H$	Wave height [m]
$H_1$	Height of the chamber [m]
$H_2$	Height of the chimney [m]
$H_3$	Lip submergence [m]
$H_T$	Height of the wave tank [m]
$I$	Unitary tensor tension [ $\text{N}/\text{m}^2$ ]
$k$	Wave number [ $\text{m}^{-1}$ ]
$l$	Length of the chimney [m]
$L$	Length of the chamber [m]
$L_T$	Length of the wave tank [m]
$p$	Pressure [Pa]
$P_{hyd}$	Hydropneumatic power [W]
$t$	Time [s]
$T$	Wave period [s]
$u$	Horizontal component of the velocity of the wave [m/s]
$v$	Vertical component of the velocity of the wave [m/s]

$\vec{v}$	Velocity vector [m/s]
$x$	Streamwise coordinate [m]
$z$	Normal coordinate [m]

## Greek Letters

$\alpha$	Volume fraction [dimensionless]
$\lambda$	Wave length [m]
$\mu$	Dynamic viscosity [Kg/ms]
$\rho$	Mixture density [Kg/m <sup>3</sup> ]
$\bar{\tau}$	Deformation rate tensor [N/m <sup>2</sup> ]
$\Pi$	Power coefficient [dimensionless]
$\omega$	Frequency [rad/s]
$\phi$	Flow coefficient [dimensionless]
	Pressure coefficient [dimensionless]

## Acronyms

CFD	Computational Fluid Dynamics
FVM	Finite Volume Method
MPI	Message Passing Interface
OWC	Oscillating Water Column
PISO	Pressure-Implicit with Splitting of Operators
PTO	Power Take Off
RMS	Root Mean Square
VOF	Volume Of Fluid
WEC	Wave Energy Converters

## References

- [1] A. F. Miguel, M. Aydin. Ocean exergy and energy conversion systems. *Int. J. of Exergy* 10 (2013) 454-470.
- [2] F. Zabihiyan, A.S. Fung, Review of marine renewable energies: case study of Iran, *Renew. Sust. Energ. Rev.* 15 (2011) 2461-2474.
- [3] R. Pelc, R. M. Fujita, Renewable energy from the ocean. *Marine Policy* 26 (2002) 471-479.
- [4] A. F. de O. Falcão. Wave energy utilization: A review of the technologies. *Renewable and Sustainable Energy Reviews.* 14 (2010) 899-918.
- [5] Z. Liu, B. S. Hyun, K. Hong, Y. Lee, Investigation on integrated system of chamber and turbine for OWC wave energy convertor, *Proceeding of the nineteenth international offshore and polar engineering conference* (2009), 276-282.
- [6] H. K. Versteeg, W. Malalasekera, *An Introduction to Computational Fluid Dynamics – The Finite Volume Method*, Longman, England, 1995.
- [7] C. W. Hirt, B. D. Nichols, Volume of fluid (VOF) method for the dynamics of free boundaries, *Journal of Computational Physics*, 39 (1981), 201-225.
- [8] M. Horko, CFD Optimization of an oscillating water column energy converter, MSc. Thesis, School of Mechanical Engineering, The University of Western, Australia, 2007.
- [9] Z. Liu, B.-S. Hyun, K. Hong, Numerical study of air chamber for oscillating water column wave energy /convertor, *China Ocean Eng.* 25 (2011) 169-178.
- [10] M. das N. Gomes, Computational modeling of an Oscillating Water Column device to conversion of wave energy into electrical energy (in Portuguese), MSc. Thesis, Federal University of Rio Grande, Brazil, 2010.
- [11] E.D. Dos Santos, B.N. Machado, N.R. Lopes, J.A. Souza, P.R.F. Teixeira, M.N. Gomes, L.A. Isoldi, L.A.O. Rocha, Constructal Design of Wave Energy Converters, in: L.A.O. Rocha, S. Lorente, A. Bejan (Eds.), *Constructal Law and the Unifying Principle of Design*, Springer, New York, 2013, pp. 275-294.
- [12] E. D. dos Santos, B. N. Machado, M. M. Zanella, M. das N. Gomes, J. A. Souza, L. A. Isoldi, L. A. O. Rocha, Numerical Study of the Effect of the Relative Depth on the Overtopping Wave Energy Converters According to Constructal Design. *Defect and Diffusion Forum* 348 (2014) 232-244.
- [13] J. M. P. Conde, L. M. C. Gato, Numerical study of the air-flow in na oscillating water column wave energy converter. *Renew. Energy* 33 (2008) 2637 – 2644.
- [14] M. N. Gomes, M, E. D. dos Santos, E, L. A. Isoldi, L. A. O. Rocha, Two-dimensional geometric optimization of an oscillating water column converter of real scale, *Proceedings 22nd International Congress of Mechanical Engineering, COBEM*, (2013), Ribeirão Preto.
- [15] M. das N. Gomes, C.R. Olinto, L.A.O. Rocha, J.A. Souza, L.A. Isoldi, Computational modeling of a regular wave tank. *Therm. Eng.* 8 (2009) 44-50.
- [16] L. Ling, C. Yongcan, L. Yuliang, Volume of fluid (VOF) method for curved free surface water flow in shallow open channel, *Department of Hydraulic Engineering, Tsinghua University, Beijing*, 2001.
- [17] X. Lv, Q. Zou, D. Reeve, Numerical simulation of overflow at vertical weirs using a hybrid level set/VOF method, *Adv. Water Resour.* 34 (2011) 1320-1334.
- [18] FLUENT, version 6.3.16, ANSYS Inc., 2007.
- [19] S.V. Patankar, *Numerical Heat Transfer and Fluid Flow*, McGraw Hill, New York, 1980.
- [20] J. W. Weber, G. P. Thomas, An investigation into the importance of the air chamber design of an oscillating water column wave energy device, *Proceeding of the eleventh international offshore and polar engineering conference* (2001), pp. 581-588.

## Research Article

## Open Access

Abdelkader Boutra, Karim Ragui, Nabila Labsi, and Youb Khaled Benkahla\*

**Lid-Driven and Inclined Square Cavity Filled With a Nanofluid: Optimum Heat Transfer**

DOI 10.1515/eng-2015-0028

Received September 16, 2014; accepted April 07, 2015

**Abstract:** This paper reports a numerical study on mixed convection within a square enclosure, filled with a mixture of water and Cu (or Ag) nanoparticles. It is assumed that the temperature difference driving the convection comes from the side moving walls, when both horizontal walls are kept insulated. In order to solve the general coupled equations, a code based on the finite volume method is used and it has been validated after comparison between the present results and those of the literature. To make clear the effect of the main parameters on fluid flow and heat transfer inside the enclosure, a wide range of the Richardson number, taken from 0.01 to 100, the nanoparticles volume fraction (0% to 10%), and the cavity inclination angle ( $0^\circ$  to  $180^\circ$ ) are investigated. The phenomenon is analyzed through streamlines and isotherm plots, with special attention to the Nusselt number.

**Keywords:** mixed convection, lid-driven cavity; Cu and Ag nanoparticles; water base fluid; finite volume method

$Pr$	Prandtl number, $Pr = C_p \mu_f / k_f$
$Re$	Reynolds number, $Re = \rho_f V_{lid} H / \mu_f$
$Ri$	Richardson number, $Ri = Gr / Re^2$
$T$	Temperature [K]
$u, v$	Velocity components [m/s]
$U, V$	Dimensionless velocity components
$x, y$	Cartesian coordinates [m]
$X, Y$	Dimensionless Cartesian coordinates

**Greek letters**

$\alpha$	Thermal diffusivity [ $\text{m}^2/\text{s}$ ]
$\beta$	Thermal expansion coefficient [ $1/\text{K}$ ]
$\theta$	Dimensionless temperature
$\mu$	Viscosity [ $\text{kg}/\text{ms}$ ]
$\rho_f$	Fluid density [ $\text{kg}/\text{m}^3$ ]
$\phi$	Nanoparticles volume fraction
	Cavity inclination angle

**Nomenclature**

$C_p$	Specific heat, [ $\text{J}/\text{kgK}$ ]
$Gr$	Grashof number, $Gr = g \beta \rho_f^2 \Delta T H^3 / \mu_f^2$
$H$	Cavity height, [m]
$k$	Thermal conductivity, [ $\text{W}/\text{mK}$ ]
$N$	Normal direction to the wall
$Nu$	Nusselt number
$p^*$	Pressure [Pa]
$P$	Dimensionless pressure

**Subscripts**

$c$	Cold
$h$	Hot
$nf$	Nanofluid
$s$	Solid particles

**1 Introduction**

Heat convection of nanofluids, which are a mixture of nanoparticles in a base fluid such water and oil, has been recently an active field of research since they are used to improve heat transfer. Compared to other techniques for enhancing heat transfer in practical applications, nanofluids have the advantage of behaving like pure fluids because of the nanometric size of introducing solid parti-

**Abdelkader Boutra, Karim Ragui, Nabila Labsi:** Laboratory of Transfer Phenomenon, University of Sciences and Technology Houari Boumediene BP. 32 El Alia, 16111 Bab Ezzouar, Algiers, Algeria

**\*Corresponding Author: Youb Khaled Benkahla:** Laboratory of Transfer Phenomenon, University of Sciences and Technology Houari Boumediene BP. 32 El Alia, 16111 Bab Ezzouar, Algiers, Algeria, E-mail: youbenkahla@yahoo.fr

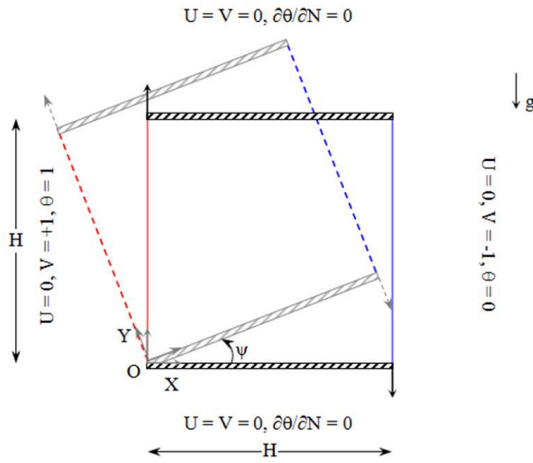


Figure 1: Simulation domain with its boundary conditions.

cles. Thus, they are used as heat transfer fluids for various applications, such as advanced nuclear systems or micro/mini channel heat sinks, electronic equipment as power transistors, printed wiring boards and chip packages mounted on computer mother boards.

To reveal the effects of such added nanoparticles on the heat transfer, some papers deal with natural convection of nanofluids, in differentially heated enclosures, were very helpful [1–3]. The literature indicates that most researches [4–6] were achieved using a closed configuration whilst a little attention has been devoted to the convection phenomenon within a moving wall enclosure [7, 8].

As such, the aim of the present paper is to examine the combined natural-forced convection heat transfer in a square cavity filled with a nanofluid in order to predict the effect of the Richardson number, the nanoparticles volume fraction and the square inclination angle on fluid flow and heat transfer as well.

Referred to papers of Elif [9], Santra *et al.* [10] and many others [11], the nanoparticles with a high thermal conductivity (such as Ag and Cu) produce a great enhancement in heat transfer rate. For this reason, Cu and Ag nanoparticles are considered in the present investigation.

It is to note that this kind of configurations represents an important industrial application such the shear mixture, where we train the fluid on both sides to generate a mixture.

Table 1: Thermo-physical properties of the base fluid and the nanoparticles at  $T = 25^\circ\text{C}$ .

Thermo-physical properties	Fluid Phase (water)	Cu	Ag
$C_p$ (J/kgK)	4179	385	230
$\rho$ (kg/m <sup>3</sup> )	997.1	8933	10500
$k$ (W/mK)	0.613	401	418
$\beta$ (1/K) $10^{-5}$	21	1.67	1.97

## 2 Problem’s statement and Mathematical formulation

The physical model of the problem, along with its boundary condition, is shown in Figure 1. A square inclined cavity filled with (Cu or Ag)-water nanofluid is considered, such as the water and the Cu (or Ag) nanoparticles are in thermal equilibrium. The side moving walls are maintained at a different constant temperatures  $\theta_h$  and  $\theta_c$ , respectively, when the horizontal walls are kept insulated. The flow and heat transfer are steady and two-dimensional. The Richardson number ( $= Gr/Re^2$ ) is taken as 0.01, 1 and 100 to simulate the forced, mixed and natural convection, respectively. The thermo-physical properties of the base fluid and the solid nanoparticles are given in Table 1. Constant thermo-physical properties are considered for the nanofluid, whereas the density variation in the buoyancy forces is determined using the Boussinesq approximation [12].

The density,  $\rho_{nf}$ , the heat capacity,  $(\rho C_p)_{nf}$ , the thermal expansion coefficient,  $(\rho\beta)_{nf}$ , and the thermal diffusivity of the nanofluid,  $\alpha_{nf}$ , are defined, respectively, as follows [13]:

$$\rho_{nf} = (1 - \phi)\rho_f + \phi\rho_s, \tag{1}$$

$$(\rho C_p)_{nf} = (1 - \phi)(\rho C_p)_f + \phi(\rho C_p)_s, \tag{2}$$

$$(\rho\beta)_{nf} = (1 - \phi)(\rho\beta)_f + \phi(\rho\beta)_s, \tag{3}$$

$$\alpha_{nf} = \frac{k_{nf}}{(\rho C_p)_{nf}}. \tag{4}$$

The effective viscosity  $\mu_{nf}$  and the thermal conductivity  $k_{nf}$  of the nanofluid are determined according to Brinkman [14], Equation 5, and Maxwell [15], Equation 6, models:

$$\mu_{nf} = \frac{\mu_f}{(1 - \phi)^{2.5}}, \tag{5}$$

$$\frac{k_{nf}}{k_f} = \frac{(k_s + 2k_f) - 2\phi(k_s + k_f)}{(k_s + 2k_f) + \phi(k_s + k_f)}. \quad (6)$$

The dimensionless continuity, momentum (according to horizontal and vertical directions) and energy equations are given, respectively, as:

$$\frac{\partial U}{\partial X} + \frac{\partial V}{\partial Y} = 0, \quad (7)$$

$$U \frac{\partial U}{\partial X} + V \frac{\partial U}{\partial Y} = -\frac{\partial P}{\partial X} + \frac{1}{Re} \frac{\mu_{nf}}{\rho_{nf} \nu_f} \left[ \frac{\partial^2 U}{\partial X^2} + \frac{\partial^2 U}{\partial Y^2} \right] + Ri \frac{(\rho\beta)_{nf}}{\rho_{nf} \beta_f} \theta \sin \psi, \quad (8)$$

$$U \frac{\partial U}{\partial X} + V \frac{\partial V}{\partial Y} = -\frac{\partial P}{\partial Y} + \frac{1}{Re} \frac{\mu_{nf}}{\rho_{nf} \nu_f} \left[ \frac{\partial^2 V}{\partial X^2} + \frac{\partial^2 V}{\partial Y^2} \right] + Ri \frac{(\rho\beta)_{nf}}{\rho_{nf} \beta_f} \theta \cos \psi, \quad (9)$$

$$U \frac{\partial \phi}{\partial X} + V \frac{\partial \phi}{\partial Y} = \frac{\alpha_{nf}}{\alpha_f} \frac{1}{PrRe} \left[ \frac{\partial^2 \theta}{\partial X^2} + \frac{\partial^2 \theta}{\partial Y^2} \right], \quad (10)$$

where  $Re = \rho_f V_{wall} H / \mu_f$  is the Reynolds number,  $Ri = Gr / Re^2$  the Richardson number and  $Pr = C_p \rho_f / k_f$  is the Prandtl number.

The mean Nusselt number over the hot (or cold) wall is given by the following expression:

$$|Nu|_{wall} = \int_0^1 \left( \frac{k_{nf}}{k_f} \right) \frac{\partial \theta}{\partial X} \Big|_{X=0 \text{ or } 1} dY. \quad (11)$$

The mean Nusselt number inside the cavity is calculated as:

$$Nu = \frac{Nu_h + Nu_c}{2}. \quad (12)$$

### 3 Numerical procedure and validation

The governing equations are discretized in space using the finite volume method. As the momentum equation is formulated in terms of primitive variables ( $U$ ,  $V$  and  $P$ ), the iterative procedure includes a pressure correction calculation method, namely SIMPLER [16], to solve the pressure velocity coupling. In fact, a regular two-dimensional finite difference mesh is generated in the computational domain. Then, a square shaped control volume is generated around each nodal point. The governing equations are

then integrated over each control volume. Subsequently, the derivatives of the dependent variables on the faces of the control volume in the resulting equations are replaced by finite difference forms written in terms of the nodal values of the dependent variables. A second-order central difference scheme is used for the diffusion terms while a hybrid scheme, a combination of upwind and central difference schemes, is employed for the convective terms citeb:16. Carrying out the same procedure for all the control volumes yields a system of algebraic equations with nodal values of the dependent variables as unknowns. The set of discretized equations are then solved iteratively yielding the velocity, pressure, and temperature at the nodal points. An under relaxation scheme is employed to obtain converged solutions.

The adopted convergence criterion for the temperature, the pressure, and the velocity is given as:

$$\frac{\sum_{j=2}^m \sum_{i=1}^n |\phi_{i,j}^{\zeta+1} - \phi_{i,j}^{\zeta}|}{\sum_{j=1}^m \sum_{i=1}^n |\phi_{i,j}^{\zeta+1}|} \leq 10^{-6}, \quad (13)$$

where both  $m$  and  $n$  are the numbers of grid points in the  $x$ - and  $y$ -directions, respectively,  $\phi$  is any of the computed field variables, and  $\zeta$  is the iteration number.

The performance of the using code via the nanofluid convection problem in a confined enclosure is established by comparing predictions with other numerical results and by verifying the grid independence of the present results. First, the present results are consistent with previous computations, namely those of Oztop and Abu-Nada [17] as shown in Table 2. The present results and those reported by Oztop and Abu-Nada are in excellent agreement since the maximum difference between both results is about 2%. Then, in order to determine an appropriate grid for the numerical simulations, a grid independence study is conducted for the different values of the Richardson number (0.01, 1 and 100) as shown in Table 3. The calculations are performed for the Cu-water nanofluid of  $\phi$  equals 0.02 with six different uniform mesh grids:  $51^2$ ,  $71^2$ ,  $91^2$ ,  $101^2$ ,  $111^2$ , and  $121^2$ . It is observed that a  $91^2$  uniform mesh grid is adequate for a grid independent solution. However, a fine structured mesh of  $101^2$  is used to avoid round-off error for all other calculations in this investigation.

### 4 Results and discussion

First of all, we investigate the convection phenomenon inside the square Cu (or Ag)-water nanofluid cavity, of an inclination angle equals  $0^\circ$ . The Richardson number is ad-

**Table 2:** Average Nusselt number of the heat source compared with Oztop and Abu-Nada [17].

$Ra$	$\phi$	Oztop and Abu-nada [17]	Present study	Relative gap (%)
$10^3$	0.00	1.004	1.005	0.10
	0.05	1.122	1.128	0.53
	0.10	1.251	1.248	0.24
	0.15	1.423	1.419	0.28
	0.20	1.627	1.621	0.37
	0.00	2.010	2.032	1.08
$10^4$	0.05	2.122	2.109	0.61
	0.10	2.203	2.199	0.18
	0.15	2.283	2.291	0.35
	0.20	2.363	2.382	0.80
	0.00	3.983	3.992	0.22
$10^5$	0.05	4.271	4.256	0.35
	0.10	4.440	4.389	1.16
	0.15	4.662	4.680	0.38
	0.20	4.875	4.861	0.29

**Table 3:** Average Nusselt number of the Cu-water nanofluid for different uniform grids.  $\phi = 0.02$ ,  $Pr = 6.2$ .

nodes Number	Nu		
	$Ri = 0.1$	$Ri = 1$	$Ri = 100$
51×51	36.3109	16.0545	5.6052
71×71	43.7220	17.4163	5.8391
91×91	49.9145	17.9306	5.9436
<b>101×101</b>	<b>53.1219</b>	<b>19.9059</b>	<b>6.2693</b>
111×111	53.1216	19.9063	6.2697
121×121	53.1220	19.9062	6.2695

justed between 0.01 and 100 when the nanofluid volume fraction is fixed at 0.02. The streamlines and the isotherm patterns for various values of the Richardson number are presented in Figure 2.

In the case of a dominant forced convection ( $Ri = 0.01$ ), we note a single clockwise rotation cell transported by the translational movement of the active walls. The bottom left and the top right regions seem to be less stirred by the flow; this behavior disappears gradually by increasing the Richardson number.

With mixed convection ( $Ri = 1$ ), we denote a combined effect of the translational motion of the active walls as well as that introduced by the thermal buoyancy forces what causes, then, an extension lengthening of the cell along the diagonal. The latter becomes horizontally extended when a dominated natural convection ( $Ri = 100$ ) is considered, since the active walls effect is weak compared

to the thermal buoyancy forces. In the vicinity of the horizontal and the vertical walls, the flow is generally unidirectional. The Isotherm plots are also presented as a function of the Richardson number, as displayed in Figure 2(b). In the vicinity of the active walls, the thermal boundary layers are found to be less important with the increase of the Richardson number. With the mixed convection case, great temperature gradients are localized in the lower-left and the upper-right parts of the active walls, with a penetration of the hot fluid within the cavity from the upper side, (and vice versa for the cold fluid). At  $Ri = 100$ , the penetration of the heat into the center of the cavity is still observed, whilst the isotherms become fully horizontal.

The effect of the nanoparticles volume fraction on the fluid flow and heat transfer has also been investigated as plotted in Figure 3. Unlike the streamlines, where the same fluid motion is observed, it can be seen from the isotherms that the increase of the latter to 10% leads to the decrease of the thermal boundary layers thickness to be more compact near the active walls. This behavior is reflected in the mean Nusselt number variations according to the Cu and Ag nanoparticles volume fraction, for different values of the Richardson number, shown in Figure 4. For both nanofluids, the last is found to be as a linear increasing function of the nanoparticles volume fraction and decreases with the increase Richardson number. It is worth noting that far from the natural convection mode, natural convection ( $Ri = 100$ ), the heat transfer is more important for the Ag-water nanofluid compared to the Cu-water one, what makes the use of the Ag nanoparticles more required.

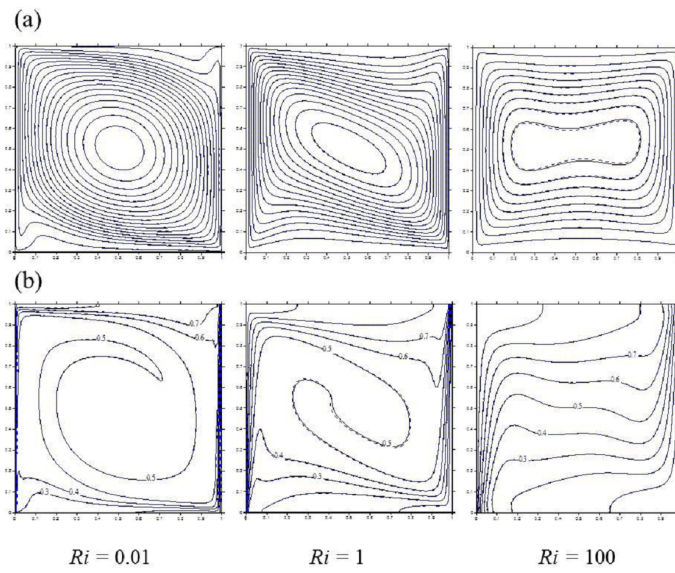


Figure 2: Streamlines (a) and Isotherms (b) for different values of the Richardson number.  $\phi = 0.02$ , [— Cu-water, — Ag-water].

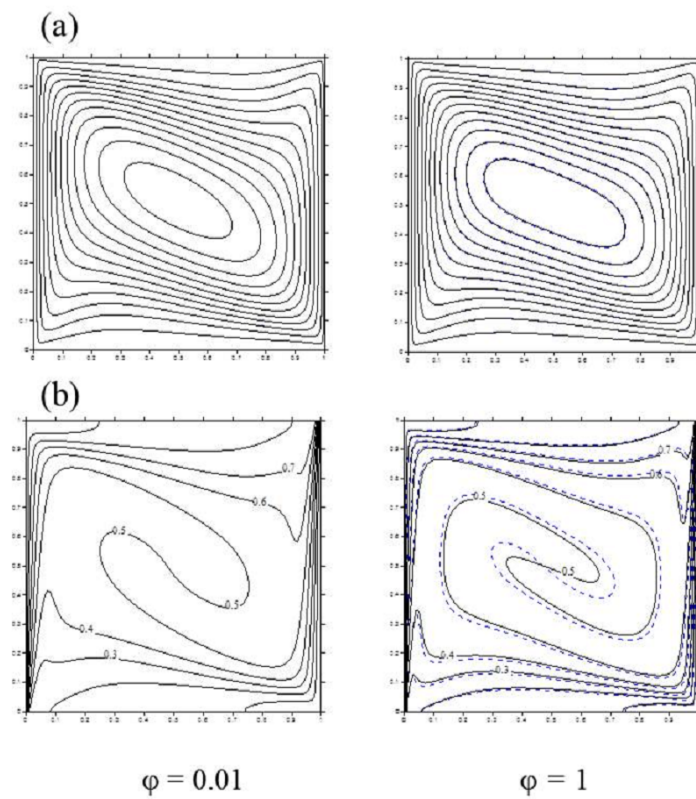
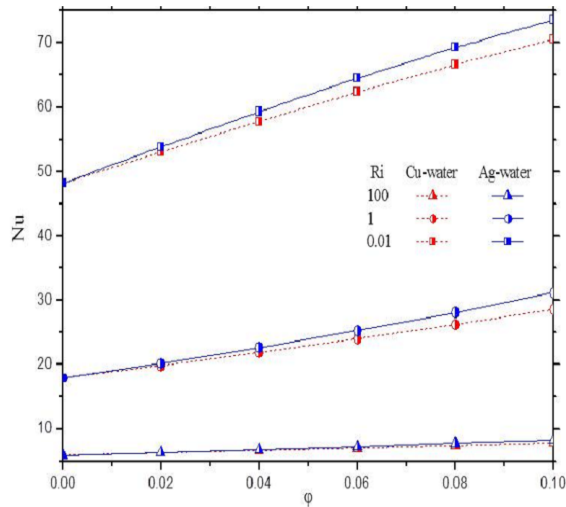


Figure 3: Streamlines (a) and Isotherms (b) of the nanofluids for different values of the solid volume fraction.  $Ri = 1$ , [— Cu-water, — Ag-water].



**Figure 4:** Variation of the mean Nusselt number with the nanoparticles volume fraction for different values of  $Ri$ .

Regarding, the cavity inclination angle effect, Figure 5 displays the mean Nusselt number as a function of the latter (noted as  $\psi$ ) and that, for different values of the Richardson number. As we can see and except for the natural convection mode, the increase of the cavity inclination angle has no significant effect on heat transfer, since the maximum enhancement is found to be quietly over 0.2% than that calculated into a non-inclined one.

However, for  $Ri = 100$ , the increase of the cavity inclination angle over  $90^\circ$  leads to the decrease of the heat transfer rate to reach 69% for an inclination angle of  $180^\circ$ , compared to the case of a non-inclined one. To explain this phenomenon, Figure 6 displays both the streamlines and the isotherm plots for different inclination angles, ranging from  $90^\circ$  to  $180^\circ$ . It can be seen the appearance of a mono-cellular structure when the inclination angle ranges between  $90^\circ$  and  $95^\circ$ . At  $96^\circ$  we denote the destruction of this structure and the appearance of a central cell, with two others near the active walls. By increasing the cavity inclination angle, the central cell becomes more important to the detriment of the wall cells. This can be explained by the fact that the vertical component of the wall velocity increases, and acting strongly in the opposite direction of the buoyancy forces. Consequently, the hot fluid remains confined near the hot wall when the cold fluid near the cold wall. As a result, the extent of the wall cells decreases and so do the mean Nusselt number (Figure 5) when the wall temperature gradient decreases as shown in the Isotherm plots (Figure 6). The minimum heat transfer rate is obtained for  $180^\circ$ , where the active walls' motion is in the

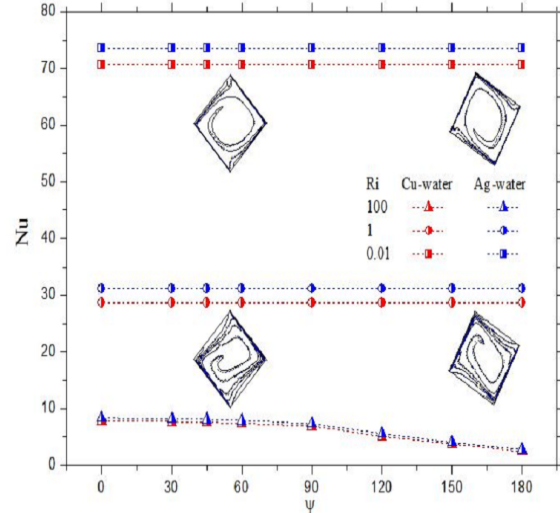


**Figure 5:** Nusselt number as a function of  $\psi$  for different values of  $Ri$ .

opposite direction with the buoyancy forces (upward cold and downward cold walls).

## 5 Conclusion

The analysis of the mixed convection phenomenon in a side moving walls cavity, filled with a nanofluid, was realized through our paper. Taking into account the effects of various parameters, such the Richardson number, the nanoparticles volume fractions, and the inclination angle, the results may resume as follows:

1. Heat transfer is a decreasing function of Richardson number.
2. Heat transfer is improved by the addition of nanoparticles to the base fluid. This enhancement is more pronounced by the increase of the nanoparticles volume fraction.
3. The type of the nanoparticles is a key factor for heat transfer enhancement. Indeed, the highest values of the mean Nusselt number are obtained for Ag nanoparticles.
4. Regarding the forced and mixed convection modes, the inclination angle has no significant effect on the heat transfer.
5. In the case of the natural convection mode, and over  $90^\circ$ , the inclination angle of the enclosure decreases the heat transfer, the reduction is about 69% compared to the case of a non-inclined one.

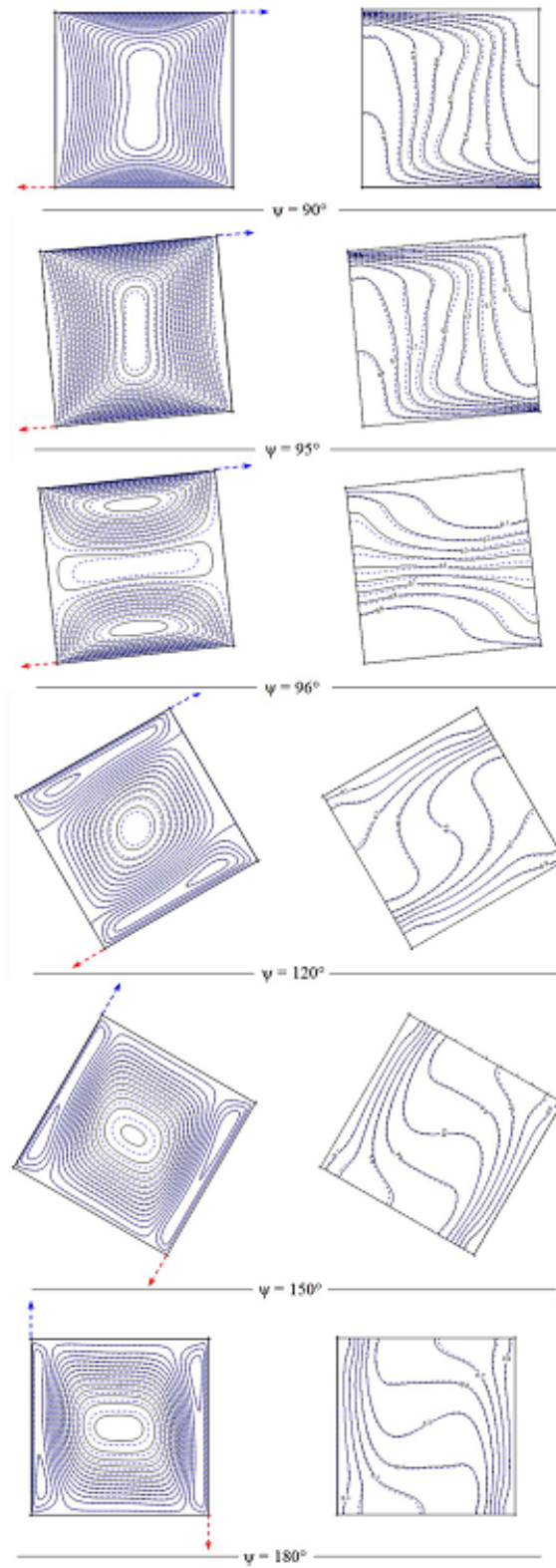


**Figure 6:** Streamlines (a) and Isotherm plots (b) of the nanofluids for different values of the inclination angle.  $\phi = 0.10$ ,  $Ri = 100$ , [— Cu-water, — Ag-water].

## References

- [1] Choi S. U. S., Enhancing thermal conductivity of fluids with nanoparticles. *ASME Fluids Engineering Division*, 1995, 231, 99-105.
- [2] Wang X., Xu X., Choi S. U. S., Thermal conductivity of nanoparticles fluid mixture. *Journal of Thermophysics and Heat Transfer*, 1999, 13(4), 474-480.
- [3] Jou R. Y., Tzeng S. C., Numerical research of nature convective heat transfer enhancement filled with nanofluids in rectangular enclosures. *International Communications in Heat and Mass Transfer*, 2006, 33, 727-736.
- [4] He Y., Men Y., Zhao Y., Lu H., Ding Y., Numerical investigation into the convective heat transfer of TiO<sub>2</sub> nanofluids flowing through a straight tube under the laminar flow conditions. *Applied Thermal Engineering*, 2009, 29, 1965-1972.
- [5] Ashorynejad H. R., Mohamad A. A., Sheikholeslami M., Magnetic field effects on natural convection flow of a nanofluid in a horizontal cylindrical annulus using Lattice Boltzmann method. *International Journal of Thermal Science*, 2013, 64, 240-250.
- [6] Akbarinia A., Behzadmehr A., Numerical study of laminar mixed convection of a nanofluid in horizontal curved tubes. *Applied Thermal Engineering*, 2007, 27, 1327-1337.
- [7] Arani A., Mazrouei S., Mahmoodi M., Numerical study of mixed convection flow in a lid-driven cavity with sinusoidal heating on sidewalls using nanofluid. *Super-lattices and Microstructures*, 2012, 51, 893-911.
- [8] Ghasemi B., Aminossadati S. M., Mixed convection in a lid-driven triangular enclosure filled with nanofluids. *International Communications in Heat and Mass Transfer*, 2010, 37, 1142-1148.
- [9] Santra A. K., Sen S., Chakraborty N., Study of heat transfer augmentation in a differentially heated square cavity using copper-water nanofluid. *International Journal of Thermal Science*, 2008, 47, 1113-1122.
- [10] Elif B. O., Natural convection of water-based nanofluids in an inclined enclosure with a heat source. *International Journal of Thermal Science*, 2009, 48, 2063-2073.
- [11] Ghasemi B., Aminossadati S. M., Natural convection heat transfer in an inclined enclosure filled with a CuO-water nanofluid. *Numerical Heat Transfer Part A*, 2009, 07, 807-823.
- [12] Bejan A., *Convection heat transfer*, John Wiley & Sons, Inc., Hoboken, New Jersey, USA, 2004.
- [13] Khanafer K., Vafai K., Lightstone M., Buoyancy-driven heat transfer enhancement in a two-dimensional enclosure utilizing nanofluids. *International Journal of Heat and Mass Transfer*, 2003, 6, 3639-3653.
- [14] Brinkman H. C., The viscosity of concentrated suspensions and solutions. *Journal of Chemical Physics*, 1952, 20, 571-581
- [15] Maxwell J. C., *A Treatise on Electricity and Magnetism Vol. II*, Oxford University Press Cambridge U.K, 1873.
- [16] Patankar V., *Numerical Heat transfer and fluid flow*, Hemisphere Publishing Corporation, Taylor and Francis Group, New York, 1980.
- [17] Oztop H. F., Abu-Nada, E., Numerical study of natural convection in partially heated rectangular enclosures filled with nanofluids. *International Journal of Heat and Fluid Flow*, 2008, 29, 1326-1336.

## Research Article

## Open Access

Nattan R. Caetano\*, Diego Soares, Roger P. Nunes, Fernando M. Pereira, Paulo Smith Schneider, Horácio A. Vielmo, and Flávio Tadeu van der Laan

## A comparison of experimental results of soot production in laminar premixed flames

**Abstract:** Soot emission has been the focus of numerous studies due to the numerous applications in industry, as well as the harmful effects caused to the environment. Thus, the purpose of this work is to analyze the soot formation in a flat flame burner using premixed compressed natural gas and air, where these quasi-adiabatic flames have one-dimensional characteristics. The measurements were performed applying the light extinction technique. The air/fuel equivalence ratio was varied to assess the soot volume fractions for different flame configurations. Soot production along the flame was also analyzed by measurements at different heights in relation to the burner surface. Results indicate that soot volume fraction increases with the equivalence ratio. The higher regions of the flame were analyzed in order to map the soot distribution on these flames. The results are incorporated into the experimental database for measurement techniques calibration and for computational models validation of soot formation in methane premixed laminar flames, where the equivalence ratio ranging from 1.5 up to 8.

**Keywords:** soot volume fraction; light extinction technique; premixed flat flame

DOI 10.1515/eng-2015-0016

Received September 05, 2014; accepted January 20, 2015

## 1 Introduction

Soot can be defined as the solid particulate matter produced during combustion [1]. The process of formation is

based in the conversion and agglomeration of the carbon atoms contained in the hydrocarbon fuel molecules. The formation of soot is not completely understood due to the complexity and velocity of this transformation. Soot is of great interest in engineering, insofar as its formation increases the radiated heat transfer, which can be a positive to the considered system. The excessive presence of particulate in diesel engines is, an example, where soot is harmful. These particles resulted from an inadequate combustion process can become logged in the seat of valves, preventing a proper seal in the combustion chamber and leading to a loss of compression in the cylinder. Another example is gas turbines, where the presence of soot affects the life of the blades due to abrasion for the contact.

The emission of this type of particulate matter into the atmosphere causes great harm to the environment, since there is a significant deterioration in air quality. Also, induce respiratory problems in humans and is associated with the occurrence of cancer. On the other hand, in industrial heating equipment such as a boiler, the presence of soot increases the heat exchange by radiation from the flame to the system walls, whereas the solid material resulting from the process absorbs and emits radiation at a wide range in the wavelengths spectrum [2]. Thus, where a large and uniform heat transfer is required, the presence of soot in combustion is purposely induced.

To control the emission of soot in real combustion systems, it is necessary to understand the soot formation and oxidation mechanisms. The basis of knowledge is the development of models that can predict the particulate matter formation, and the validation of these models requires information about the soot volume fraction. In this way, optical techniques are generally employed to perform the measurement of these quantities due the non-intrusive probing.

The necessity for such information in the study of combustion was what motivated the present work, which was developed in order to produce significant results for future calibration of measurement techniques and validation of theoretical models in this subject. Hence, the main objective of this study is to analyze the production of soot in premixed laminar flat flames of natural gas and air, measur-

\*Corresponding Author: Nattan R. Caetano: Dept of Mechanical Engineering, Federal University of Rio Grande do Sul (UFRGS), Porto Alegre, RS, Brazil, E-mail: nattan@ufrgs.br

Diego Soares, Roger P. Nunes, Fernando M. Pereira, Paulo Smith Schneider, Horácio A. Vielmo, Flávio Tadeu van der Laan: Dept of Mechanical Engineering, Federal University of Rio Grande do Sul (UFRGS), Porto Alegre, RS, Brazil

 © 2015 N.R. Caetano *et al.*, licensee De Gruyter Open.

This work is licensed under the Creative Commons Attribution-NonCommercial-NoDerivs 3.0 License.

ing the soot volume fraction applying laser light extinction technique in different flame heights for equivalence ratio of 1.5 up to 8, finally, comparing the results with the literature.

## 2 Background

The effects of light scattering by particles have been investigated for more than a century, starting in 1861, even before Maxwell proposed the theory of electromagnetism. Lord Rayleigh applied Maxwell's equations and formally established the theory of Rayleigh scattering in 1881. Other notable scientists who contributed to this line of research include Lorenz in 1890, Mie in 1908, and Debye in 1909. These last two extended the Rayleigh theory to incorporate large and non-spherical particles. Previous studies applied the Rayleigh theory to monitor the mass concentration of the particulate of different sources, such as diesel engines. In the last two decades, several researchers have shown results on the extinction coefficient from studies using hydrocarbon fuels subjected to various combustion conditions. These results are validated based on the use of the light extinction technique and a resume of them was made by Mulholland [3].

The light extinction technique is used in the region of the flame itself, as well as in regions outside of it. For situations that include the flame, the measurement of the soot volume fraction is the main information that helps to understand the development of the particulate material in the combustion. Moreover, the measurement of soot volume fraction by methods such as light extinction is of fundamental importance in the study of radiation transport in combustion.

The determination of soot volume fraction based on the light extinction technique with laser light was performed previously [4]. This method is broadly employed by the scientific community that investigates combustion, since the results obtained are backed up by non-intrusive measurements and generate instant and useful information.

Several optical measurement techniques are calibrated using this method, for instance, the Laser Induced Incandescence method, LII. It has been used to validate the soot volume fraction obtained based on the LII 2D technique in combustion systems with laminar diffusion flames. The LII technique presented dispersion in the range of 5 to 10%, probably due to the difference in particle size [5].

Other researchers contest the findings in the literature for the refractive index of soot particles, which is a key parameter in determining the extinction coefficient [6]. Measurements were performed for the wavelengths of 450, 630 and 1,000 nm using crude oil as fuel. Results have shown that the extinction coefficient for the three wavelengths considered is constant, even though the particle number concentration varied by a factor of 24 due to agglomeration.

Measurements of acetylene premixed flames using both light extinction and gravimetric techniques were performed to obtain the soot volume fraction [4]. After calibration, an extinction coefficient of 8.6 was found and the author states that this number can be applied as the extinction coefficient for soot generated from the combustion of various fuels for lighting systems that include the visible spectrum. The conclusion is that simultaneous measurement methods must be employed for more accurate results of the extinction coefficient.

The light extinction technique was also used by in order to verify the formation of soot into a diesel engine cylinder [7]. The results were compared with other techniques such as the LII and emission in two colors methods to obtain an extinction coefficient with less uncertainty.

Studies on the influence of oxygen and air velocity on soot formation employed the technique of laser light extinction in a diffusive acetylene flame with an annular coaxial injection of oxygen and air [8]. Oxygen enrichment produces an increase in soot formation, as the use of higher injection velocities of air in comparison to fuel. Thus, a control of the amount of oxygen injected and the air velocity can be useful tools for the control of soot production.

Data of the concentration of soot in a non-premixed turbulent ethylene flame were obtained by applying light extinction and scattering technique [9]. The measurements of soot volume fraction in several positions of the flame were performed in the radial and axial direction. A maximum soot volume fraction of 1 ppm was found among all measurements.

The light extinction technique was also employed to obtain quantitative values of the soot volume fraction in sprayed biodiesel flames [10]. LII measurements were made using the light extinction technique results for calibration, which showed a maximum 10% discrepancy between the results.

Furthermore, numerical models can be validated by experimental results measured using the light extinction technique. Authors such as [11, 12] used this technique to validate theoretical models of soot formation using methane and acetylene, respectively.

### 3 Methodology

The transformation of fuel in soot after combustion takes place in five steps, as shown in the Figure 1. The fuel pyrolysis forming the precursors through the processes of cracking, coking and cyclization, in order to form polycyclic aromatic hydrocarbons (PAH), which are composed of ethane ( $C_2H_6$ ). In sequence the Nucleation occurs when a large molecule precipitates, forming a solid particle which shape is considered as a sphere. In the coalescence process, two particles unite to form a larger particle. The surface grows up when the particle absorbs other components, further increasing the size. Finally, the agglomeration is the union of several of these previously formed particles, which results in a solid conglomerate [13].

The laser light extinction technique is based on the Beer-Lambert Law which is an empirical relationship that relates the absorption of light to the medium properties that it passes through. Thus, measurements of light intensity are performed without flame and with laser passing through the flame, which the particles of soot in the laser line of sight attenuate the initial intensity. When applied to the light extinction technique for regions within the flame, becomes [4]:

$$\frac{I}{I_0} = \exp\left(-\frac{x f_v k_e}{\lambda}\right). \quad (1)$$

The approach consists in a burner, the light source, detection and control systems, as shown in the Figure 2. This apparatus was constructed in order to ensure alignment between the components of the illumination and the detection system. The flowfield was characterized by the similar way as done in previous works [14]. As result, a planar and adiabatic flame is obtained.

Two flowmeters were used to control the air and fuel velocities in order to establish the equivalence ratio of the mixture for each flame studied. The gas line from the CNG (Compressed Natural Gas) tank was in 4 bar of pressure and the compressed air line at 3 bar.

The flowmeter used to measure the fuel flow has a scale from 0.2 to 2.0  $Sl \cdot min^{-1}$  and another to air ranging from 0.001 to 0.01  $m^3/s$ , both of Conaut 420, with 5% of uncertainty.

For the detection system a photomultiplier tube was used as photodetector, Hamamatsu, model 931 A. The device has a quantum efficiency of approximately 3.75%, with 2% of uncertainty, for the wavelength of 532 nm emitted from a laser diode, continuous wave, of 1,000 mW power, with an uncertainty of 10 mW.

The photomultiplier tube was connected to a high voltage source, Fluke, model 415B, which provides a voltage

of 1,000 V to amplify the signal intensity. The signal is captured by a digital datalogger multimeter, Agilent, connected to a microcomputer. The HP BenchLink Data Logger program is responsible for the interface, which enables capture of the electrical signal from the photodetector.

A slit was used to prevent the light of the flame to noise in the signal. An optical bandpass filter centered at  $532 \pm 25$  nm was used for further reducing the transmission of ambient and flame light. Thus, only the laser light inside on the photodetector. Finally, a cylindrical lens was positioned after the filter to allow the entire area of the photodetector to be illuminated homogeneously.

The study was conducted in a burner designed in previously studies [15]. The burner base allows the homogeneous mixture of air and fuel, which exits through a disc of 32 mm in diameter with 1,639 holes of 0.5 mm, arranged in a hexagonal pattern. A thermal bath provided water at  $85^\circ C$  to traverses the entire perimeter of the perforated disc in order to avoid the heat exchange between the flame and the burner body, ensuring adiabatic conditions at the base of the flame. This setting allows the development of flat, i.e., one-dimensional planar flames.

The measures were filed in spreadsheet format, which were processed using the program iWork Numbers, from Apple, in order to process the results to yield the  $f_v$  values.

The fuel used in the burner was CNG, which can be easily found at gas stations. According to the supplier, this gas consists of 91%  $CH_4$  (methane), 6.1% of  $C_2H_6$  (ethane), 1.1% of  $C_3H_8$  (propane), 0.4% of  $CO_2$  (carbon dioxide) and 1.4% of  $N_2$  (nitrogen). The calorific value of CNG is around  $38.8 \times 10^6$   $J/m^3$ .

Table 1 presents the flame settings used in the experiment. The flow rates are adjusted to the air pressure and fuel lines, 3 and 4 bar, respectively. For all flame configurations used, the Reynolds number was below 2,100 that is the upper limit for laminar flows.

The light extinction technique is based on measuring the intensity of the laser light that passes through a flame, where part of the light is absorbed, scattered and attenuated due to the presence of particulate material. Therefore, to measure the intensity of transmitted light,  $I$ . The burner was positioned on a support, between the illumination and the detection system, to allow measurements at different heights. The first measurement was performed at 5 mm above the base of the flame. Subsequent measurements were made at intervals of 5 mm. Measurements of  $I_0$  were obtained in the same way as for  $I$ , with the difference that the laser light focused directly on the photomultiplier tube, without crossing the flame.

The field of view was spatially calibrated using images of the burner nose these images were processed with

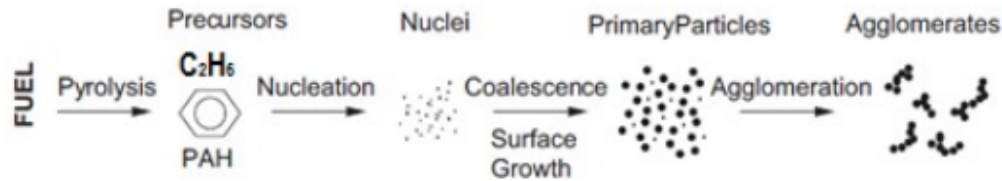


Figure 1: Stages of the soot formation process [13].

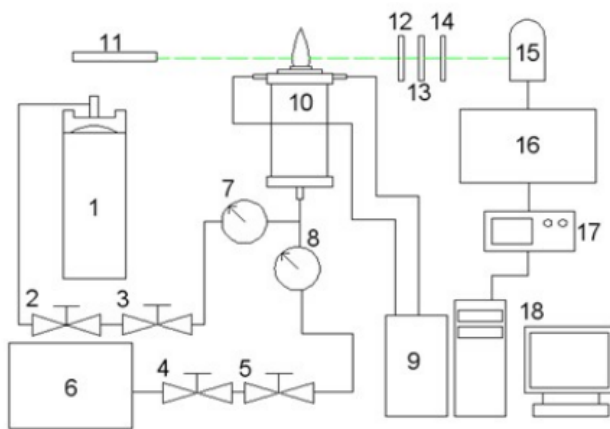


Figure 2: Scheme of the experimental apparatus. 1) Fuel vessel, 2, 3, 4 and 5) Throttle pressure and flow, 6) Air compressor, 7 and 8) Flowmeters, 9) Thermal bath, 10) Burner, 11) Diode laser, 12) Slit, 13) Band-pass optical filter, 14) Cylindrical lenses, 15) Photomultiplier tube, 16) High Voltage Supplier, 17) Datalogger Multimeter, 18) Computer.

Adobe Photoshop CS5 software. The flame thickness, at each height where measurements were made, was measured using the comparison with a known real dimension present in the image. The process consists in comparing the number of pixels that make up the flame with the number of pixels of a pattern with known size at the picture.

Thus, from the data of  $I$  and  $I_0$  obtained experimentally, the knowledge of  $x$  and considering the assumption of  $k_e = 8.6$  [4], values for  $f_v$  could be obtained for the chosen points of the flame and for the different equivalence ratios as detailed in Table 1.

Soot particle size was considered smaller than the laser light wavelength. Thus, the flames configuration is in the Rayleigh regime, where the absorption section is much larger than the scattering one, which allows the applicability of the light extinction technique. Moreover, the light absorption occurs primarily by soot particles, not being verified for combustion products [16].

The values of  $I$  and  $I_0$  are given by the electric signal which is measured by the datalogger, in terms of voltage. These results were submitted to the Chauvenet criterion to

identify values that go beyond the mainstream trend. The criterion specifies that a measured value can be rejected if the probability of obtaining the deviation from the average is less than  $0.5n$ . Where  $n$  is the number of measurements for each measured equivalence ratio.

### 3.1 Measurement uncertainty

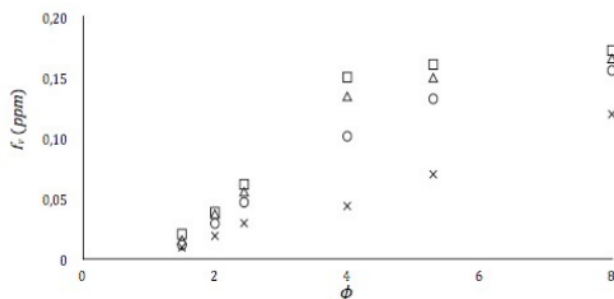
The analysis of experimental uncertainty ( $u$ ) caused by random errors, which lies in result of the addition of small independent and uncontrollable errors, such as errors of measuring instruments, was performed by applying the method of propagation of independent errors proposed by Kline-McClintock.

This method was applied to the results of soot volume concentration. For the error regarding the measurement of the flame width crossed by the laser light was considered as  $u_x = \pm 3 \times 10^{-6}$  m. This value is consistent with the uncertainty in measuring the pixel size during the flame images analysis. The uncertainty of the light extinction factor was considered  $u_{k_e} = \pm 1.5$  [4]. The uncertainty for the average of values obtained in the light intensity acquisition were considered directly of the electrical signal, in Volts, as  $u_{I_0} = u_I = \pm 0.5\%$ . It were made 600 measurements for each  $\phi$  and for each height above the burner considered in this work. In this way, the value was obtained from the ratio between the largest value of the measured RMS signal amplitude, 200 mV, and the average of this signal, 1 mV, where the major ratio value in all measurements was considered. The uncertainty related to the wavelength emitted by the laser was considered  $u_\lambda = \pm 10$  nm, from manufacturer information. Thus, the maximum uncertainty in the measurements of  $f_v$  is about 8% for the results of this work.

A similar analysis was made for the equivalence ratio uncertainties, using the associated of flowmeters uncertainties, that is 5%. Therefore, the uncertainty associated with the air flowmeter to the largest flow used was  $0.2 \text{ Sl.min}^{-1}$  and with the fuel  $0.15 \text{ Sl.min}^{-1}$ . Thus, the measurement uncertainty in the equivalence ratio values of the air/fuel mixtures is approximately 7%.

**Table 1:** Flames configurations.

Flame case	$\dot{V}_{air}$	$\dot{V}_{comb}$	$\dot{V}_{fuel}$	$\phi$	$Re$	$U_{global}(m/s)$
1	0.0083	0.0011	1.5	708	0.49	
2	0.0083	0.0015	2	736	0.51	
3	0.0083	0.0018	2.44	765	0.53	
4	0.0083	0.0026	4	823	0.57	
5	0.0083	0.0035	5.3	890	0.62	
6	0.0083	0.0053	8	1,024	0.71	

**Figure 3:** Relationship between the  $f_v$  formed for each  $\phi$  used. The following symbols represent the measuring height from the base of the flame: (x) of 5 mm, (o) of 10 mm, ( $\Delta$ ) of 15 mm and ( $\square$ ) of 20 mm.

## 4 Results and discussion

The values of  $f_v$  were obtained on different conditions, presented in the Table 1. Measurements were taken at several heights,  $h$ , starting at the flame base. The measurements were not possible at  $h = 0$ , due to the low soot concentration. This corroborates the fact of having a quasi-stoichiometric region.

### 4.1 Behavior of $f_v$ as function of the equivalence ratio and flame height

The behavior of  $f_v$  as function of the equivalence ratio and flame height is shown in the Figure 3. Values of  $\phi$  smaller than 1.5 are considered critical ( $\phi_c$ ) because there is virtually no soot, according to the literature [12, 17]. Therefore,  $f_v$  measurements were performed for  $\phi \geq 1.5$ .

In flames with equivalence ratio of  $2 < \phi < 4$  was observed a sharp increase in the values of  $f_v$ . This increase was greater as higher heights  $h$  were taken for the measurement. This behavior was expected and is consistent with the results presented previously. This occurs due to excessive quantities of fuel in the flame whose conditions are suitable to converting the carbon molecules contained

in the gaseous fuel into soot particles. For values of the equivalence ratio higher than  $\phi = 4$  there is a reduction in the growth rate of  $f_v$ , as observed for height measurement, but not for an oxidation reason. This behavior is attributed to the flame settings, which do not reach enough power, area and temperatures for the production of soot. The rest of the fuel is released in the form of unburned gases in the exhaust.

The statement about the decline in the growth of  $f_v$  for very rich flames was based on the burner characteristics and on the smell from the fuel present during the measurements for these flame configurations and by a toxic gas detector. A gas analyzer or fuel mapping technique would be useful to confirm this statement, but such alternatives were not available in the moment of the measurements.

The  $f_v$  values presented an increasing variation throughout along the flame height, beginning in the base from which the measurements were taken. Stronger growth of  $f_v$  was noticed until  $h \approx 15$  mm, where the amount of soot increases up to 300% for equivalence ratios above 4. Thereafter the increase in the value of  $f_v$  is only 20%. This occurs due to the fact that soot produced at the flame bottom, in most part, becomes oxidized or in other words is consumed at the top of the flame.

The observed behavior can be understood considering that the high exhaust gases temperature from the combustion causes the carbon molecules coagulation. This phenomenon leads to the formation of soot precursors (PAH), which then pass through the nucleation process, thus forming the particulate material. The highest  $f_v$ , 0.172 ppm, is observed for the equivalence ratio  $\phi = 8$ , which was obtained in greater height measurement of 20 mm.

### 4.2 Comparison of the results with literature

The results of  $f_v$  obtained in this work were compared with related studies in the literature, which performed experimental studies and/or numerical modeling. These results

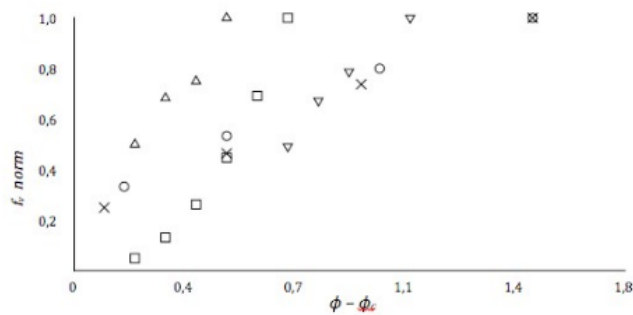


**Figure 4:** Normalized  $f_v$  values in function of the equivalence ratio ( $\phi - \phi_c$ ) for the present study (x), in comparison to the results of [12], ( $\Delta$ ), [17] ( $\square$ ), [19] ( $\nabla$ ) and [18] (o).

were normalized to allow comparison due to the fact that no publications with the same conditions and/or fuel used in this work.

Furthermore, as discussed in the previous section, there is a critical value for the mixture equivalence ratio,  $\phi_c$ . Only for higher equivalence ratios, the formation of soot begins to be observed. This critical value was used to express the equivalence ratio of different works in absolute terms.

Figure 4 presents the comparison of  $f_v$  normalized values (maximum  $f_v$  value divided by the  $f_v$  value for each  $\phi$ ) with respect to the equivalence ratio in absolute values ( $\phi - \phi_c$ ), always used the maximum values of  $f_v$  measured whatever the flame height. A local study was also used as basis of comparison, which developed a model of soot formation in a perfect stirred reactor, using n-heptane as fuel [19].

The behavior is similar for all the results from the literature analyzed, where the soot volume fraction increases as there is an increase in the equivalence ratio.

The increase in  $f_v$  occurred in a more sharply way in the experimental results obtained by Melton *et al.* [17], D'Anna *et al.* [12] and Hadeif *et al.* [18]. The last one used ethylene as fuel and the others two, methane. This behavior is due to the flames configuration. These studies have used other types of burners, which is capable of producing flames of high power from high fuel rates. These characteristics produce flames concentrated in a small volume, reaching high temperatures, which favors the soot formation. On the other hand, the burner available in this study generates low power flames, which are important for model validations. Thus, there are no favorable conditions for the formation of soot that requires temperatures about 1,900 to be produced from methane [1].

The results of  $f_v$  in this work were compared to the theoretical results [19]. A very similar behavior was observed, despite the different conditions in which they were obtained. The correlation coefficient between the results is 99%.

The fitting curve containing the behavior of the results measured in this work may be described by the following equation, with the fit coefficient of  $R^2 = 0.95$ ,

$$f_v = 0.26e^{0.98(\phi - \phi_c)}. \quad (2)$$

This equation can be used to calculate intermediate values or points beyond the measurement range used in order works to serve as base for future studies that aim to simulate the soot production in the same burner configuration used in this experiment.

## 5 Conclusions

The light extinction technique is a feasible way to measure the soot volume fraction produced in premixed flames, specially the flat flames which has a steady distribution of  $f_v$  in the transversal axis. There was no soot formation in the measurements made at the flame bottom, due to the quasi-stoichiometric combustion character in this region.

The values of  $f_v$  increased substantially in measurements made in heights above of 15 mm upstream to the burner surface. This behavior is consistent with the mechanisms of soot formation. For values of  $h$  higher than 15 mm, the growth of  $f_v$  tends to stabilize, due to the oxidation of the particulate matter produced.

The results found on the relationship between  $f_v$  and the equivalence ratio showed that the amount of soot increases exponentially with the equivalent ratio. With respect to mixtures of equivalency ratio greater than 4, excess fuel not burned is released in the exhaust gases, justifying the tendency of stagnation in the production of particulate material in very rich mixtures.

The use of the laser light extinction technique to determine the soot volume fraction led to experimental results similar to the ones obtained by the literature, when compared with each other through normalized values. Comparing to the theoretical model developed in a theoretical, the trend of increase of  $f_v$  with respect to mixture composition used showed consistent results. The correlation between the results of the two studies lies at 99%.

Also, was proposed a representative equation for the soot formation behavior as a function of equivalence ratio, which showed a correlation factor of 0.95. Future studies that require intermediate values in the  $f_v$  range, or even

beyond this range, may use this relation, considering the uncertainty of 5%.

Measurements of  $f_v$  in this work may provide the basis for further studies in combustion, such as the numerical models validation of soot formation in premixed laminar methane flames, with equivalence ratio ranging 1.5 up to 8.

Furthermore, numerical simulations in perfect stirred reactor using natural gas as fuel can benefit from the results of this work to validate models.

## Nomenclature

$I_0$	total intensity of light emitted by a laser, [mW]
$I$	amount of transmitted light, [mW]
$x$	flame thickness that the laser light crosses, [m]
$f_v$	soot volume fraction produced, [ppm]
$k_e$	light extinction coefficient, [-]
$\dot{V}_{air}$	volumetric flow of air, [m <sup>3</sup> /s]
$\dot{V}_{fuel}$	volumetric flow of fuel, [m <sup>3</sup> /s]
$U_{global}$	global velocity of gases, [m/s]
$Re$	Reynolds number, [-]
$h$	Flame height, [m]
$u$	Uncertainty [-]

## Greek letters

$\lambda$	laser wavelength, [nm]
$\phi$	equivalence ratio, [-]
$\phi_c$	critical equivalence ratio, [-]

## References

- [1] Glassman I., Yetter R.A., Combustion, Elsevier, Fourth Edition, 2008, 773.
- [2] Caetano N.R., Pereira F.M., Vielmo H.A., van der Laan F.T., Experimental Study of Soot Volume Fraction Applied in Laminar Diffusion Flames, Mod. Mech. Eng., 2013, 3, 137-141.
- [3] Mulholland G.W., Smoke production and properties, The SFPE Handbook of Fire Protection Engineering, 2002, 258.
- [4] Choi M.Y., Mulholland G.W., Hamins A., Kashiwagi T., Comparison of the Soot Volume Fraction using Gravimetric and Light Extinction Techniques, Combust. Flame, 1995, 102, 161.
- [5] Santoro R.J., Semerjin H.G., Dobbins R.A., Soot particle measurements in diffusion flames, Combust. Flame, 1983, 51, 203.
- [6] Mulholland G.W., Bryner N.P., Comparison of a Fractal Smoke Optics Model with Light Extinction Measurements, Atmos. Environ., 1994, 28, 889.
- [7] Zhao H., Ladommatos N., Optical diagnostics for soot and temperature measurement in diesel engines, Prog. Energ. Combust., 1998, 24(3), 221.
- [8] Santos A.A.B., Influência do Teor de O<sub>2</sub> e da Velocidade do Ar na Formação da Fuligem em Chmas Difusas de Acetileno com Escoamento Anular Paralelo do Oxidante, Master thesis, University of Campinas, 2001.
- [9] Caetano N.R., Pereira F.M., Vielmo H.A., van der Laan F.T., Assessment of Soot Emissions from Commercial Fuels, IJESIT, 2013, 3, 89-92.
- [10] Tran M.K., Dunn-Rankin D., Pham T.K., Characterizing sooting propensity in biofuel–diesel flames, Combust. Flame, 2012, 159, 2181.
- [11] Appel J., Bockhorn H., Wulkow M., A detailed numerical study of the evolution of soot particle size distributions on laminar premixed flames, Chemosphere, 2001, 42, 635.
- [12] D'Anna A., Sirignano M., Commodo M., Pagliara R., Minutolo P., An Experimental and Modelling Study of Particulate Formation in Premixed Flames Burning Methane, Combust. Sci. Technol., 2008, 180, 950.
- [13] Tree D.R., Svensson K.I., Soot processes in compression ignition engines, Prog. Energ. Combust., 2007, 33, 272.
- [14] Caetano N.R., van der Laan F.T., Turbulent Flowfield Analysis in a Bluff-Body Burner Using PIV, WJM, 2013, 03, 215-223.
- [15] Bosschaart K.J., de Goey L.P.H., Detailed analysis of the heat flux method for measuring burning velocities, Combust. Flame, 2003, 132, 170.
- [16] Frencklach M., Clary D.W., Remachandra M.K., Shock Tube Study of the Fuel Structure Effects on the Chemicals Kinectical Mechanisms Responsible for Soot Formation, NASA Contract. Rep. No. 174880, 1995.
- [17] Melton T.R., Vincitore A.M., Senkan S.M., The Effects os Equivalence Ratio on the Formation of Polycyclic Aromatic Hydrocarbons and Soot in Premixed Methane Flames, Twenty-Seventh Symposium (International) on Combustion/The Combustion Institute, Naples, Italy, 1998.
- [18] Hadeif R., Geigle K.P., Meier W., Aigner M., Soot characterization with laser induced incandescence applied to a laminar premixed ethylene-air flame, Int. J. Therm. Sci., 2010, 49, 1457.
- [19] Pinto O., Estudo Teórico da Formação de Fuligem na Combustão do N-heptano, Bachelor monography, Federal University of Rio Grande do Sul, 2012.